Simulations and Electronic Structure of Disordered Silicon and Carbon Materials

A dissertation presented to

the faculty of

the College of Arts and Sciences of Ohio University

In partial fulfillment

of the requirements for the degree

Doctor of Philosophy

Yuting Li

May 2014

This dissertation titled

Simulations and Electronic Structure of Disordered Silicon and Carbon Materials

by

YUTING LI

has been approved for

the Department of Physics and Astronomy

and the College of Arts and Sciences by

David A. Drabold

Distinguished Professor of Physics and Astronomy

Robert Frank

Dean, College of Art and Science

Abstract

LI, YUTING, Ph.D., May 2014, Physics

Simulations and Electronic Structure of Disordered Silicon and Carbon Materials

Director of Dissertation: David A. Drabold

Urbach tails are the exponential band tails observed universally in impure crystals and disordered systems. Evidence has been provided that the topological origin of the Urbach tails in amorphous materials are filaments formed by short or long bonds[20]. One aspect of my work focuses on the size effects and choice of Hamiltonian with respect to the structure of the Urbach tails. The dynamical properties of filaments have been studied by performing Molecular Dynamics simulation under constant temperature. The response of filaments under external pressure has also been explored. The second portion of this dissertation is about carbon in two-dimensional sp^2 phases. Carbon has shown itself to be the most flexible of atoms, crystallizing in divergent phases such as diamond and graphite, and being the constituent of the entire zoo of (locally) graphitic balls, tubes, capsules and possibly negative curvature analogs of fullerenes, the Schwartzites. In this part, we explore topological disorder in three-coordinated networks including odd-membered rings in amorphous graphene, as seen in some experimental studies. We start with the Wooten-Weaire-Winer models due to Kumar and Thorpe, and then carry out *ab-initio* studies of the topological disorder. The structural, electronic and vibrational characteristics are explored. We show that topological disorder qualitatively changes the electronic structure near the Fermi level. The existence of pentagonal rings also leads to substantial puckering in an accurate density functional simulation. The vibrational modes and spectra have proven to be interesting, and we present evidence that one might detect the presence of amorphous graphene from a vibrational signature. We also explore the energy landscape of amorphous graphene and report the eigenstates near the Fermi level.

To my parents, Li Li and Hongyan Dang, and all my family members

Acknowledgements

The past six years at Ohio University have been an extremely precious experience to me. I was extremly lucky that I have met people who are kind, supportive, and understanding to me. There's no way I can achieve the goal of getting my PhD in physics without them. I would like to take this oppotunity to thank all these people thoughout my academic study.

First of all, I want to give my deep gratitude to Dr. David A. Drabold. As an advisor, he is knowledgeable, helpful, and extremly supportive during the whole time. As a mentor, he is a perfect role model for me. He is always enthusiastic for science, kind to others, and extremely considerate. I benefit a lot from him, not only for my academic study, but also for my future career. I feel really grateful and lucky to have had him as my advisor. Without him, I would never make any achievements during these years.

I would like to thank all collaborators in my research. Thanks to their suggestions and contributions, I can succeed in my academic study. I would like to thank Dr. Gang Chen, who gave me valuable suggestions in experimental aspects. I would also like to thank Dr. Mike Thorpe, who provides the amorphous graphene models and valuable discussions about my research work.

I would like to thank all my committee members for their suggestions and help to assemble this dissertation. I would like to thank all my former and current team members, Dr. Mingliang Zhang, Dr. Bin Cai, Dr. Binay Prasai, Kiran Prasai and Anup Pandey for their discussions and help. I want to thank Department of Physics and Astronomy and Ohio University for providing this excellent studying and research environment.

Finally, I want to extend my gratitude to my parents. Their unconditional love and support through all these years give me the strength to pursue my dream. I also want to thank my dear friends here Lulin Jiang, Meng Shi and Bing Xia for their support and encouragement through these years.

Table of Contents

List of Tables

List of Figures

1 Introduction

Amorphous materials, especially amorphous semiconductors, have drawn increasing attention from scientists and engineers. To understand the structural and physical properties of these materials, researchers have to overcome difficulties due to its lack of long-range translational periodicity. It is for this reason that computer simulation has become a key tool to study amorphous materials.

1.1 Computational Methods

To model amorphous systems, the interatomic potential is the basic tool to accurately understand the total energy and interatomic forces. For amorphous materials the chemical bonding between atoms gives rise to the interatomic potential $\Phi(\vec{r})$. Unlike crystalline solids, the details of chemical bonding in amorphous system sensitively depend on the local topology, which creates a big challenge to construct a realistic potential.

When facing the many-body nature of the interactions between electrons, it is nearly impossible to solve the problem directly, thus approximation is required. Nowadays, there are three commonly used paths to the interatomic potential: "empirical" potential (using an ad-hoc functional form), tight-binding approximation and *ab-initio* methods [1]. All these three methods have their own advantages and suitable cases. Both empirical and tight-binding potentials suffer from lack of transferability. By carefully handling this problem, in various cases these two methods are powerful tools which can yield sometimes accurate results in vastly shorter computer time than *ab-initio* methods

1.1.1 Empirical Potentials

Empirical potentials are based on classical chemical concepts. The bonds between atoms may be treated as elastic springs whose distortion determines the potential energy. Typically the interatomic potentials includes some or all of the following terms[2]:

* **Bonded terms**: These terms include bond-stretching, bond-angle-bending, dihedral angles, torsion etc.

* **Non-bonded terms**: These terms include electrostatics and van der Waals interactions.

* **Corrections**: These terms are used to fit the experimental data.

Carefully considering different contributions and fitting the experimental data, known properties, such as bond length, bond angle, melting point, etc., in the reference materials can be reproduced.

1.1.2 Tight-binding Approximation

Another commonly used method is the tight-binding method. In this approximation, the electrons are considered as tightly bound to the nuclei, and have limited interactions with nearby atoms. Then the hamiltonian can be simplified (following [3]):

$$H = H_{at} + \Delta U(\vec{r}) \tag{1.1}$$

Here H_{at} is the hamiltonian for one single atom in the lattice located at origin, $\Delta U(\vec{r})$ is the potential generated by all the other atoms in the crystal. Assume $\psi_n(\vec{r})$ is the eigenfunction of H_{at}, and $\psi(\vec{r})$ is the eigenfunction of H. First the wave function localized around one atom can be expanded as a linear combination of $\psi_n(\vec{r})$:

$$\phi(\vec{r}) = \sum_n b_n \psi_n(\vec{r}) \tag{1.2}$$

Then the single particle hamiltonian can be simplified to:

$$H = \sum_{\vec{R}} U_{\vec{R}} |\vec{R}\rangle\langle\vec{R}| + \sum_{\vec{R}\vec{R}'} t_{\vec{R}\vec{R}'} |\vec{R}\rangle\langle\vec{R}'| + t_{\vec{R}'\vec{R}} |\vec{R}'\rangle\langle\vec{R}| \tag{1.3}$$

Here $\vec{R}'$ represents the set of nearest neighbors of $\vec{R}$. The first term in Eq. 1.3 describes the potential of electron at a lattice site, the second term is a hopping term producing

interaction energy between nearest neighbors. For disordered systems, the off-diagonal hopping matrix elements depend on $\vec{R}$, which means their values vary from site to site. The free parameters in tight-binding hamiltonian are obtained by fitting to density functional or experimental results.

1.1.3 *ab-initio* Methods

The third well developed set of methods is characterized as "*ab-initio*". One approach is density functional theory (DFT), which is based upon the ground state charge density as the fundamental variable instead of the many-particle wave functions[34]. The well-accepted theory is introduced by Kohn and Sham (1965). This approximation introduces a set of N single-electron orbitals $|\psi_l(\vec{r})\rangle$, then the Schrödinger equation can be written as:

$$-\frac{\hbar^2}{2m}\nabla^2\psi_l(\vec{r}) + \left[U(\vec{r}) + \int d\vec{r}\frac{e^2\rho(\vec{r}')}{|\vec{r}-\vec{r}'|} + \frac{\partial\mathcal{E}_{xc}[\rho]}{\partial n}\right]\psi_l(\vec{r}) = \mathcal{E}_l\psi_l(\vec{r}) \tag{1.4}$$

In Eq. (1.4) the exchange-correlation $\mathcal{E}_{xc}[\rho]$ is still unknown. Two common approximations have met with widespread use.

The simplest approximation for the exchange-correlation term is the Local Density Approximation (LDA). This key approximation can be expressed as:

$$\mathcal{E}_{xc}[\rho] = \int \epsilon_{xc}[\rho(\vec{r})]\rho d\vec{r} \tag{1.5}$$

Here $\epsilon_{xc}[\rho(\vec{r})]$ is the exchange-correlation energy per particle of the homogeneous electron gas. The exchange energy is given by a simple analytic form $\epsilon_x[\rho] = -\frac{3}{4}(\frac{3\rho}{\pi})^{\frac{1}{3}}$[34] and the correlation energy has been calculated to great accuracy for the homogeneous electron gas with Monte Carlo methods[4].

Another valuable approximation that is sometime helpful is the Generalized Gradient Approximation (GGA), for which[34]:

$$\mathcal{E}_{xc}[\rho] = \int \epsilon_{xc}[\rho(\vec{r}), |\nabla\rho(\vec{r})|]\rho d\vec{r} = \int \epsilon_{xc}[\rho(\vec{r})]F_{xc}[\rho(\vec{r}), |\nabla\rho(\vec{r})|]\rho d\vec{r} \tag{1.6}$$

Here $\epsilon_{xc}[\rho(\vec{r})]$ is the exchange-correlation functional of the homogeneous electron gas, and F_{xc} is dimensionless, and based upon three widely used forms of Becke (B88)[5], Perdew and Wang (PW91)[6], and Perdew, Burke and Enzerhof (PBE)[7]. This approximation is expected to improve results for less homogeneous systems.

Both empirical potential and tight-binding approximations are computationally cheap relative to *ab-initio*, but suffer from a lack of transferability and reliability in arbitrary bonding environments. *Ab-initio* methods are applicable to many systems, but at a significant computational price. Nowadays, SIESTA[8] and Vienna *ab-initio* simulation package (VASP)[9] are two widely used *ab-initio* programs to calculate band structure, electronic density of states, total energies, forces and other quantities. SIESTA uses pseudopotentials and both LDA and GGA functionals. While VASP is based on pseudopotentials, it employs a plane-wave basis and offers various density functionals.

1.2 Structure Analysis

Unlike crystalline materials, amorphous materials lack long-range order. Scientists have developed a wide range of theoretical and experimental methods to study the structure of amorphous materials. X-ray and neutron diffraction are two widely used methods; whereas in simulations *ab-initio* is the method of choice. Some statistical functions are used to study the atomic structures, for both experimentally and computer models.

1.2.1 Radial Distribution Function

One of the most commonly used functions is the radial distribution function (RDF) $g(r)$, also known as the pair distribution function, which describes the probability of finding an atom as a function of distance from one particular particle. The general form of

radial distribution function is[10]:

$$g(\vec{r}) = \frac{1}{\rho^2 V} N(N-1)\langle \delta(\vec{r} - \vec{r}_{ij})\rangle \tag{1.7}$$

Where ρ is the number density, V is the volume of the model, and r_{ij} is the distance from any atom to the central atom. The last term means average over all configurations, which can be expressed as:

$$\langle \delta(\vec{r} - \vec{r}_{ij})\rangle = \frac{1}{N(N-1)} \sum_{i,i\neq j} \delta(\vec{r} - \vec{r}_{ij}) \tag{1.8}$$

Plug Eq. (1.8 into Eq. (1.7), the $g(\vec{r})$ can be written as:

$$\begin{aligned} g(\vec{r}) &= \frac{1}{\rho^2 V} N(N-1) \frac{1}{N(N-1)} \sum_{i,i\neq j} \delta(\vec{r} - \vec{r}_{ij}) \\ &= \frac{1}{\rho^2 V} \sum_{i,i\neq j} \delta(\vec{r} - \vec{r}_{ij}) \end{aligned} \tag{1.9}$$

Then to find the radial distribution function $g(r)$, we need to average $g(\vec{r})$ over all the space:

$$\begin{aligned} g(r) &= \int \frac{d\Omega}{4\pi} g(\vec{r}) \\ &= \frac{1}{\rho^2 V} \sum_{i,i\neq j} \int\int \frac{sin\theta}{4\pi} d\theta d\phi \frac{1}{r^2 sin\theta} \delta(r - r_{ij})\delta(\theta - \theta_{ij})\delta(\phi - \phi_{ij}) \\ &= \frac{1}{\rho^2 V r^2} \sum_{i,i\neq j} \delta(r - r_{ij}) \end{aligned} \tag{1.10}$$

The radial distribution functions provide important information about local structure in amorphous materials. The nth peak in the function indicates the average distance between any atom and its nth neighbor. Since amorphous materials do not have long-range order, the $g(r)$ eventually goes to one at large r.

1.2.2 Ring Statistics

Ring statistics is another commonly used measure in my work. In a network, a path means a series of nodes and links connect sequentially without overlap. Then the simplest

definition for a ring is a closed path. In real calculations of ring statistics, the definition of ring and the properties of the model have also to be taken into consideration. There are four commonly used definitions of rings:

* **King's shortest path criterion** This is the first definition of rings given by Shirly V. King [11], where a ring is defined as the shortest path between two of the nearest neighbors at a given node (atom).

* **Guttman's shortest path criterion** Latter Guttman gave another definition which defines a ring as the shortest path from one node (atom) to one of its nearest neighbors[12].

* **Primitive rings** A primitive (also known as irreducible) ring means it can not be decomposed into two smaller rings[13] [14] [15].

* **Strong rings** This definition is obtained by extending the definition of primitive rings [13] [14]. A strong ring means it can not be decomposed into any number of smaller rings.

From the ring statistics calculation, we can get an impression about the connectivity of the system, which is important to understand the local structure of amorphous materials. In my study, most of the ring statistics calculations are done by a convenient public domain program called ISAACS [16].

1.2.3 Electronic Structure Analysis

Applications of amorphous materials often depend upon their electronic properties. The electronic structure is usually analyzed by the electronic density of states (EDOS) and projected density of states (PDOS)[3].

The EDOS can be written as:

$$g(E) = \frac{1}{N}\sum_{i=1}^{N_{basis}} \delta(E - E_i) \tag{1.11}$$

Here E_i is the eigenvalue of the system and N_{basis} is the number of basis orbitals. An important message we can get from EDOS is the band gap and states near it, from which we can get a general picture about the electronic properties of given material. The other important information is the shape of the band tails near the Fermi level. For crystalline materials, due to the Van Hove singularities, we expect sharp edges at the band tail. But for amorphous materials, without the long-range order, they'll have smooth edges, which will be explained in a later chapter.

The second important tool for analysis is the projected DOS (PDOS), which can be written as:

$$g_n(E) = \sum_{i=1}^{N_{state}} \delta(E - E_i)|\langle\phi_n|\Psi_i\rangle|^2 \tag{1.12}$$

where $g_n(E)$ is the projected density of states on n^{th} site, ϕ_n is the orbital localized on given site and Ψ_i is the i^{th} eigenvector whose eigenvalue is E_i. From this function, we can find the relation between spatially local structure and the electronic structure.

Another frequently used quantity is inverse participation ratio (IPR), which provides a useful tool to associate topological irregularities with localization of eigenstates in amorphous materials and glasses. The IPR of j^{th} eigenstate is defined as[17]:

$$I(\psi_j) = N\frac{\sum_{i=1}^{N} a_i^{j4}}{(\sum_{i=1}^{N} a_i^{j2})^2} \tag{1.13}$$

Where N is the number of atoms in given model, and $\psi_j = \sum_{i=1}^{N} a_i^j \phi_i$ is the j^{th} eigenvector. In principle, for extended state, which is uniformly distributed over atoms, $I(\psi_j) = 1/N$. For highly localized state, $I(\psi_j) \to 1$. I have assumed that the basis is orthonormal in Eq. 1.13.

Moreover, for certain highly localized eigenstates, PDOS calculation for this eigenstate will provide valuable information about its structural signature. Thus

combining the calculation results of IPR and PDOS, the key structure features that greatly influence the electronic properties could be found.

1.3 Organization of Dissertation

The rest part of this dissertation is organized as: In Chapter 2, properties of Urbach tails in amorphous silicon will be discussed. The thermal and vibrational properties of Urbach tails in amorphous silicon models will be emphasized. In Chapter 3, the electronic and vibrational properties of various sp^2 phases of carbon will be discussed, involving crystalline graphene, carbon nanotubes, fullerenes, and schwarzites. The studies of potential energy landscape of amorphous graphene will be presented, and the electronic structure of both planar and puckered amorphous graphene will be discussed in Chapter 4. In each chapter, the computation and analysis methods will be explained in detail.

2 URBACH TAILS

Part of the following work in Chapter 2 is published in D. A. Drabold, Y. Li, B. Cai, and M. Zhang, Physical Review B **83**, 045201 (2011).

2.1 Introduction

The so-called "Urbach tails" were first observed by Franz Urbach in a set of measurements in the absorption spectrum of silver bromide crystals in 1953 [18]. In these experiments, he observed the absorption edges were close to straight lines in plot of the logarithm of absorption coefficient versus frequency. Later on, scientists found exponential absorption edges are not unique, but a common phenomena in amorphous materials, liquids, other disordered materials and even defective crystals. One of the most important topics of amorphous semiconductors (because of the universality of the effect) is to find the link between structural features and electronic or optical properties of the materials. Anderson, Mott and others gave the first clue in the late 1950's, their work indicates that electrons are localized by disorder [19]. In subsequent decades, a lot of theoretical models have been proposed to explain how disordered structure would give rise to these exponential tails, but most of them suffers of lack of applicability to all systems or incompleteness in theory.

In a previous study of amorphous material models in our group, it has been shown that in our best available models the Urbach tails are associated with topological filaments containing short or long bonds [20] [21], and the short (long) bonds are spatially correlated forming subnetworks in the system. The short bonds tend to form a 3-D cluster, whereas the long bonds form 1-D filament. And there is little long to short bond correlation. Also it was found that the valance (conduction) tail states are localized at short bond cluster (long bond filament).

In the following sections, I demonstrate the existence of Urbach tails in three large scale models using a tight-binding calculation. I study the character of the strain field centered on particularly short bonds, the effect of thermal disorder on the band tails, and filaments, and finally the phonon trapping effect of the cluster formed by short bonds.

2.2 Calculations on a Large Systsem

To investigate the role of finite size effects, models with up to 10000 atoms have been carefully studied. We extend this to 100000 atom models and show that a well-made model of this size produces highly exponential tails.

By carefully exploiting locality of interactions and implementing various clever computational tricks, Mousseau and Barkema[22] have proposed genuinely enormous, but nevertheless high-quality, models of α-Si, the largest to date being 100000 atoms. These models are cubic and periodic boundary conditions are applied. To determine whether the Urbach edges are a property of a large system, we compute the density of states for this model. We show that both tails are quite exponential and indeed very close to an earlier calculation[23] on a smaller (4096-atom) model proposed by Djordjevic and coworkers[24].

In recent years there have been significant advances in obtaining the electronic structure of large systems. While the roots of these approaches extend back at least to Haydock and Heine's recursion method[25], conceptual advances in the nineties showed how to compute total energies and forces in a fashion that scales linearly with system size - the so-called order-N methods[26]. For the present topic, we are concerned primarily with the spectral density of states for a singleparticle Hamiltonian in a local basis (orthogonal tight-binding) representation.

Within a tight-binding approach, the electronicHamiltonian matrix H of a large model of α-Si is readily computed because it is extremely sparse (meaning that the

overwhelming majority of the matrix elements vanish). Using the Hamiltonian of Kwon *et al.*[27] (with four orbitals per site and a cutoff between the second and third neighbors for Si) we find that about 54 million matrix elements are nonzero, out of 400000^2 matrix elements in total, so that only about 1 in 2800 entries in the matrix is nonvanishing. As such, one can take advantage of sparse matrix methods formulated to carry out all matrix operations using only the nonzero matrix elements.

The principle of maximum entropy (maxent) provides a successful recipe for solving missing information problems associated with spectral densities, such as the electronic (or vibrational) density of states[28]. Let ρ be the maximum entropy estimate for this density. The maxent framework prescribes that we maximize the entropy functional:

$$S[\rho] = -\int d\epsilon \rho(\epsilon) log[\rho(\epsilon)] \tag{2.1}$$

subject to the condition that $\rho(\epsilon)$ satisfies all known information about ρ, and with implied integration limits over the support of ρ.As discussed elsewhere[29], it is easy to get accurate estimates of the power moments $\mu_i = \int_a^b d\epsilon \epsilon^i \rho(\epsilon)$, $i = 1, N$. By using simple tricks, one can generate hundreds of power moments in seconds for systems with 10^5 or more atoms (this is because the only operations involving H are of the form matrix applied to vector). Then maximizing Eq. 2.1 (solving the Euler equation) subject to the moment data leads to

$$\rho(\epsilon) = exp\left[\sum_{i=0}^{N} \Lambda_i \epsilon^i\right] \tag{2.2}$$

From a computational point of view, the maxent moment problem is solved by finding the Lagrange multipliers $\{\Lambda\}$ that satisfy the moment conditions. This system of equations presents a dreary nonlinear problem, but by using orthogonal polynomials rather than raw powers and converting the calculation into a convex optimization problem, practical solutions are available for more than 100 moments[29][30][31].

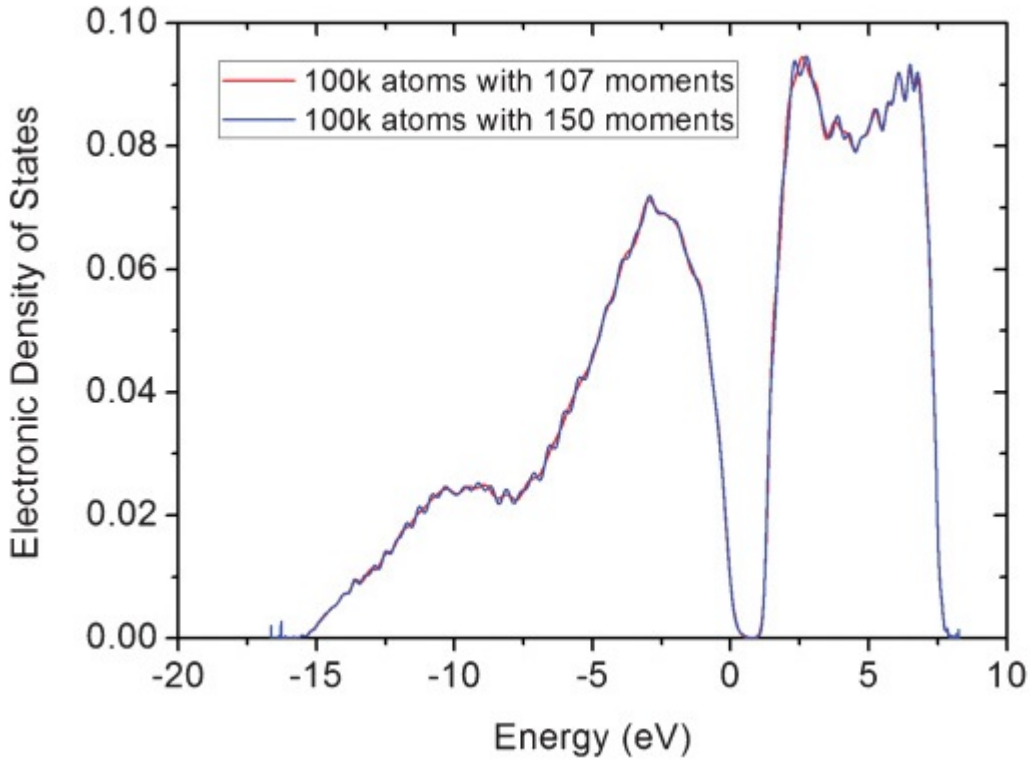

Figure 2.1: Electronic density of states for 100 000- atom α-Si model from maxent reconstruction based on 107 and 150 moments. As the curves are nearly identical, ca. 100 moments appears to be sufficient to accurately reproduce the state density. The Fermi level is in the middle of the gap.

In Fig. 2.1 we reproduce the electronic density of states for the 10^5-atom model. We carry out the maxent reconstruction for 107 and 150 moments; the results are nearly identical, implying that the density of states is converged with respect to moment information for of order 100 moments. We show the global density of states, including a state-free optical gap. In Fig. 2.2, we show a blowup of the gap region.By fitting the tails to an exponential $exp(-|E - E_t|/E_U)$, where E_t indicates the valence or conduction edge, we obtain Urbach energies of $E_U = 200$ meV for the valence tail and $E_U = 96$ meV for the conduction edge. Semilog plots of the density of states for tail energies (not reproduced here) exhibit the expected linear behavior. These Urbach decay parameters are very close

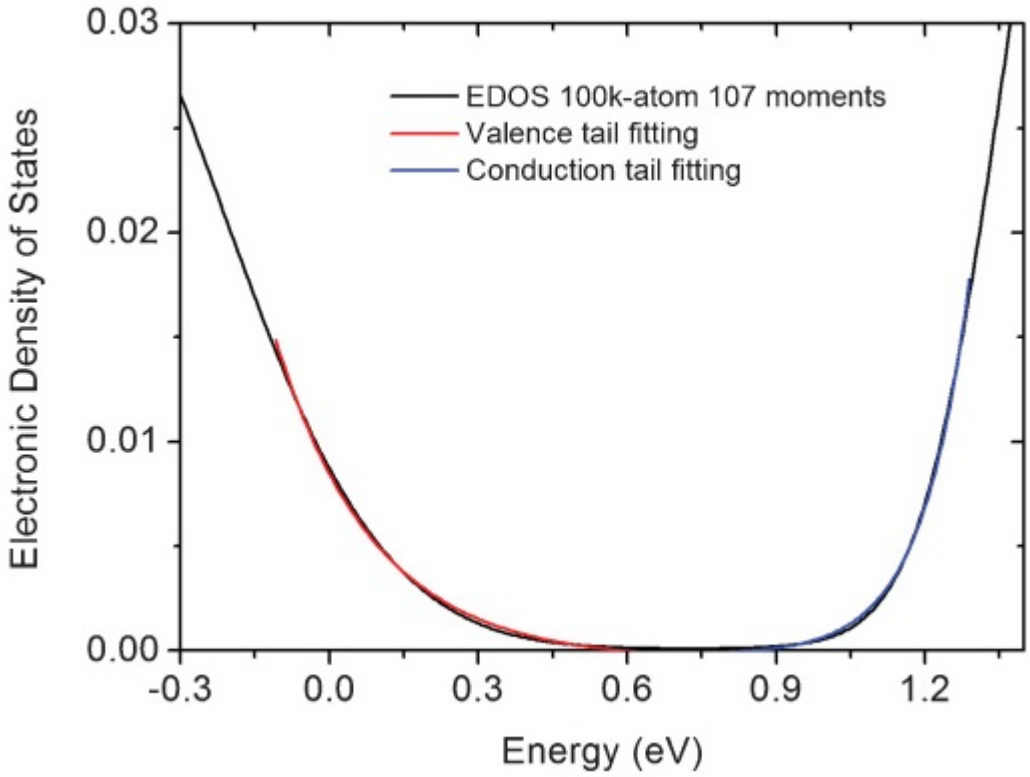

Figure 2.2: Least-squares fits to exponentials for valence and conduction tails for maxent reconstruction of the density of electron states for 100000-atom model, based on 107 moments.

to earlier calculations on somewhat smaller systems[23][32]. The small spikes near -16.0 eV are ”real”: the moment data and maxent technique produce respectable δ functions for isolated states with extremal energies.

We have also determined that the exponential edges are not limited to the valence and conduction tails. The ”extremal tails” (near -15 and +8 eV) are also highly exponential. The high-energy edge has an Urbach parameter $E_U = 130$ meV. The low-energy tail is much sharper than the other three, but still plausibly exponential when plotted on a log scale. It is not possible to access these extremal tails optically or electronically, being so

far removed from the Fermi level, yet they do contribute to quantities like the total energy and forces.

We make two additional points. First, the exponential form is in no way due to the maxent approach, which is nonbiased. While the identical calculation has not been published on diamond Si, there are published calculations on very large fullerenes (with up to 3840 atoms, asymptotically approaching graphene) that show a sharp band edge as in crystals, *not* an exponential, an edge that is essentially identical to an exact calculation of the graphene electronic density of states obtained from Brillouin-zone integration[33][34]. From a mathematical point of view, it is no mean feat for the maxent form [Eq. 2.2] to produce simple exponential tails in the gap. In effect, the network structure of connected filaments (and the consequent electronic Hamiltonian matrix) causes $\sum_{i=0}^{N} \Lambda_i \epsilon^i \approx \lambda\epsilon$ for $\epsilon \in \mathcal{E}$, where $\mathcal{E}$ defines a spectral energy range including the two band tails and λ is characteristic of the decay of the valence or conduction tail. Other illustrations can be found in the theory of magnetic resonance[35][36]. Finally, calculations with more sophisticated (density functional) Hamiltonians (and necessarily smaller models that require Brillouin zone integrations) show exponential tails for topologically similar models[20][37].

2.3 Strain Recovery for Short Bonds

We have shown in earlier work that if a particularly short bond appears in the network, it will tend to be connected to other short bonds, which tend to be connected to additional short bonds, etc. Let us name the central short bond a ”defect nucleus”. As one progresses away from the nucleus, the bond lengths must asymptotically return to the mean bond length of the network. In effect, there is a strain field induced by the anomalous short bond. In Fig. 2.3, we illustrate this strain field. There is a reasonably consistent form to the curves, which are plotted for the shortest few bonds in the 512-atom

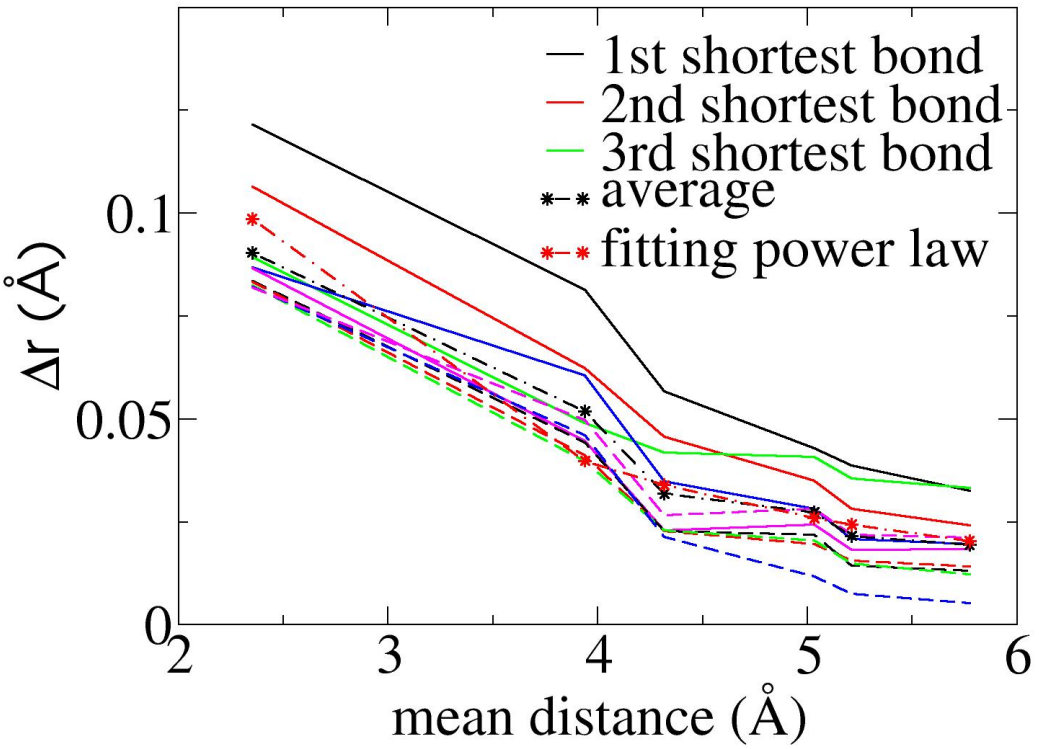

Figure 2.3: Strain recovery in a 512-atom model of α-Si: shortest few bonds. Δr is the difference in bond length from the mean; r is the distance from the short bond defect nucleus.

model. By fitting a power law $\delta r = Ar^{\gamma}$ (or alternatively, examining a log-log plot), we find that $\gamma = -1.86 \pm 0.52$. For several reasons (poor statistics, only a small range of r contributing meaningful information, etc.) this number is not to be taken too seriously. In fact, we are inclined to wonder if a more refined attempt will not yield a $1/r$ law, as predicted for a point deformation for a continuum model by Lord Kelvin[38].

Despite these uncertainties, the consistency of this decay between the different short bond centers is interesting. It seems that to a significant degree, anomalous bonds determine their local topology. Bond length defects have a characteristic spatial range

associated with them, and the range is quite predictable for short bond defects, at least. The main point is that one must be careful about thinking in overly local termsone anomaly affects many atoms. For the case of short bonds, this discussion is salient to the valence tail. In α-Si, the valence tail is known to be broad and mainly due to static (not thermal) disorder[39]. In other terms, an individual point defect can introduce density fluctuations on a scale of order $5 - 7$Å[1]. Since short bonds beget short bonds (always with electronic signature at the valence edge), there is a cumulative electronic consequence at the valence edge. Presumably it is this nonlocality and the tendency of the network to local density that makes the valence tail broad (as in an experiment in α-Si : H in Ref. [40]). For hydrogenated material, the broad valence tail impedes hole mobility. Thus, our calculations suggest that a maximally homogeneous material is ideal for applications. How homogeneous this can be, either in the experimental material or in models is not clear, though we know that the WWW class models are exceptionally uniform compared to models made in other ways[41].

Where long bonds are concerned, the pattern is less clear because there is a basic asymmetrysufficiently long bonds are not bonds! Clearly there is no pattern so clear as Fig. 2.3 for long bonds (since it is silly to imagine that very long, e.g., nonexistent, bonds could induce slightly shorter long bonds, etc.) The experimental observation that the valence tail is much broader than the conduction tail is presumably connected to this basic asymmetry. Bond length distribution is almost symmetric about long and short in a good model. Because thewave functions of the conduction states are mainly distributed in the dilute regions, the disorder potential they feel is weak; thus the conduction tail is less broadened.

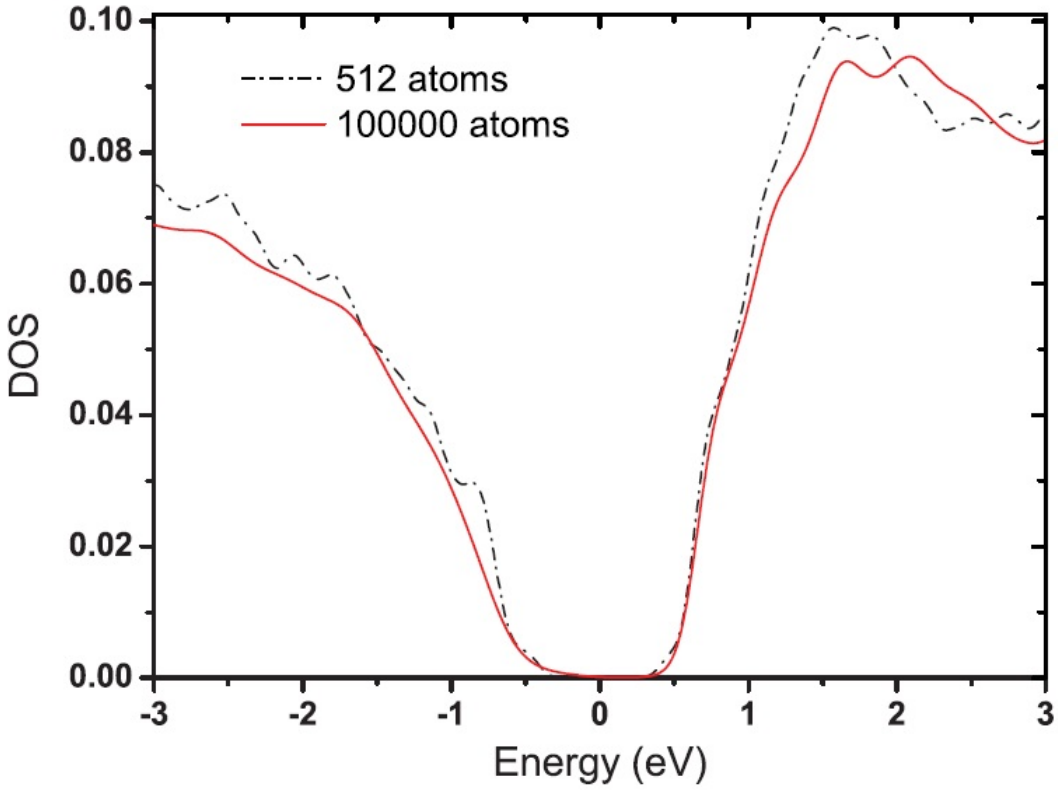

Figure 2.4: Comparison of electronic density of states between the 512-atom model and the 100 000-atom model.

2.4 Size Effects and Hamiltonians

Because we cannot perform molecular dynamics (MD) simulations on the 100000-atom model or even the 4096-atom model, we are led to investigate the effects of thermal motion on the filaments and associated electronic structures at the tails. First, we consider the possible importance of size artifacts on the energy spectrum by comparing the 100000-atom model with a 512-atom model made in a similar way[24], and we show the result around the gap in Fig. 2.4. Both plots have similar general features, though the electronic density of states (EDOS) of the 100000-atom model is of course smoother than that of the 512-atom model. Within finite size artifacts, the 512-atom model is producing a

fairly exponential tail which indicates that the 512-atom model is an appropriate basis to study some aspects of the tails in α-Si.

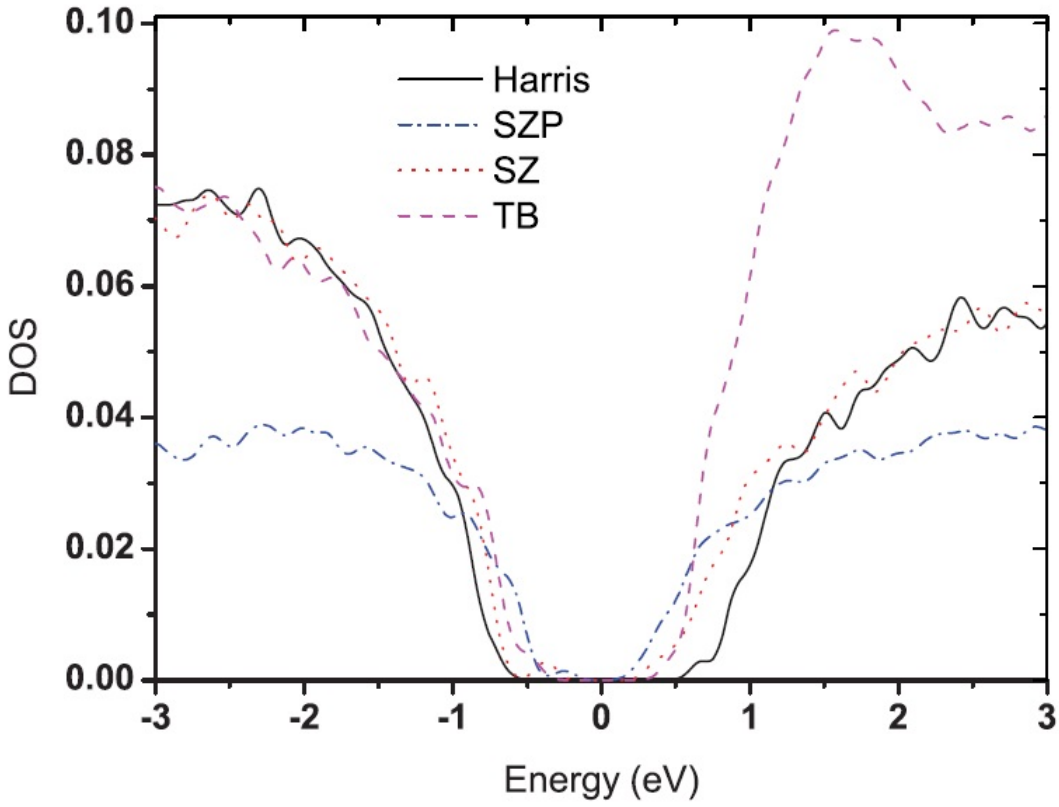

Figure 2.5: Electronic density of states of 512-atom models obtained by SIESTA self-consistent calculation with single-ζ and single-ζ-polarized basis sets, by the tight-binding method, and by a Harris functional calculation with a single-ζ basis.

Next, we compare the EDOS of an α-Si 512-atom model obtained via different Hamiltonians and plot the results in Fig. 2.5. The EDOS of a 512-atom model are computed by SIESTA self-consistent calculation with single-ζ and single-ζ-polarized basis sets, by the tight-binding method, and by SIESTA using a Harris functional calculation with a single-ζ basis. We point out that the Harris functional calculation gives a significantly bigger highest occupied molecular orbital (HOMO)-lowest unoccupied

molecular orbital (LUMO) gap and, as expected, the more complete the basis the smaller the gap. Though the shapes of EDOS are different for different basis sets, we observe that different basis sets all produce qualitatively exponential tails at least within the finite size effects for the small 512-atom model.

2.5 Filament Dynamics

Total yield photoelectron spectroscopy measurements have shown interesting behavior in the band tails of α-Si : H and related materials[42][39]. In the experiments of Aljishi *et al.*[39] it was found that the valence tail was due primarily to structural disorder and that the conduction tail was much more temperature dependent, and thus linked to thermal disorder. MD simulations have been applied to model these effects[43].

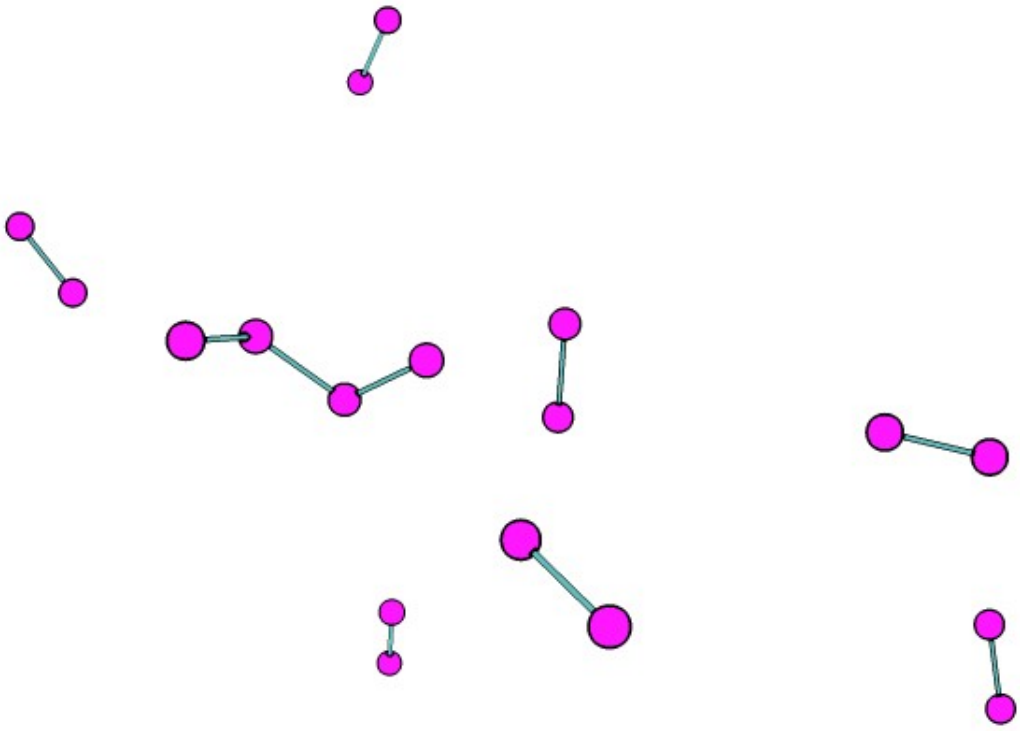

Figure 2.6: Instantaneous snapshot of short bonds in the 512-atom model at 300 K. Only bonds less than 2.3Å are shown. A bar connecting the spheres indicates a chemical bond.

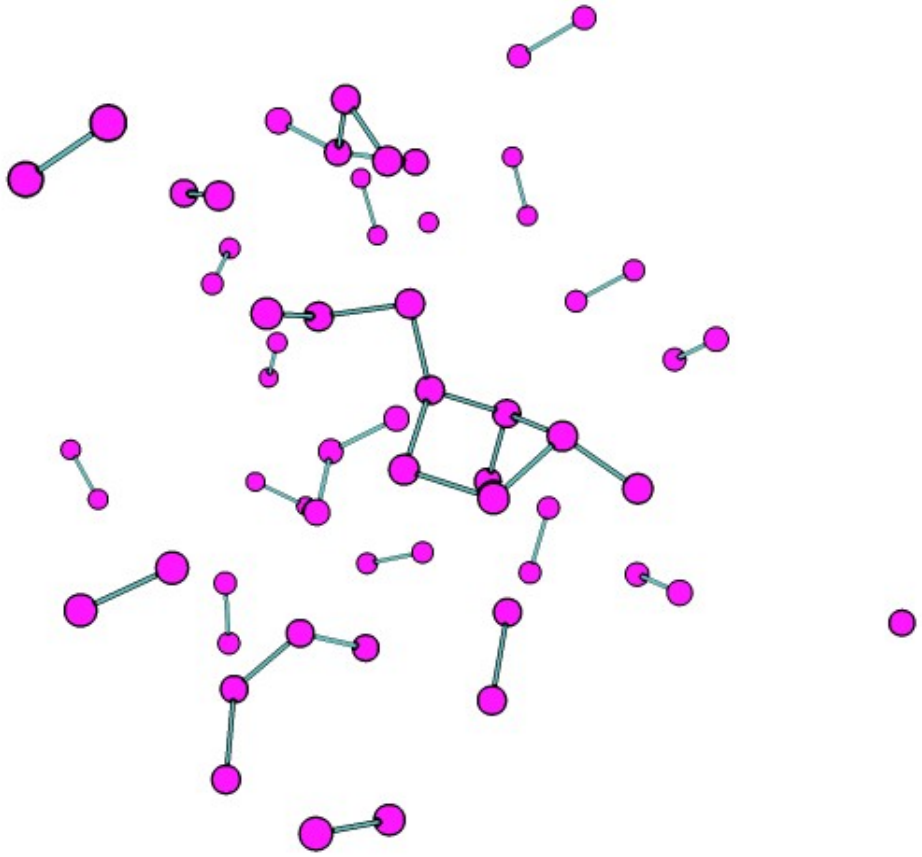

Figure 2.7: Another instantaneous snapshot of short bonds in a 512-atom model at 300 K. Bonds less than 2.3Å are shown.

As another step toward understanding the effect of a dynamic lattice on the band tails, we have created animations of the dynamics of the short bonds in the 512-atom cell[24] using the local orbital *ab initio* code SIESTA[8] for temperatures from 20 to 700 K (in each case using constant temperature dynamics). In Fig. 2.6 and 2.7 we show instantaneous snapshots of the shortest bonds at two different times at 300 K. As inspection of the animation suggests, there is considerable fluctuation in the identity of the shortest bonds. While it is not easy to infer from our figures, there is a clear (and expected) tendency for short bonds to occur in the denser volumes near a defect nucleus rather than in other parts of the network. Moreover, we computed the EDOS for a

”nonfilament” model and tried to relate it with the Urbach tail. We have also made similar animations for long bonds, and we see extended, highly connected filaments fluctuate into and out of existence. We illustrate the case of short bonds here, as there is less ambiguity in definition. Thus, we note that the filaments persist at room temperature at least[37], though not by retaining a static form, but with considerable temporal fluctuation.We illustrate these points with animations elsewhere[44].

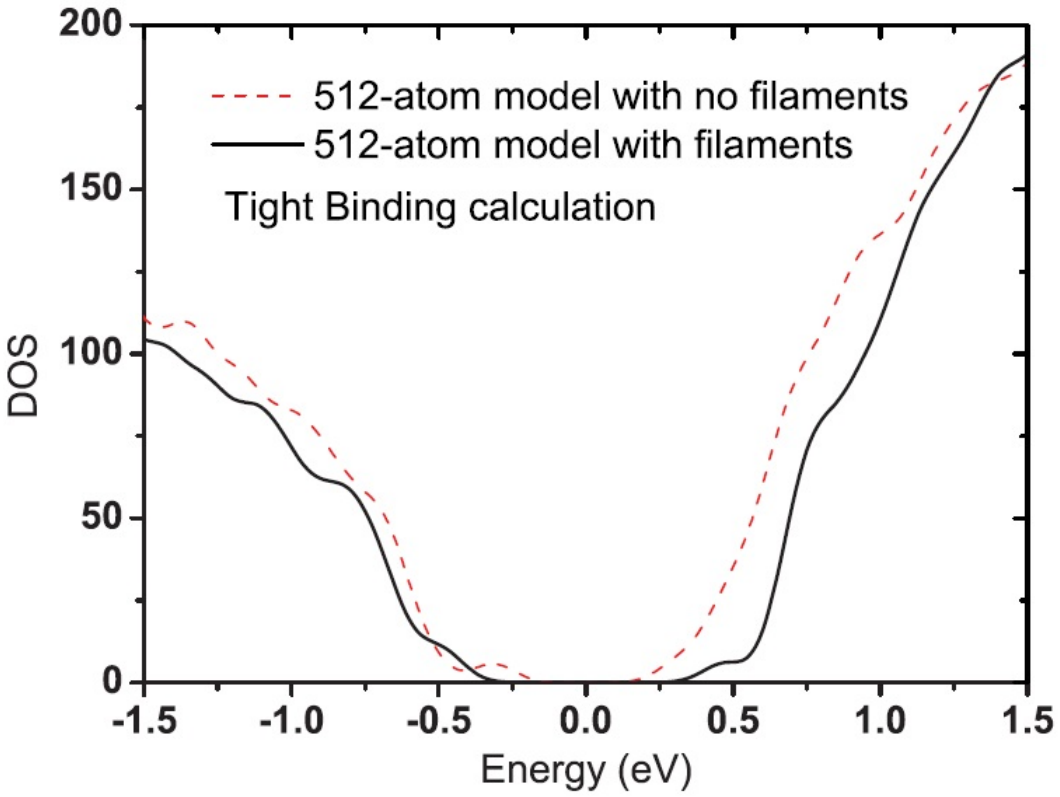

Figure 2.8: Electronic density of states for 512-atom models with and without filaments.

We end this section by comparing the EDOS of models with and without filaments. Two 512-atom α-Si models are presented: one with short and long filaments and the other without filaments[45]. We used the tight-binding method to compute the electronic density of states, and the results are plotted in Fig. 2.8. A clear band gap exists for the

configuration with filaments but a smaller gap is revealed for the model without filaments. Furthermore, we sought to understand the differences by performing exponential fits to tails in both models. Because of the incompleteness of the basis set for states above the Fermi level, we only fit the valence tail and we report the outcome in Fig. 2.9. We found that exponential fits for the structuralmodels with filaments are better than those without filaments. The Urbach energy, $E_U \approx 193$ meV, is essentially the same as that for the 100000-atom model for the model including filaments and is ≈ 99 meV for the model without filaments. Modification of the filaments leads to significant changes in the Urbach tail.

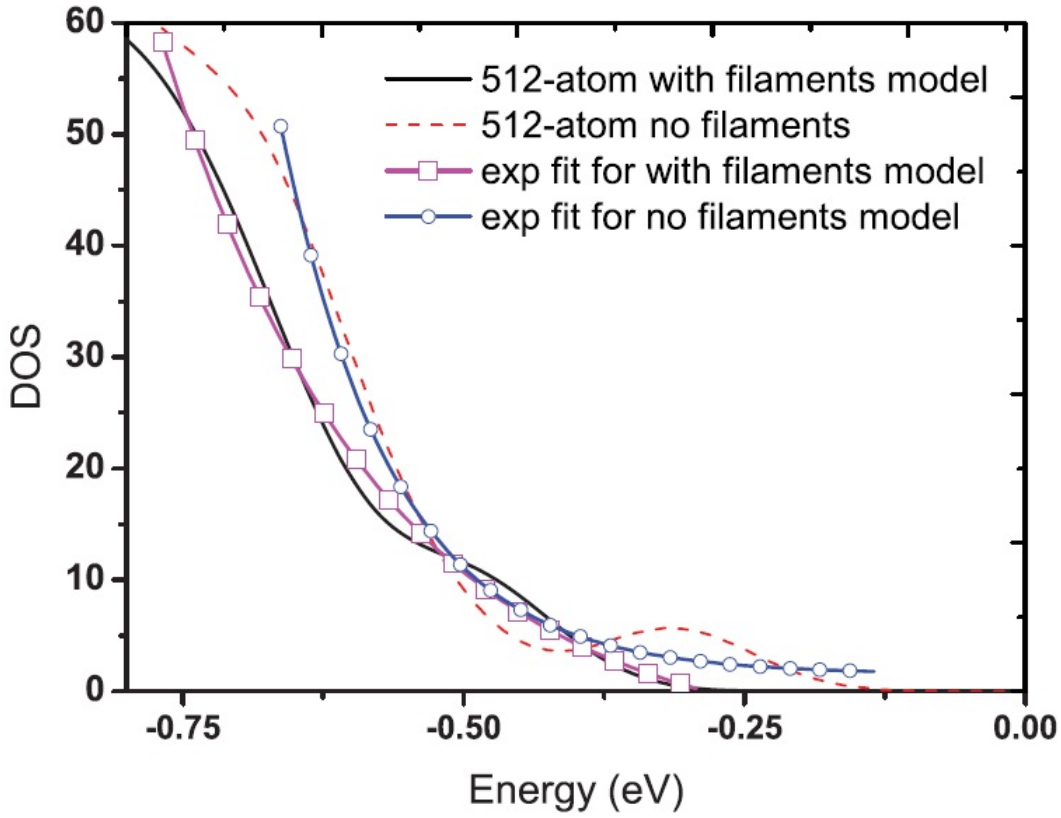

Figure 2.9: Exponential fitting for valence edges of 512-atom models with and without filaments.

2.6 Filaments under pressure

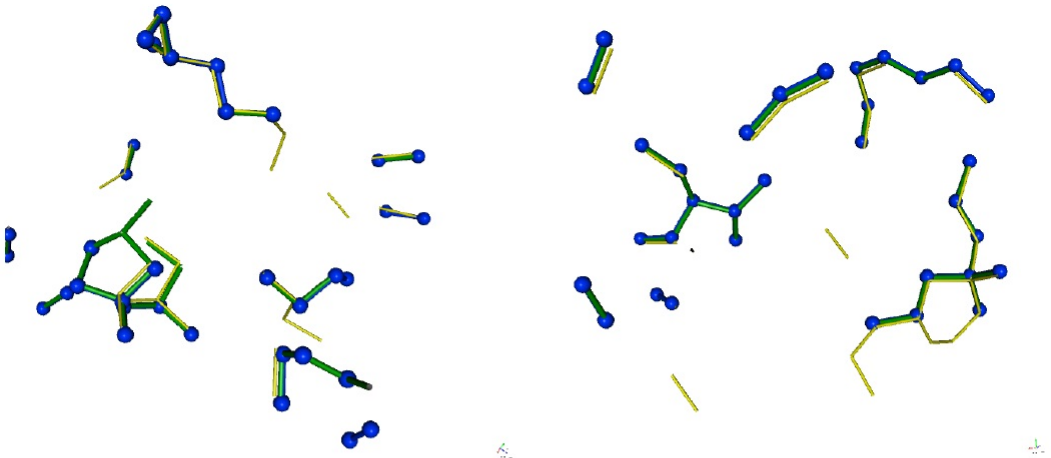

(a) short bonds in hydrostatic pressure (b) long bonds in hydrostatic pressure

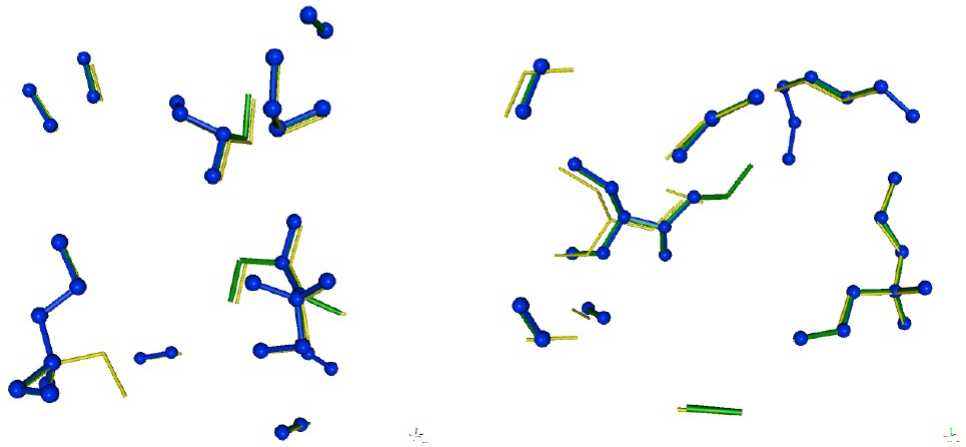

(c) short bonds in 1D pressure (d) long bonds in 1D pressure

Figure 2.10: Filaments in 512 a-Si under hydrostatic and one-dimensional pressure of 5Gpa. The green sticks represent the filaments from the system under external pressure, blue atoms illustrate the filaments in original 0Gpa model.

So far we study the response of filaments under different temperatures, now we focus on how filaments respond to the external pressure. This time the 512 a-Si was relaxed under hydrostatic and one-dimensional pressure of 1Gpa and 5Gpa.

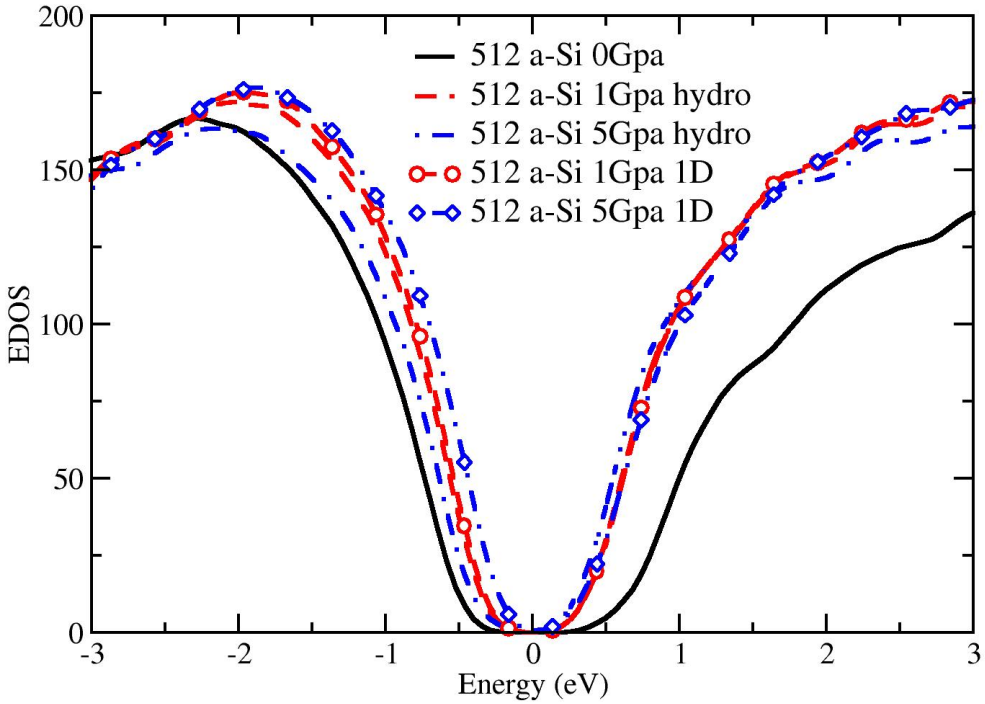

Figure 2.11: EDOS for 512 a-Si under hydrostatic and 1D pressure of 1Gpa and 5Gpa.

As shown in Fig 2.6, the filaments have spatial consistency after relaxed under external pressure, which is similar as the results of 512 a-Si from thermal MD. The filaments still tend to occur near especially long or short bonds. Also the fluctuation of filaments is not very significant after relaxed under the pressure. There are certain filaments which have more bonds than itself under 0 pressure, which is pretty natural since when the system was placed in the external pressure, the configuration would be compressed. Thus certain bonds near nucleus defect would be more sensitive to the external field, and some of the filaments grew bigger than the original model.

Next we compute the EDOS for the systems relaxed under pressure using SIESTA, with a SZ basis. As shown in Fig 2.11, similar as heating the system up, the external

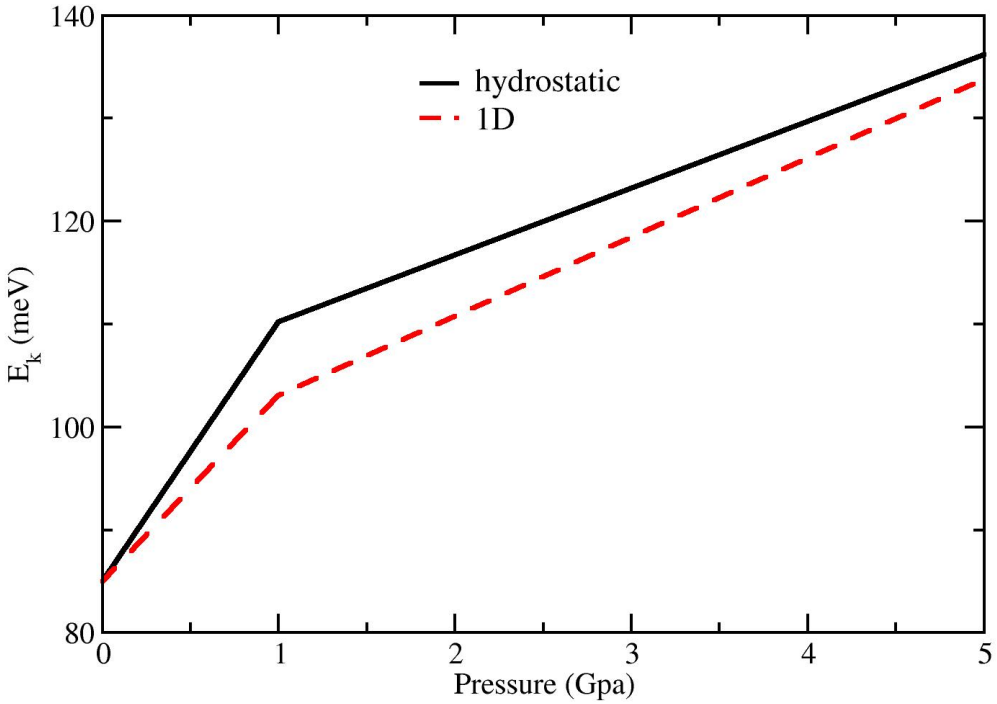

Figure 2.12: Correlation between Urbach energy (E_k) and pressure.

pressure also will close the gap, no matter whether the pressure is hydrostatic or 1D. After fitting the valence tails using Eq. 2.3, it seems there is a correlation between Urbach energy (E_k) with pressure. In Fig 2.12, for both hydrostatic and 1D external fields, the increasing of pressure will lead to the rising of E_k.

2.7 Necessity of Filaments

To test the relationship between band tails and the structure of the 512-atom amorphous silicon, every atom was randomly moved by δr ($|\delta r| \leq 0.01, 0.03$ and 0.05), which can be related with thermal fluctuation under certain temperatures (around 8.03K, 32.12K and 72.26K) [47]. After we introduce random distortion into the system, the

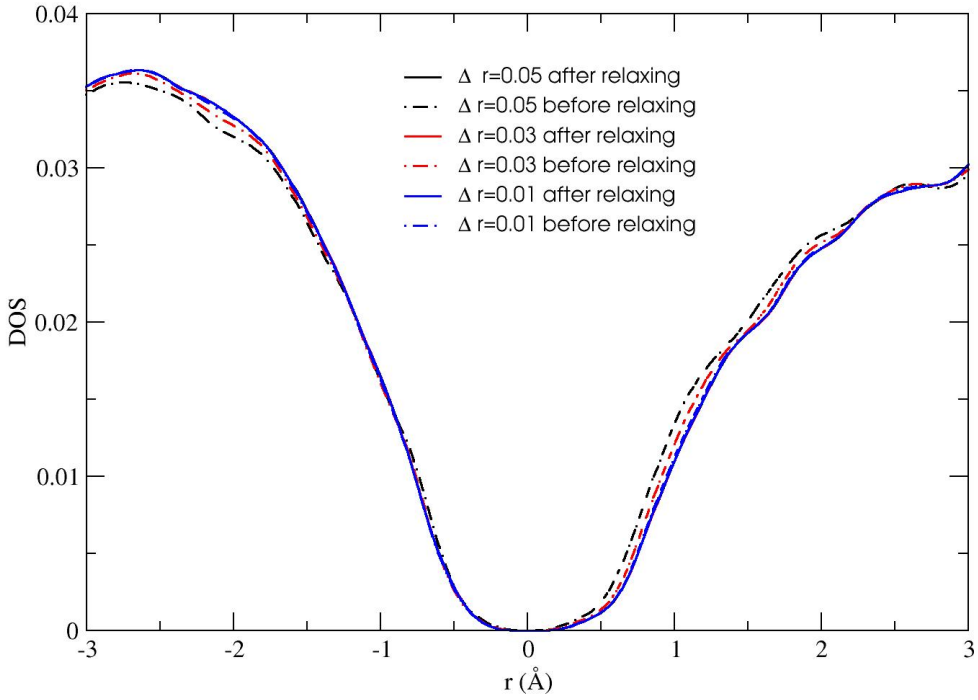

Figure 2.13: EDOS of 512 α-Si system with thermal disorder before and after relaxation around fermi level. The lines without symbols represent relaxed results, and unrelaxed models are illustrated by lines with symbols.

filaments become fewer with increasing of δr. These distorted structures are relaxed by SIESTA using a single-ζ polarized (SZP) basis and a double-ζ (DZ) basis. The final electronic density of states (EDOS) from these two calculations are similar, as both of them show an asymmetric broadening of the conduction tail with extra disorder, and little change in valence tail as shown in Fig 2.13, which is in agreement with the well-known fact that the conduction tail is more sensitive to thermal disorder than valence tail [48].

By further fitting the EDOS tails with an exponential function:

$$\rho(E) \propto e^{\frac{-|E-E_b|}{E_k}} \tag{2.3}$$

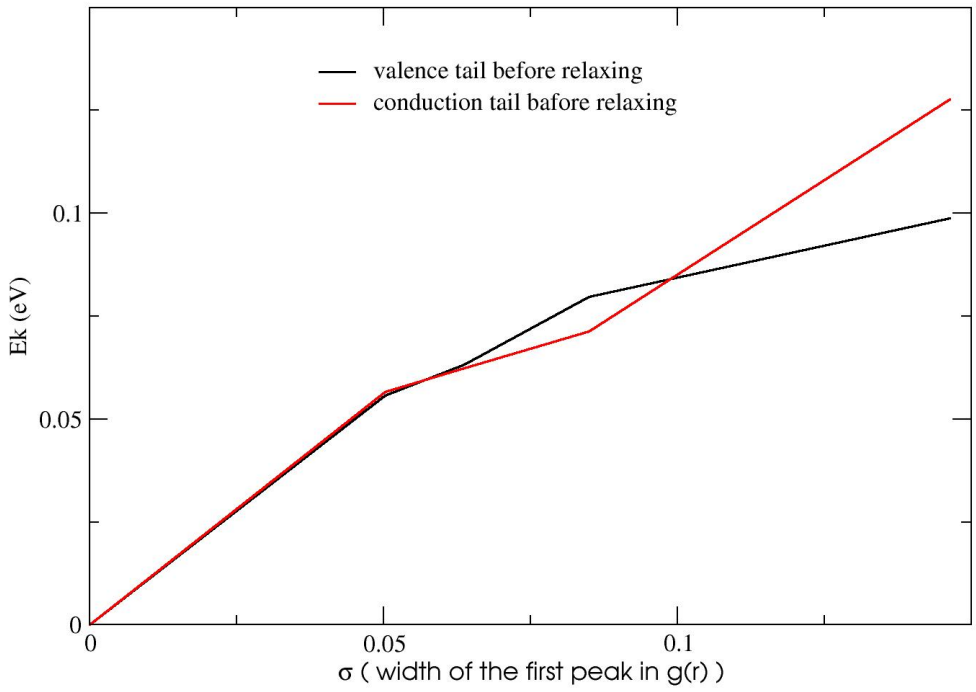

Figure 2.14: Correlation between initial disorder and the Urbach energy E_k. The solid line represents data of valence tail and the data of conduction tail is illustrated by dashed line.

Where E_b is the band-edge energy and E_k is the Urbach energy. In Fig 2.14, it seems there is a correlation between the initial disorder (illustrated by σ, which is the width of the first peak in radial distribution function (RDF g(r)) of the model) and E_k. It appears the more disorder is, the higher E_K will be, which implies the tail will look more and more sharp.

Also during the fitting, there is a clue to show that the fitting of Eq. 2.3 is better for the relaxed model than the initial model with disorder. It can be deduced that when the number of filaments decreases, the band tails (especially conduction tail) will become less exponential. However, in Fig 2.13, it is hard to tell whether the filaments will effect band tails or not.

2.8 Normal Mode Calculation

The phonon calculations were performed for 512-atom amorphous (512 α-Si) and cystalline silicon model (512 c-Si). The dynamical matrix was constructed by calculating forces of each atom from six orthogonal displacements by 0.04 Bohr using SIESTA. The vibrational density of states (VDOS) are given in Fig. 2.15. The calculation of VDOS for crystalline silicon is in great agreement with other publised results[46].

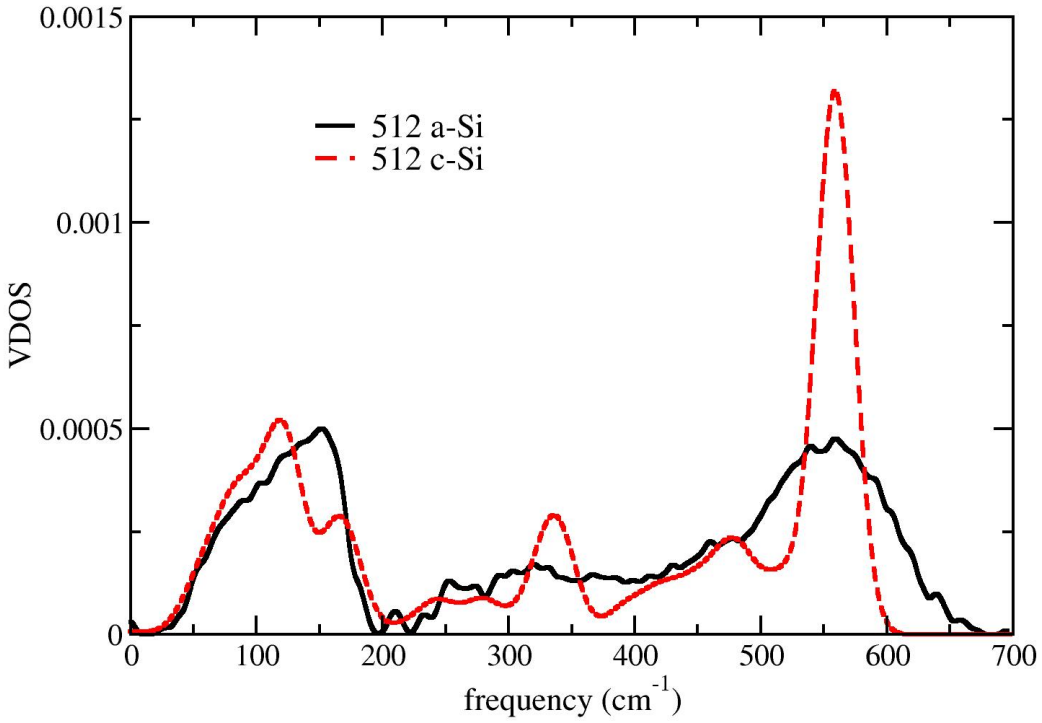

Figure 2.15: Normalized VDOS of 512 α-Si and c-Si models.

Inverse paricipation ratio (IPR) has been calculated for 512 α-Si model based on the phonon eigenvectors, as shown in Fig. 2.16. In the low-frequency range, there are a few localized states around $25cm^{-1}$. Take the state maked as 1 in Fig. 2.16 as example, this

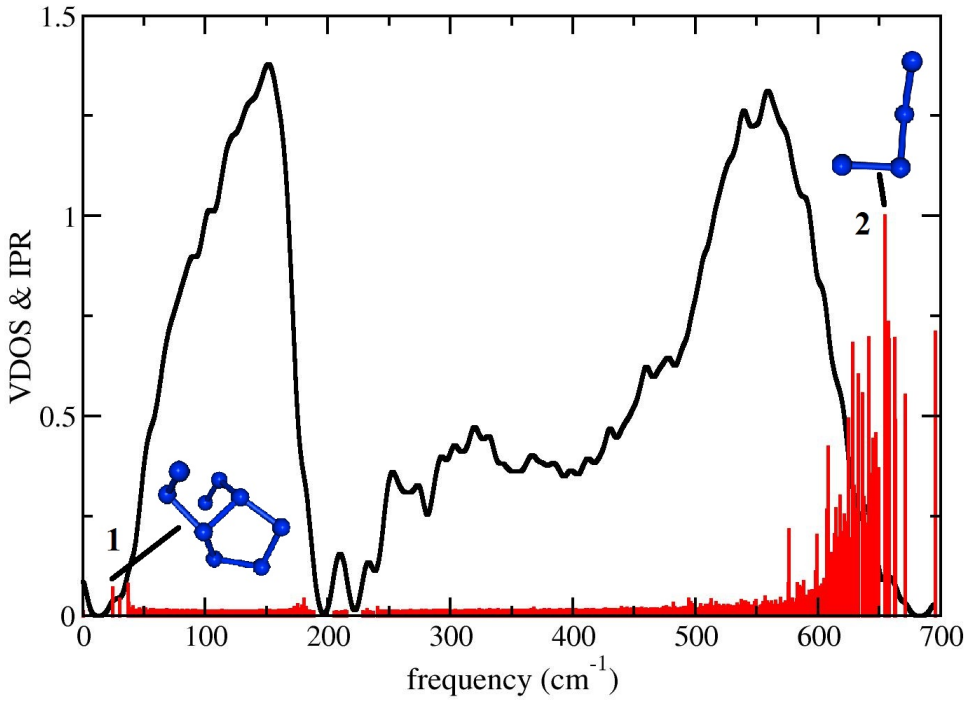

Figure 2.16: Scaled VDOS and IPR of 512 α-Si model. The atomic structure where each state is loclalized is shown by blue atoms.

state is localized on short bonds, whose average bond length is around 2.308Å, comparing to the average bond length of amorphous silicon (2.35Å). As illustrated in Fig. 2.16, these short bonds cluster togeter, forming a short-bond filament. Peak 2 in Fig. 2.16 is the most localized state in 512 α-Si model, which is localized on bonds with average bondlength 2.298Å. These atoms also interlink with each other. As shown in Section 2.3, the short bonds induces a strain field around them. Thus these strain field around short bonds may act as a phonon trap, leading to high localization around short bonds.

2.9 Conclusion

In this chapter, the existance of Urbach tails in large scale three dimensional configurations using tight-binding calculation is discussed. Also I present the character of the strain field centered on particularly short bonds, the effect of thermal disorder on the band tails and filaments. And finally vibrational density of states is discussed.

3 sp^2 PHASES OF CARBON

Part of the following work in Chapter 3 is published in Y. Li and D. A. Drabold, *Handbook of Graphene Science (CRC Press)* (submitted) 2013.

3.1 Introduction

Carbon-based semiconductors are one of the hottest topics in condensed matter science. Although silicon-based electronics have achieved tremendous success, scientists and engineers are always seeking alternative materials. One of the main reasons is that the size of silicon-based transistors, which are the building blocks of electronics, is reaching basic limits. One challenge of these short length scales is the requirement of rapid heat dissipation. Nowadays, remarkable improvements in growth techniques allow scientists to build carbon structure with reduced dimensionality in high precision. The advances in computational tools and theoretical models make it possible to investigate and make plausible predictions about the electronic, vibration or optical properties of carbon materials.

Single-layer graphene was first isolated by Novoselov et al. using mechanical exfoliation[49]. Graphene's two dimensional structure, which consists only of hexagons, gives rise to its unique and interesting electronic properties and promising potential for applications[50]. However, different categories of defects have to be taken into account for applications. It has been shown that these defects may lead to various graphitic arrangements, associated with a menagerie of local minima on the sp^2 carbon energy landscape. Among these analogs of graphite, we will briefly consider the properties of crystalline graphene, fullerene, carbon nanotubes and schwarzite, and focus mainly on amorphous graphene.

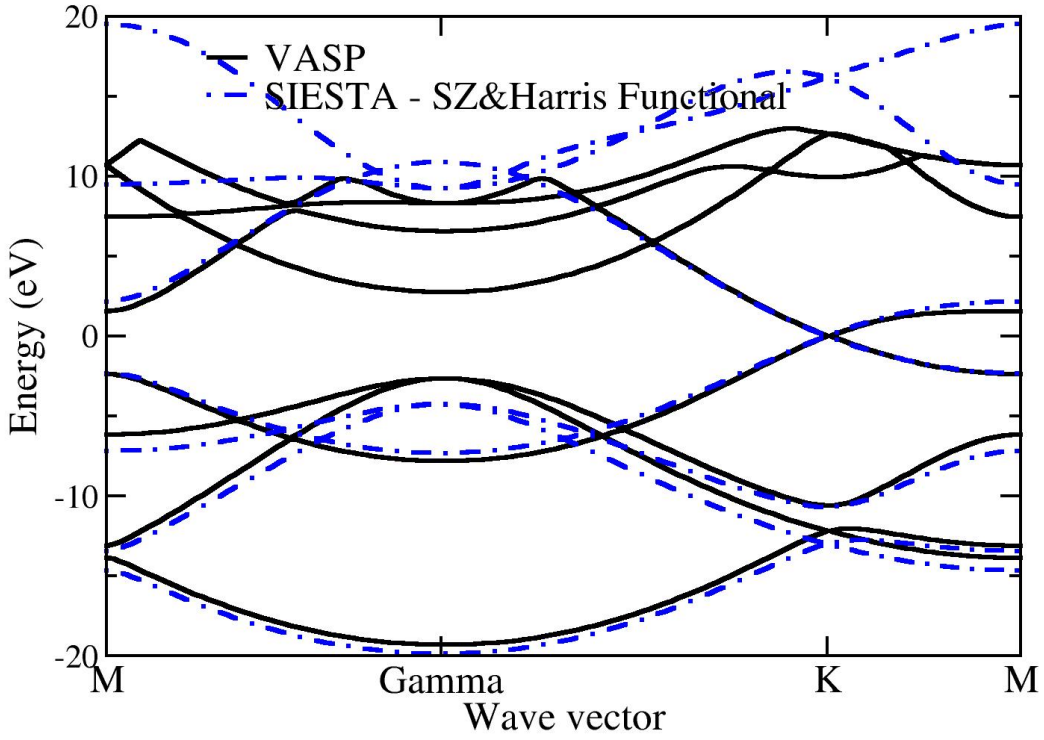

Figure 3.1: The density functional band structure of crystalline graphene. The result of VASP is given by solid line. The results by SIESTA using SZ basis and Harris functional is represented by the dash-dotted curve[57].

3.2 Crystalline Graphene

3.2.1 Band Structure

Crystalline graphene refers to one layer of graphite, where carbon atoms are arranged on a perfect honeycomb lattice. After experimental isolation in 2004, graphene's electronic properties have been predicted theoretically[49][51][52][53]. Since there have been extensive studies on crystalline graphene, here we will briefly discuss the electronic properties. To calculate the band structure of crystalline graphene, we employed a single-ζ

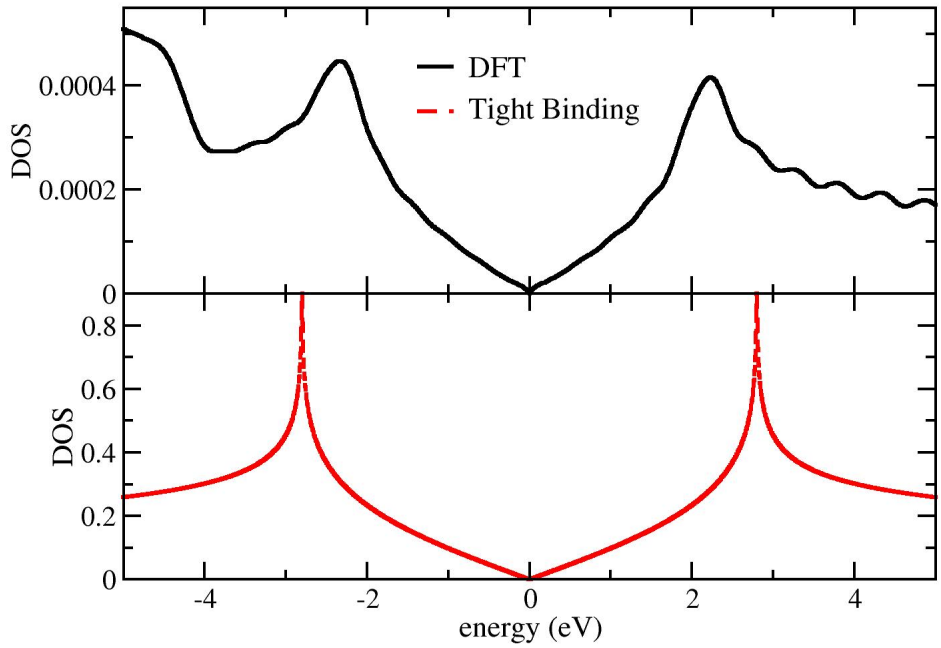

Figure 3.2: Density of states of 800-atom crystalline graphene using both DFT and tight-binding methods. The Fermi energy is 0eV. Solid line represents the result of SIESTA. The density of states due to tight-binding is shown by the dashed line.

(SZ) basis set with or without Harris functional[54], a double-ζ polarized (DZP) basis set with SIESTA, and also VASP to compute the eight lowest-energy bands. For both SZ and DZP calculations by SIESTA, 20 k-points along each special symmetry lines were taken, and for VASP 50 k-points along each line were sampled. The result from SIESTA using SZ basis and Harris functional is essentially identical with the one based on DZP basis for the four occupied bands. These results of SIESTA with SZ basis and Harris functional and of VASP show excellent agreement with published results for each code respectively[55][56], as shown in Fig. 3.1. For energies above the Fermi level, agreement of results for the four unoccupied bands are rather poor, which can be amended by

carefully choosing the energy cutoff to minimize the total energy as shown by Machon et al.[58]. While this is presumably irrelevant for ground state studies, these artifacts would be significant for transport or optics.

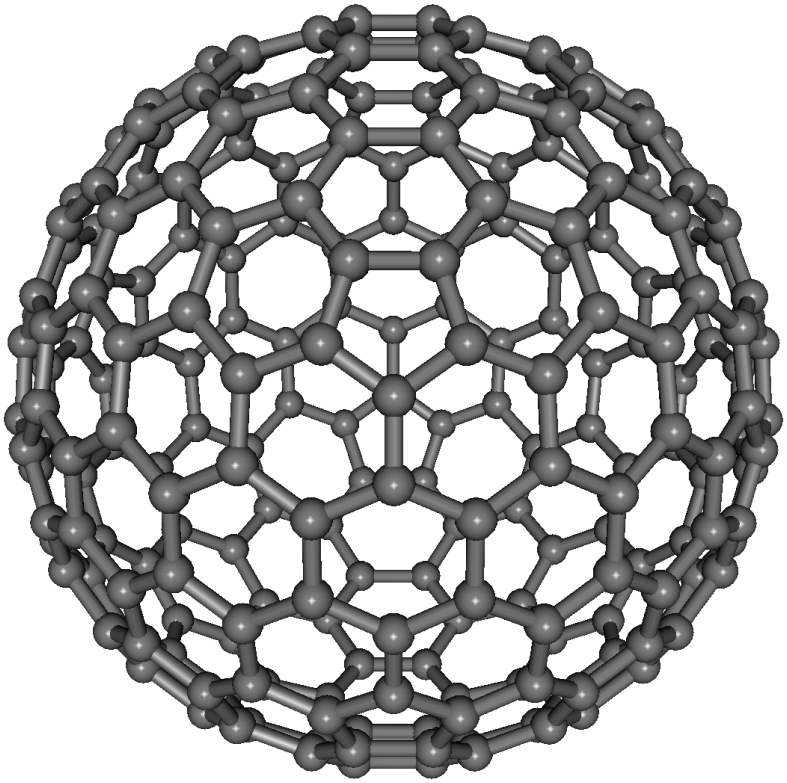

Figure 3.3: Optimized structure of C_{240} using SIESTA with SZ basis and Harris-functional.

3.2.2 Density of States

The comparison of density of states of crystalline graphene between DFT using SIESTA and tight-binding methods is shown in Fig. 3.2. The tight-binding result is calculated based on Eq. (14) in Ref. [50], where $t' = 0, t = 2.8eV$. Both of these two

results around Fermi level can be approximated as $\rho(E) \propto |E|$. The broadening of the DFT DOS is due to incomplete Brillouin Zone sampling.

3.3 Fullerenes

In 1985, Kroto et al. found that there exist cage-like molecules containing purely three-fold carbon atoms (sp^2 hybridization)[59], which are named fullerenes. This discovery stimulated extensive investigations into this molecular graphite allotrope. Generally speaking, fullerenes refer to a family of closed carbon cages formed by 12 pentagons and various numbers of hexagons, which can be prepared by the vaporization of graphite in an electric arc at low pressure[60]. In this section the electronic properties of C_{60} and C_{240} will be discussed. Their structures were optimized by SIESTA with SZ basis and Harris-functional without any symmetry constraints. The relaxed C_{240} model is shown in Fig. 3.3.

Table 3.1: The HOMO-LUMO gap and total energy relative to crystalline graphene of various fullerene and schwarzite models.

Allotropes	Models	Gap (eV)	E_{tot}/N_{atom} (eV)
Fullerene	C_{60}	1.724	0.402
	C_{240}	1.231	0.132
Schwarzite	G-384 schw	0.183	0.188
	P-536 schw	0.151	0.112
	P-792 schw	0.086	0.090
	P-984 schw	0.394	0.077

The comparison between DOS of these two fullerenes and crystalline graphene are shown in Fig. 3.4. It appears the curved topology of fullerene opens a gap around the Fermi level. According to Fig. 3.4 and Table. 3.1, the HOMO-LOMO gaps of C_{60} and

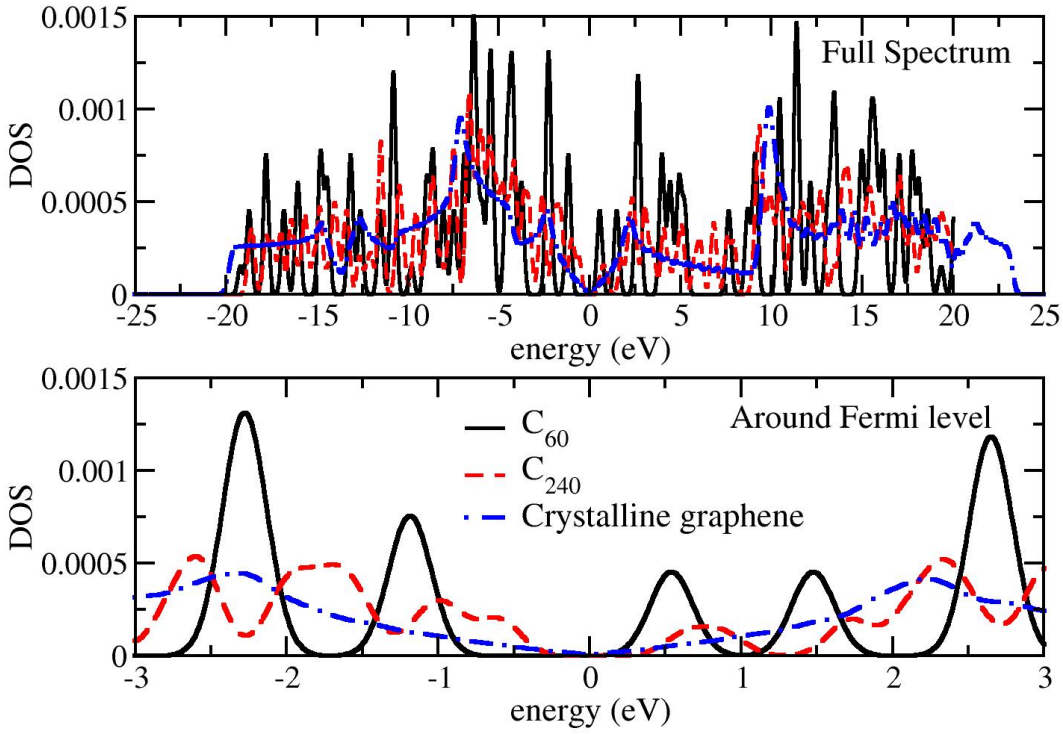

Figure 3.4: DOS of C_{60}, C_{240} and crystalline graphene. The upper panel shows the whole spectrum, and DOS around Fermi level is given in the lower panel.

C_{240} decrease with rising of the number of atoms, which is consistent with the other calculations[61].

3.4 Carbon Nanotubes

Carbon nanotubes can be visualized as a graphene sheet rolled into a cylinder. There are three different types of carbon nanotubes due to different ways in rolling the graphene sheet. Distinct geometry of these three types give rise to varied electronic behaviors[62]. Their structures can be characterized by a chiral vector $\vec{C}_h$ as shown in Fig. 3.5. Since

carbon nanotubes are derived from crystalline graphene, the geometric properties of a carbon nanotube are commonly described by the ones of graphene.

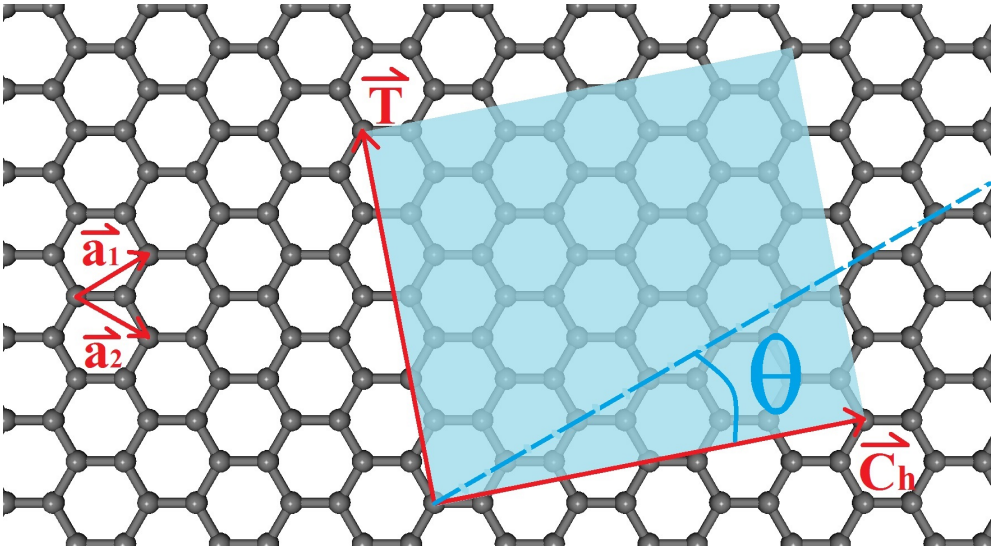

Figure 3.5: The chiral vector $\vec{C_h}$ shown in honeycomb lattice. $\vec{T}$ is the translation vector, representing the axial direction of the carbon nanotube. Shaded region represents the unit cell of carbon nanotube and Θ is the chiral angle. $\vec{a_1}$ and $\vec{a_2}$ are the lattice vectors of original honeycomb lattice.[63]

Recall that the two unit vectors in the honeycomb lattice are defined as $\vec{a_1} = \left(\frac{\sqrt{3}a}{2}, \frac{a}{2}\right)$ and $\vec{a_2} = \left(\frac{\sqrt{3}a}{2}, -\frac{a}{2}\right)$, where $a \approx 1.42$Å. To represent the geometry of carbon nanotube according to the original honeycomb lattice, chiral vector $\vec{C_h}$ defines the diameter of carbon nanotube, and translation vector $\vec{T}$ defines the axial direction along the nanotube. Both of them are expressed as:

$$\begin{aligned} \vec{C_h} &= n\vec{a_1} + m\vec{a_2} \\ \vec{T} &= \frac{2m+n}{d_r}\vec{a_1} + \frac{-2n+m}{d_r}\vec{a_2} \end{aligned} \tag{3.1}$$

Here both m and n are integers and $n > m$. d_r is the highest common divisor of $(2n + m, 2m + n)$. (n, m) values are crucial to the properties of nanotubes. N anotubes with the same number of unit vector indices (n, n) are called armchair nanotubes. Chiral vector indices $(n, 0)$ with $m = 0$ represents the zigzag nanotubes. Besides these two cases, if the

chiral vector indices (n, m) are $n \neq m \neq 0$, the nanotube is called chiral, with a screw symmetry along the axis of the tube[64]. A few examples of these three types of nanotubes are shown in Fig. 3.6.

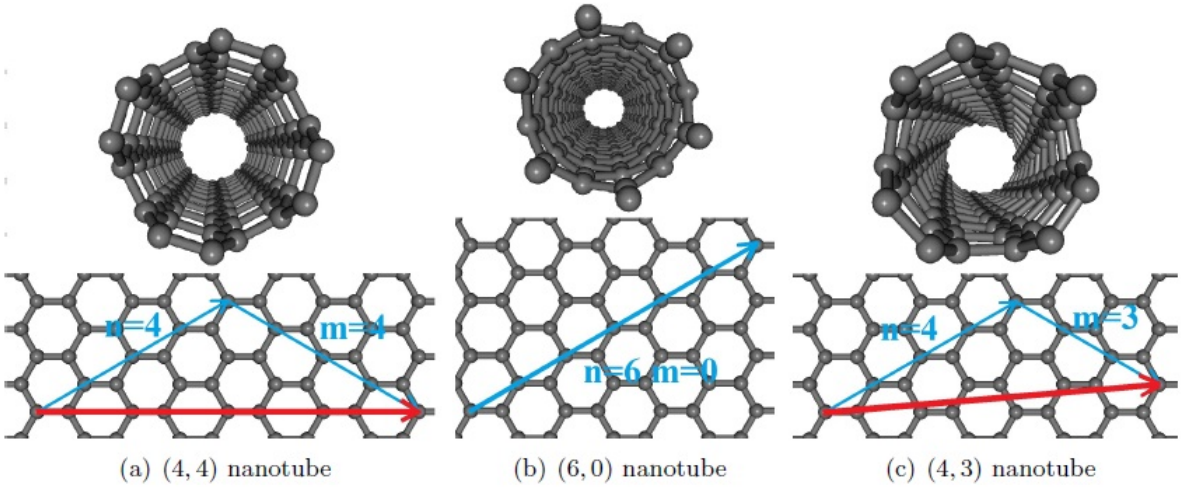

Figure 3.6: Three examples of carbon nanotubes with chral vector indices $(4, 4)$, $(6, 0)$ and $(4, 3)$ respectively.

To evaluate the electronic properties of carbon nanotubes, we use three carbon nanotubes with different chiral vector indices: (4,4) tube with $n = m = 4$, (6,0) tube with $n = 6, m = 0$, and (4,3) tube $n = 4, m = 3$. Carbon nanotubes exhibit either metallic behavior or as semiconductor depending on their chiral indices. Theoretical derivations show that if the indices (n, m) of nanotube satisfy the greatest common divisor of (n-m, 3) is 3, the given carbon nanotube behaves like metal, otherwise, it will be a semiconductor[63]. The Γ point DOS calculation results using SIESTA with SZ basis are shown in Fig. 3.7. Consistent with the theory, (6,0) tube has more states around the Fermi level, and obviously is metallic, and (4,3) tube exhibits a gap and is a semiconductor. On the other hand, the (4,4) tube which should be metallic exhibits a gap. In our case, we found SIESTA calculations with SZ basis always tend to overestimate the gap, due to

incomplete basis set and Brillouin Zone sampling. By carefully choosing the basis set and fully integraing over the Brillouin Zone, the gap would be reduced. Details on this calculation will be discussed elsewhere.

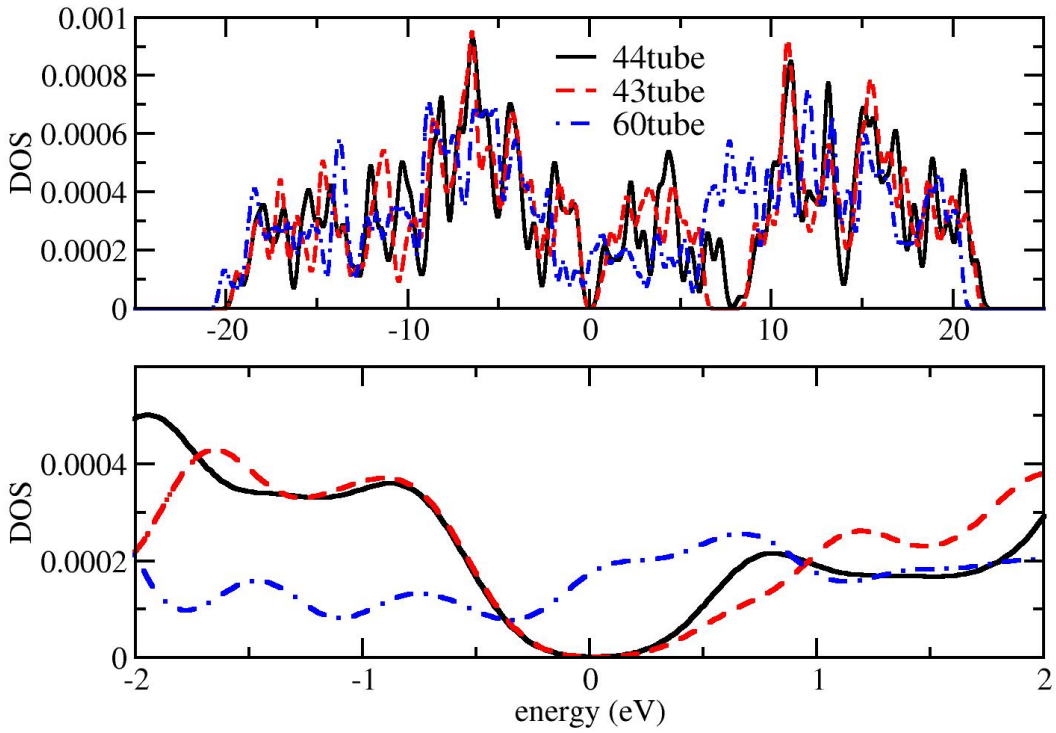

Figure 3.7: Normalized DOS of (4,4) tube, (4,3) tube and (6,0) tube. Fermi level is 0 eV. The full spectrums are shown in the higher panel, and lower panel shows in the zooming-in structures around the Fermi level.

We also compute the Γ ($\overrightarrow{k} = 0$) density of states using a similar approach for carbon nanotubes. Here we use one zigzag (30,0) tube and one armchair (40,40) tube. According to the law of greatest common divisor of $(n - m, 3)$, (30,0) tube should be metallic, which is consistent with our results as shown in Fig. 3.8. Also, by comparing the contributions from all three sp^2 orbitals and the p orbital, PDOS on p orbital have significant weight

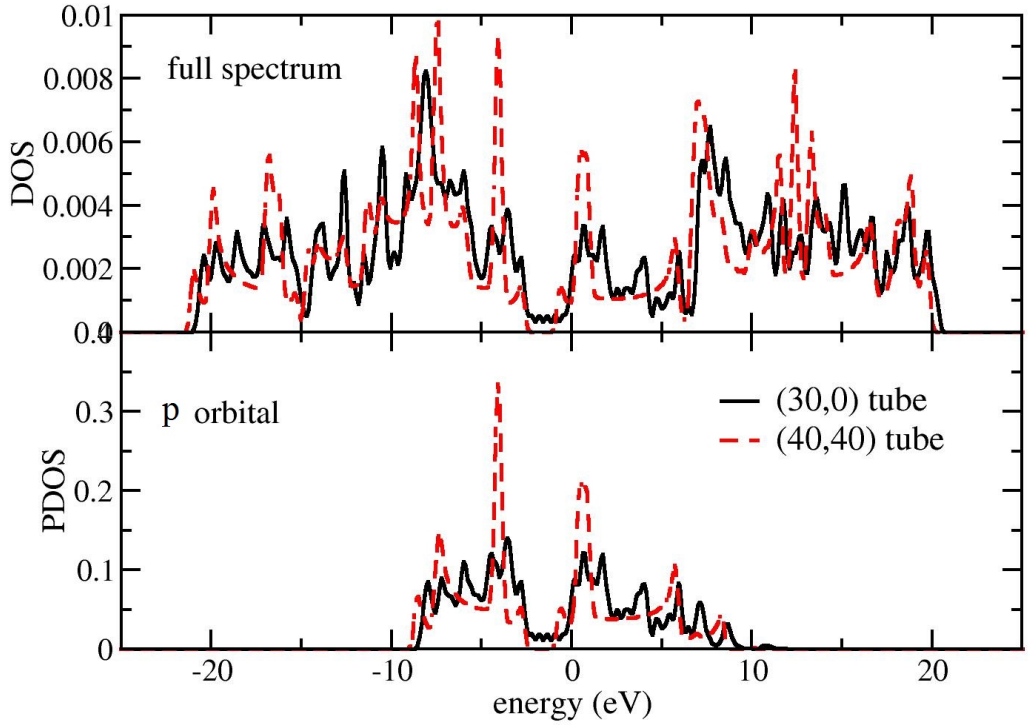

Figure 3.8: Comparison between density of states (DOS) and projected density of states (PDOS) of (30,0) tube and (40,40) tube.

around Fermi energy. And in Fig. 3.8, the PDOS curves of p orbitals in (30,0) tube and (40,40) tube have identical shape with the DOS around the Fermi level. Thus the electronic properties around the Fermi level is determined by the interaction between p orbitals. This result is in fine agreement with bandstructure calculations, in which the two π bands, which are due to the interaction between p orbitals, determine the metallic behavior of carbon nanotubes[63].

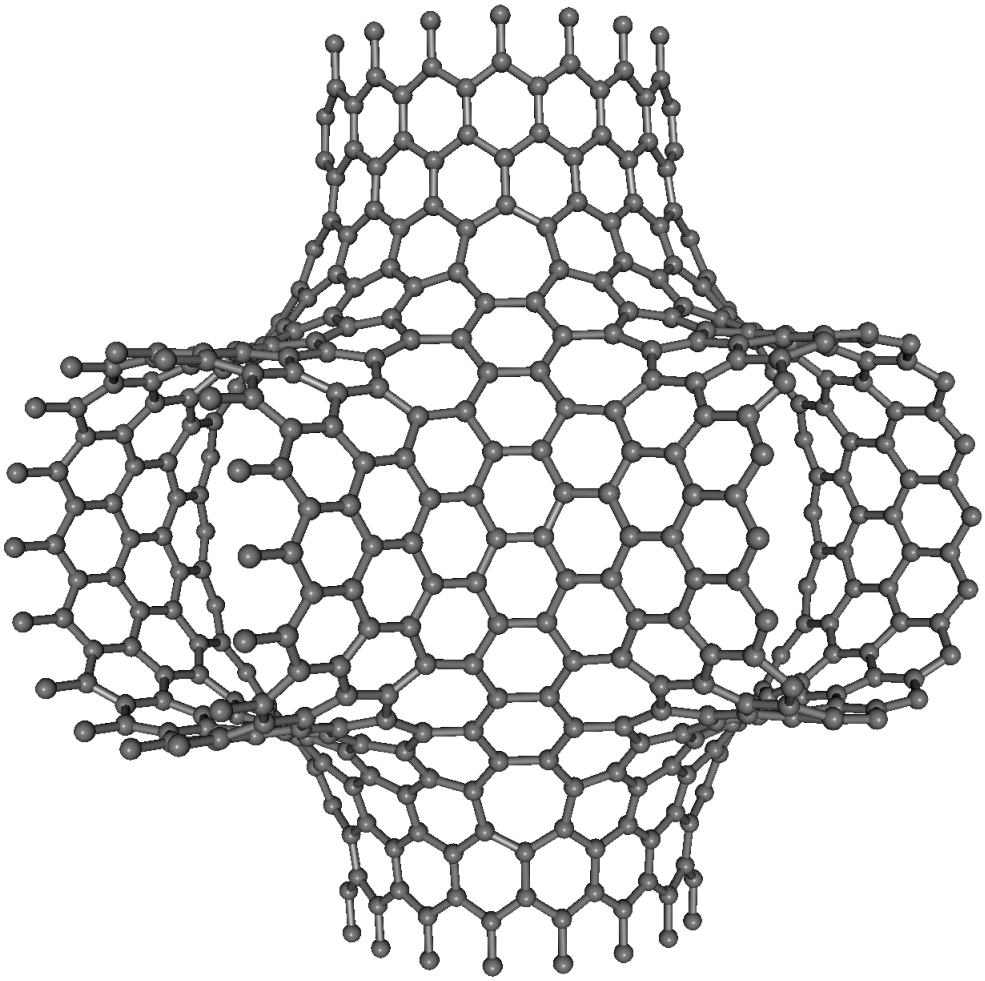

Figure 3.9: Structure of primitive 792-atom schwarzite model. Only half of this model is shown here[67].

3.5 Schwartzite

Unlike fulllerenes and carbon nanotubes, which have positive Gaussian curvature due to the presence of five-membered rings, schwarzites have negative curvature, which are induced by seven and eight-membered rings as shown in Fig. 3.9. As in crystalline graphene, all the atoms of schwarzite are three-fold[65]. To study the electronic properties of schwarzite, four models are used: gycoid 384-atom (G-384 schw), primitive 536-atom

(P-536 schw), primitive 792-atom (P-792 schw) and primitive 984-atom (P-984 schw) schwarzite models. DOS of these four models are calculated by SIESTA using SZ basis and Harris-functional with at least $2 \times 2 \times 2$ Monkhorst-Pack grid[66]. The calculation results are given in Fig. 3.10.

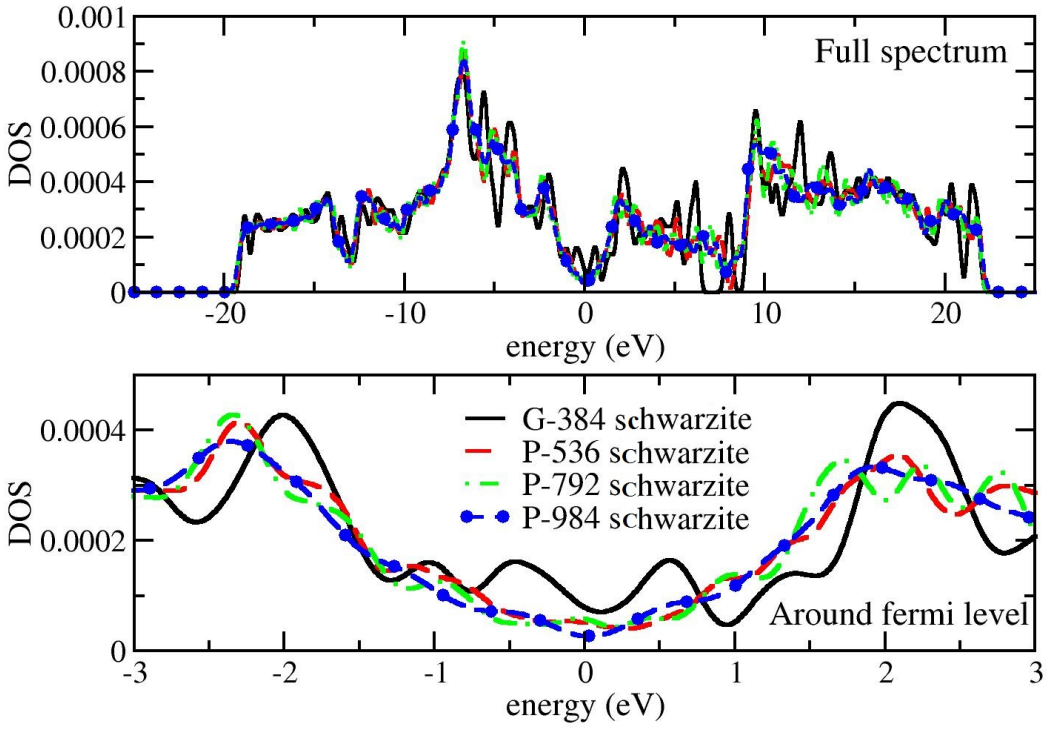

Figure 3.10: Normalized density of states (DOS) of four schwarzite models. Fermi energy is 0eV.

As shown in Fig. 3.10, with increasing schwarzite unit cell, DOS curve near fermi level approaches to the shape obtained for crystalline graphene as shown in Fig. 3.2. According to Table 3.1, increase of the schwarzite cell also leads to decline of HOMO-LUMO gap. However, the trend breaks at P-984 schw. The total energy per atom

also decreases with increasing unit cell size. And the difference in total energy between crystalline graphene and large schwarzite cell approaches to 0.077 eV, which implies there is a great chance to prepare real schwarzite models.

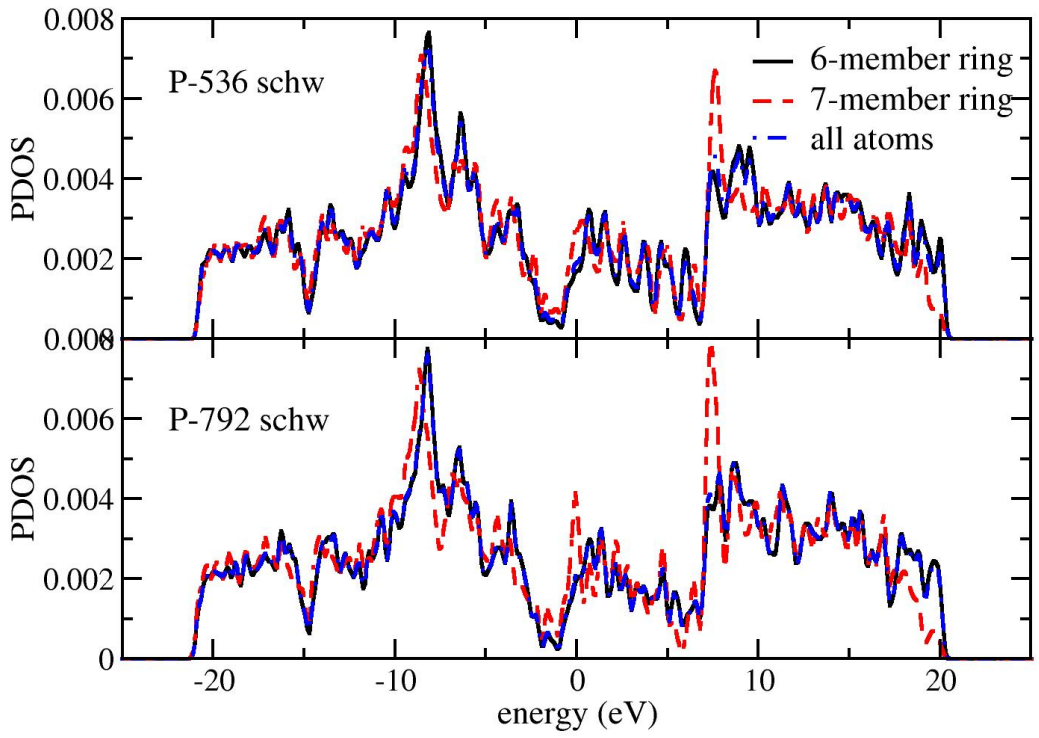

Figure 3.11: PDOS of P-536 and P-792 schw models on 7-member and 6-member rings, and the DOS represent by the dot-dashed lines.

The calculations of Γ point PDOS of both P-536 and P-792 schwarzite models have been performed. Since the primitive schwarzites contain only 6-member and 7-member rings, and the negative curvature is introduced by 7-member rings, here we compare the PDOS on the atoms within 7-member rings and the ones with 6-member rings, as shown

in Fig. 3.11. It appears that for both of these two models, 7-member rings are responsible for the structure of the DOS around the Fermi level.

3.6 Conclusion

In summary, positive curvature opens up HOMO-LUMO gap in fullerenes. For carbon nanotubes, their electronic properties strongly depend on the chiral indices. On the other hand, the influence of negative curvature on DOS is reduced by increasing schwarzite unit cell size, and the difference of DOS between large schwarzite and crystalline graphene diminishes. For both positively and negatively curved carbon allotropes, the bigger the closed cage is, the lower the total energy per atom will be.

4 Amorphous Graphene

The following work in Chapter 3 is published in Y. Li, F. Inam, A. Kumar, M. F. Thorpe and D. A. Drabold, Phys. Stat. Sol. B **248**, 2082 (2011), Y. Li and D. A. Drabold, Phys. Stat. Sol. B **250**, 1012 (2013), Y. Li and D. A. Drabold, *Handbook of Graphene Science (CRC Press)* (submitted) 2013, and Y. Li, and D. A. Drabold, *Electronic Signatures of Topological Disorder in Amorphous Graphene* (submitted) 2014.

As mentioned in the introduction, crystalline graphene and associated materials have extraordinarily interesting electronic properties. The electronic, thermal, and vibrational properties of graphene depend sensitively on the perfection of the honeycomb lattice. Thus it is worthwhile investigating defects in graphene. Although extensive efforts have been devoted to curved graphene derivatives such as carbon nanotubes and fullerenes, little attention has been given to non-hexagonal defects and their electronic and vibrational properties in a planar graphene. In this section, details about the progress in producing real amorphous graphene samples in experiment, techniques on preparing computational models and calculation results about electronic and vibrational properties of amorphous graphene will be discussed.

4.1 Experimental results

From the 1980's, the progress in the growth engineering and characterization techniques made it possible to grow low dimensional materials under tight control. Recent electron bombardment experiments have been able to create amorphous graphene pieces[68][69]. Clear images of regions of amorphous graphene have been taken by Meyer[70], following the method described in Ref[71].

Recently Kawasumi *et al.* successfully embeded non-hexagonal rings into a crystalline graphene subunit in experiment, synthesized by stepwise chemical methods, isolated, purified and fully characterized the material spectroscopically[72]. They reported

the multiple odd-membered-ring defects in this subunit lead to non-planar distortion, as shown in Fig. 2 in [72], which is consistent with our published results, as described in following sections.

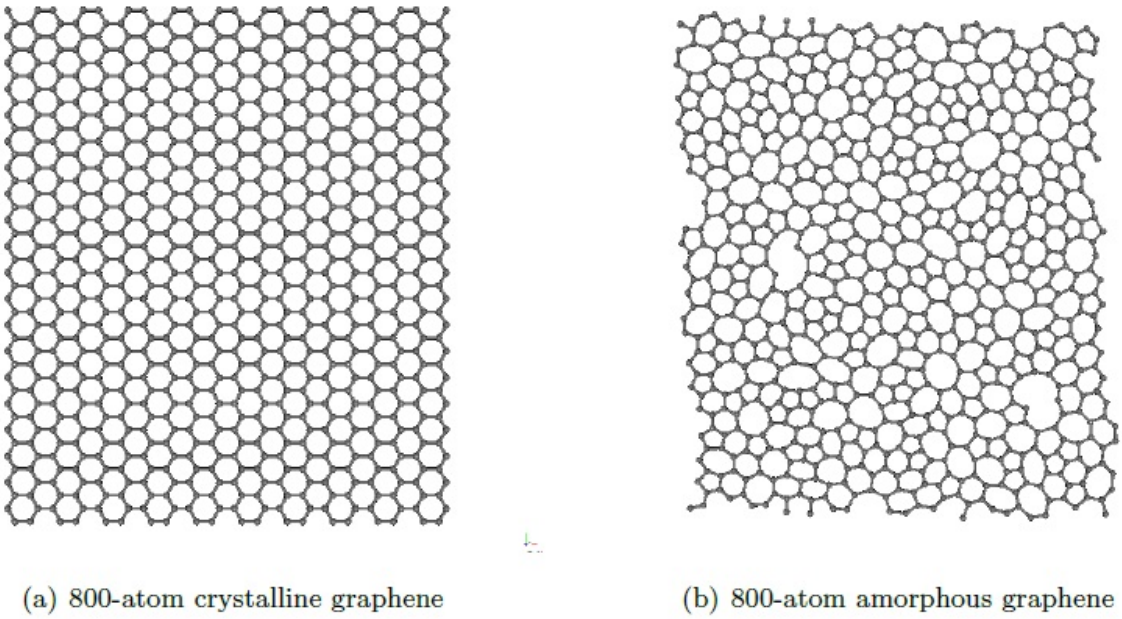

(a) 800-atom crystalline graphene (b) 800-atom amorphous graphene

Figure 4.1: Top view of 800-atom crystalline and 836-atom amorphous graphene[57].

4.2 Amorphous Graphene Models

To investigate the electronic and vibrational properties of amorphous graphene, three models are employed: 800 atom model (800 a-g), two 836 atom models (836 a-g1 and 836 a-g2). All these models are prepared by introducing Stone-Wales (SW) defects[73] into perfect honeycomb lattice and a Wooten-Weaire-Winer (WWW) annealing scheme[74] with varying concentration of five, six and seven member rings[57]. Their ring statistics are shown in Table 4.1. All the atoms in these models are threefold, forming a practical realization of the continuous random network (CRN) model, proposed by

Zachariasen[75]. A comparison between crystalline graphene and 836 a-g1 model is shown in Fig. 4.1.

Table 4.1: Ring statistics of 800 a-g, 836 a-g1 and 836 a-g2 models, shown as %[57].

Ring Size	800 a-g	836 a-g1	836 a-g2
5	33.5	25	24
6	38	53	52
7	24	19	25
8	4.5	3	0

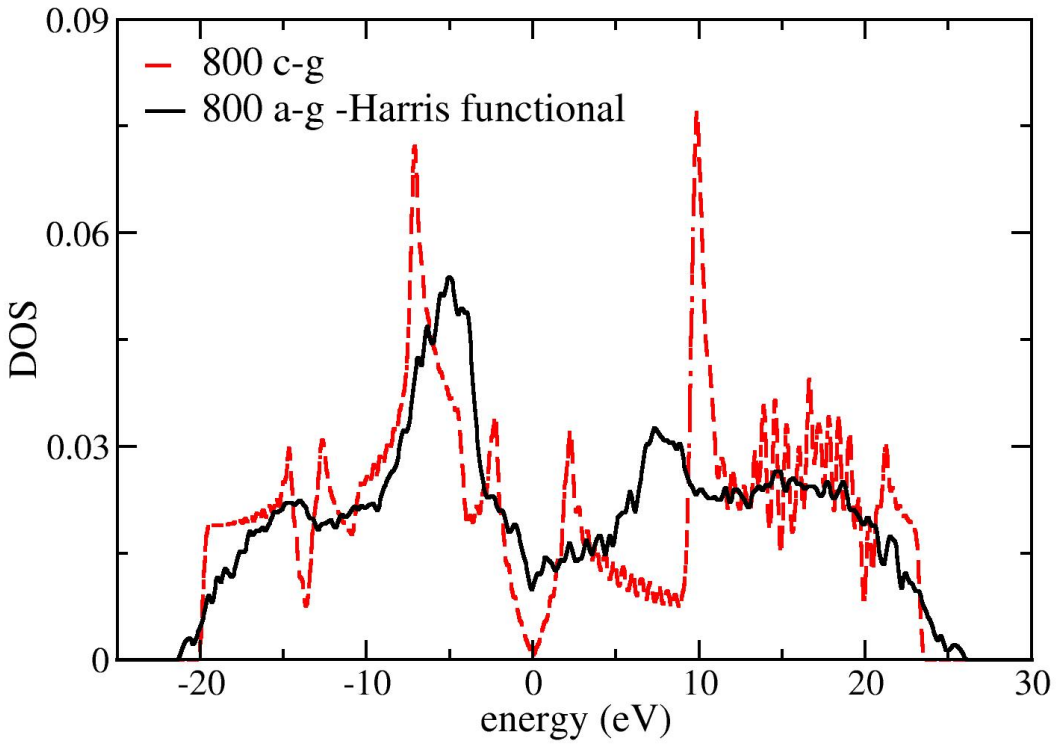

Figure 4.2: DOS of 800-atom amorphous and crystalline graphene, the Fermi energy is 0 eV[57].

The electronic DOS of the planar 800 a-g model is compared to a Γ point DOS of the crystalline 800 c-g model in Fig. 4.2 due to SIESTA. The electronic structure of the 800 a-g model is vastly different from the crystalline graphene near the Fermi level due to the presence of ring defects, as first reported by Kapko et al.[76].

4.3 Pentagonal Puckering

In all three amorphous graphene models, we introduced small random fluctuations in the coordinates, in the direction normal to the graphene plane, and then relaxed with the Harris functional and a SZ basis set. Starting with a flat sheet, the planar symmetry breaks with curvature above or below initial the plane. The final distortion depends on the initial conditions. However, a consistent theme emerges of pentagons inducing curvature as we describe below.

Table 4.2: the influence of δr on 800 a-g system relative to initial flat model

δr (Å)	$\overline{\delta r'}$ (Å)	E_{tot}/N_{atom} (eV)
0.01	0.520	-0.107
0.05	0.525	-0.107
0.07	0.526	-0.107

Table 4.3: the influence of δr on 836 a-g1 system relative to initial flat model

δr (Å)	$\overline{\delta r'}$ (Å)	E_{tot}/N_{atom} (eV)
0.01	2.53E-3	0.0
0.05	1.402	-0.102
0.07	1.401	-0.102

As shown in Table 4.2, Table 4.3 and Table 4.4, first we randomly moved the atoms along normal direction in the range of $[-\delta r, +\delta r]$, as shown in the first column of these

Table 4.4: the influence of δr on 836 a-g2 system relative to initial flat model

δr (Å)	$\overline{\delta r'}$ (Å)	E_{tot}/N_{atom} (eV)
0.01	2.72E-3	0.0
0.05	1.183	-0.090
0.07	1.180	-0.090

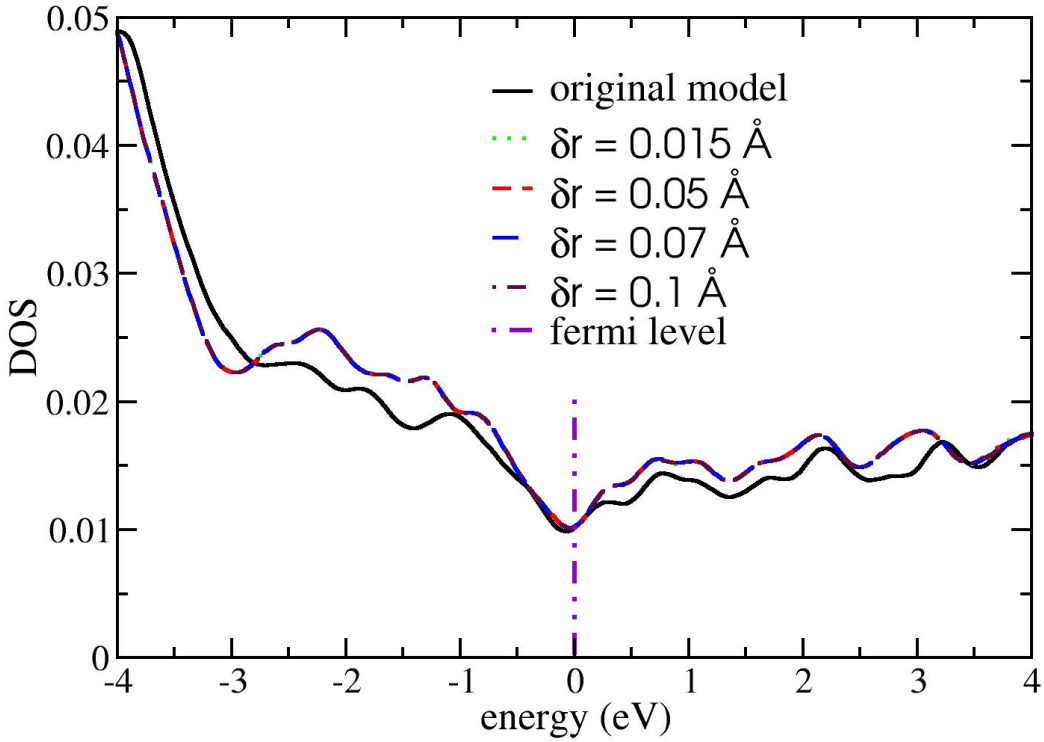

Figure 4.3: Density of states of the original and relaxed crinkled system. a) The solid line is the density of states of original 800-atom amorphous graphene model. b) The density of states of crinkled systems are shown as marked in the plot. c) The Fermi level is corrected to $0eV$ in the plot, as shown in dot-slash line.

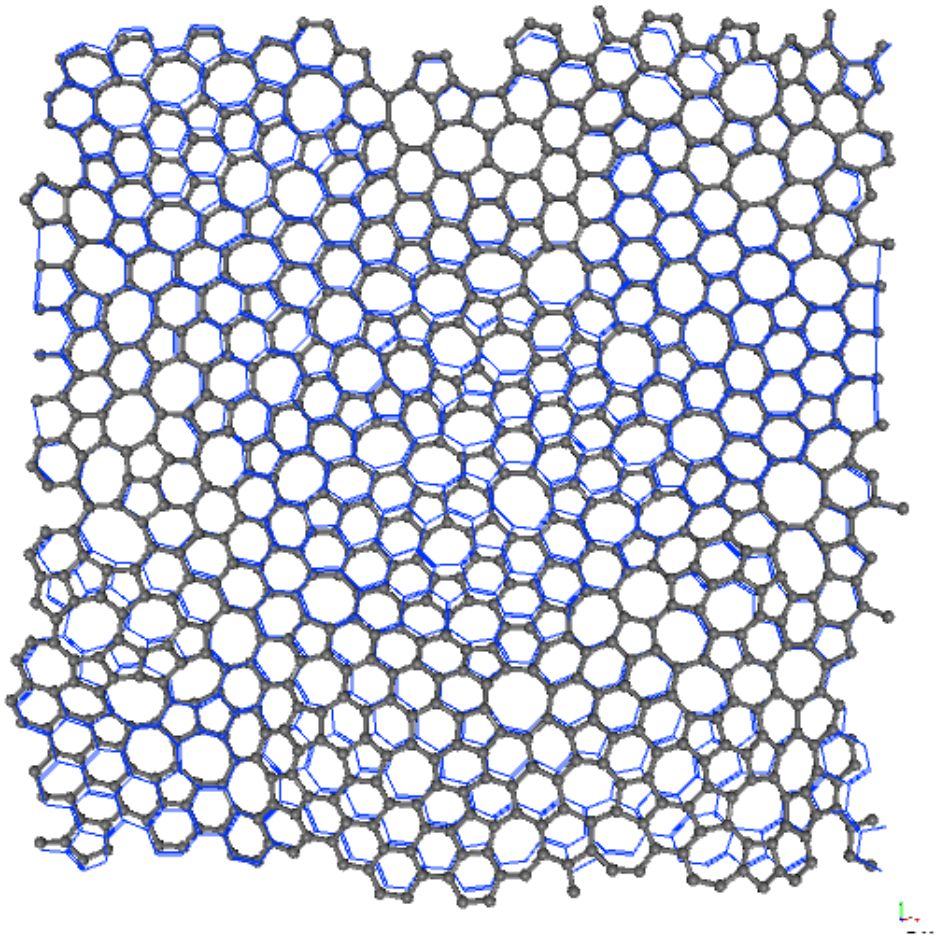

Figure 4.4: The flat view of the relaxed 836 a-g1 system (in gray). The blue background illustrates the original 836 a-g1 model.

tables; and the results of relaxing by SIESTA in SZ basis are shown in the second, third and fourth columns. The prime symbol refers to the relaxed model. Taking the 800 a-g model as an example, the influence of puckering the system on the density of states around Fermi level is shown in Figure 4.3; an intuitive view of the fluctuation after relaxing is shown in Figure 4.4 and 4.5 when $\delta r = 0.05$Å. After breaking the planar symmetry by a tiny amount, say $\delta r = 0.05$Å, all three models pucker and form the rippled or undulated structure as shown in Figure 4.4 and 4.5.

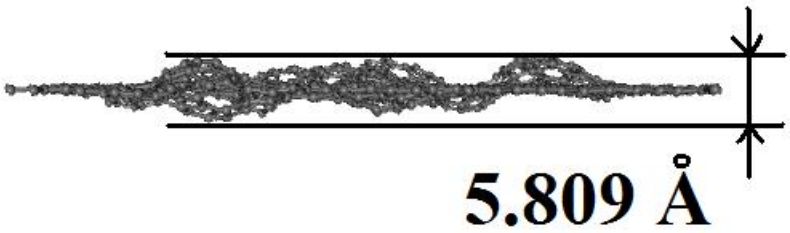

Figure 4.5: The side view of the relaxed 800 a-g system. The biggest separation along normal direction is marked in the plot.

The radial distribution function $g(r)$ is shown in Figure 4.6. From this plot, the mean bond length of the relaxed systems with different initial δr remain near 1.42Å, the change in ring statistics after relaxing is also not significant. And according to Fig 4.4, only one bond broke after relaxation. This implies that the main difference between the original amorphous graphene model and the relaxed ones is due to these undulations in Figure 4.4.

To compare with the puckering of the 800 a-g model, we also introduced the same planar symmetry breaking into a 800 c-g model and relaxed it. As expected, the atoms in this crystalline system maintained planar symmetry.

Also in order to find the relation between the ripples in the relaxed systems and the initial random distortion, we tested different seeds in random number generator (RNG) and also different RNG. The results reveals that the changing seeds or or employing different RNG are quantitatively small: The maximum mean distortion from the original flat plane ($\overline{\delta r'}$) is about 0.545Å and the maximum change in total energy is around $0.01eV$ per atom. Figure 4.7 shows the side view of the final configurations by using new and original RNG when $\delta r = 0.05$Å, we can tell that the rippled regions are similar, except certain regions have formed ”bucky domes” on opposite sides of the initial plane.

To further test the relation between the ripples and the initial distortion, instead of randomly moving all the atoms of 800 a-g, we only distorted the atoms within pentagons

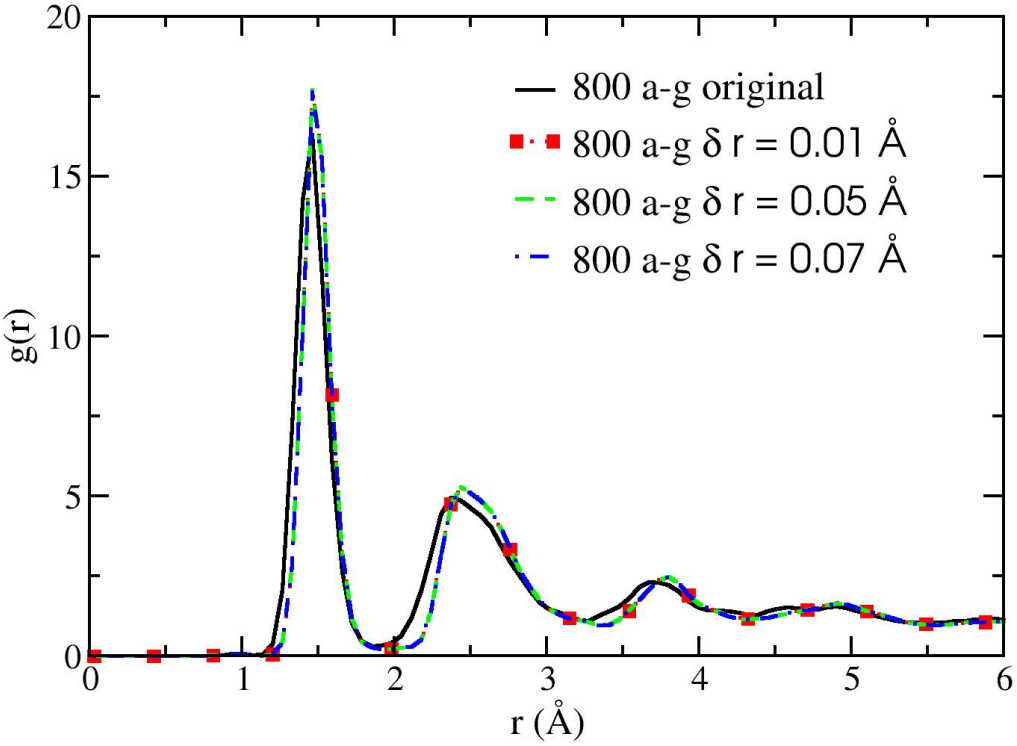

Figure 4.6: Radial distribution function of flat and crinkled 800 a-g system.

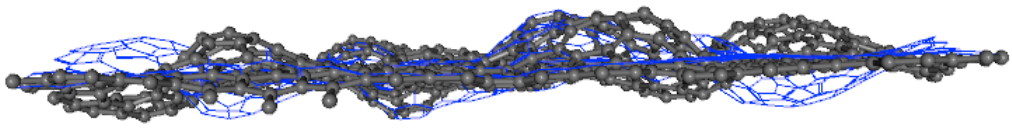

Figure 4.7: The side view of the final configuration by using new and original RNG. a) The gray balls and sticks show the result of new RNG. b) The blue frames represent the result of original RNG.

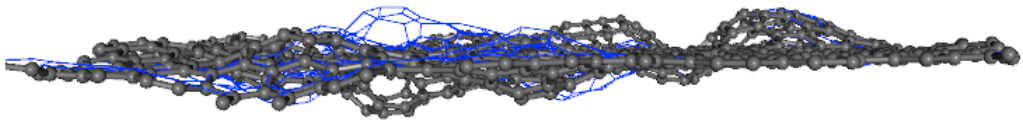

Figure 4.8: The side view of the final configuration with δr = 0.05Å of only moved atoms within pentagons and the original relaxation (distort all atoms). a) The gray balls and sticks show the result of moving atoms within pentagons. b) The blue frames represent the result of original distortion.

and compared with atoms not included in pentagons. Figure 4.8 shows the side view of the final configuration of relaxed 800 a-g system when the δr = 0.01Å and only the atoms within pentagons were randomly moved . These results are similar as the previous test: a) The maximum change in $\overline{\delta r'}$ is around 0.625Å and the maximum change in total energy is around $0.02eV$ per atom. b) No matter which atoms were distorted initially, the final puckered regions involve the same atoms, but possibly puckered in the opposite direction relative to the symmetry plane. Finally, we note that a 128-atom amorphous graphene model made with ”melt quenching” [1] exhibits regions puckered around pentagons in a similar fashion to what we report here.

Different initial symmetry breaking leads to different nearly degenerate states after relaxing. However, as stated above, no matter how different initial condition is (or how different these degenerated state is), the puckered regions are almost the same. It is evident that different rings induce these ripples. With this motivation, we searched for regions where the height differences of two neighbor atoms are the largest and smallest in the model (crinkled and smooth regions), as shown in Figure 4.9, 4.10 and 4.11. In these plots, the gray atoms are the configuration of crinkled system, and the blue straight lines represent the original model.

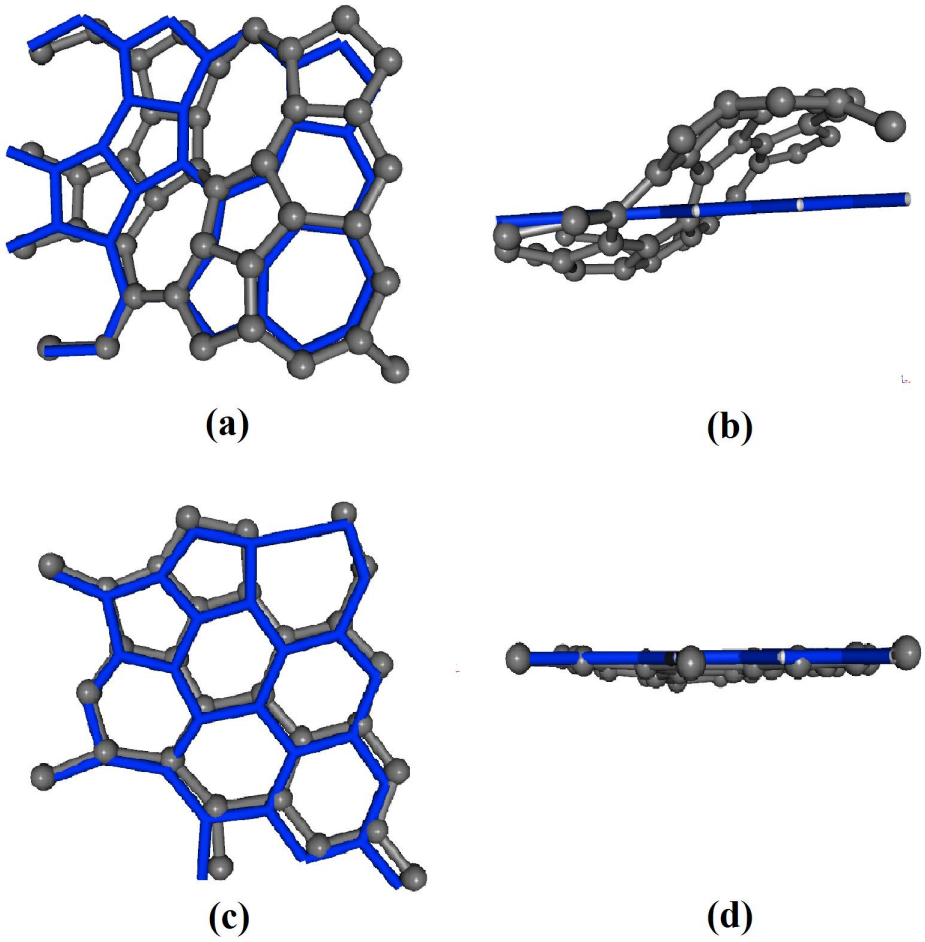

Figure 4.9: The enlarged plot of crinkled and smooth region of 800 a-g model. a) The top view of the crinkled region. b) The side view of the crinkled region. c) The top view of the smooth region. d) The side view of the smooth region.

As illustrated in Figure 4.9 and 4.10, the puckered areas are pentagon-dense areas. The bonds with most distortion do not belong to these pentagons, instead they are within the hexagons or heptagons connecting two pentagons. And the smooth areas have fewer pentagons than the crinkled areas, and most parts of the smooth areas contain hexagons and pentagons. These plots imply that the hexagons and heptagons alone will not lead to planar symmetry breaking. These ripples formed by pentagons strongly remind us of the fullerenes, especially the buckyball (C_{60}) which only contains pentagons and hexagons.

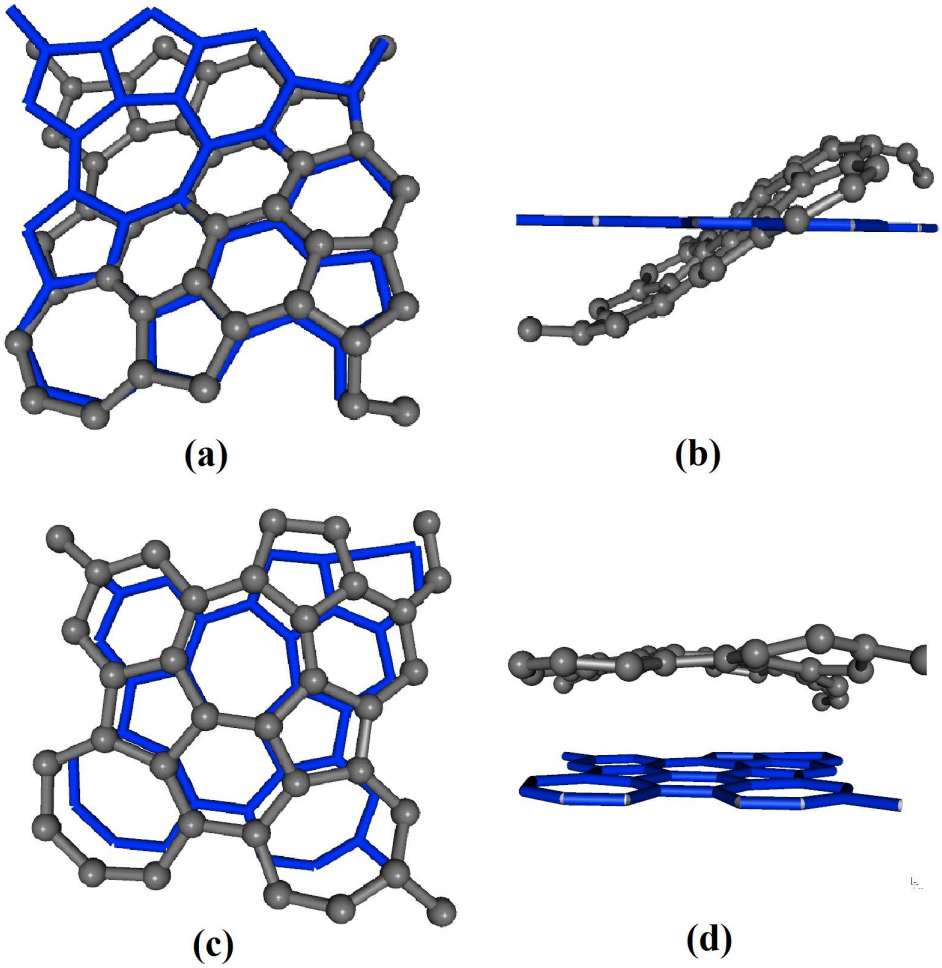

Figure 4.10: The enlarged plot of crinkled and smooth region of 836 a-g1 model. a) The top view of the crinkled region. b) The side view of the crinkled region. c) The top view of the smooth region. d) The side view of the smooth region.

The distance from the top to the bottom of the ripples for 800 a-g is around 5.809Å as shown in Figure 4.5, which is comparable to the diameter of buckyball, 6.636Å. As shown in Figure 4.9, 4.10 and 4.11, the crinkled regions are all associated with pentagons.

In conclusion, while the planar conformation is locally stable, a lower energy solution is obtained that is puckered with local maxima and minima in the vicinity of pentagons. The relaxation is performed using a density functional calculation of the electronic energy. The scale of the puckering is consistent with the curvature found in

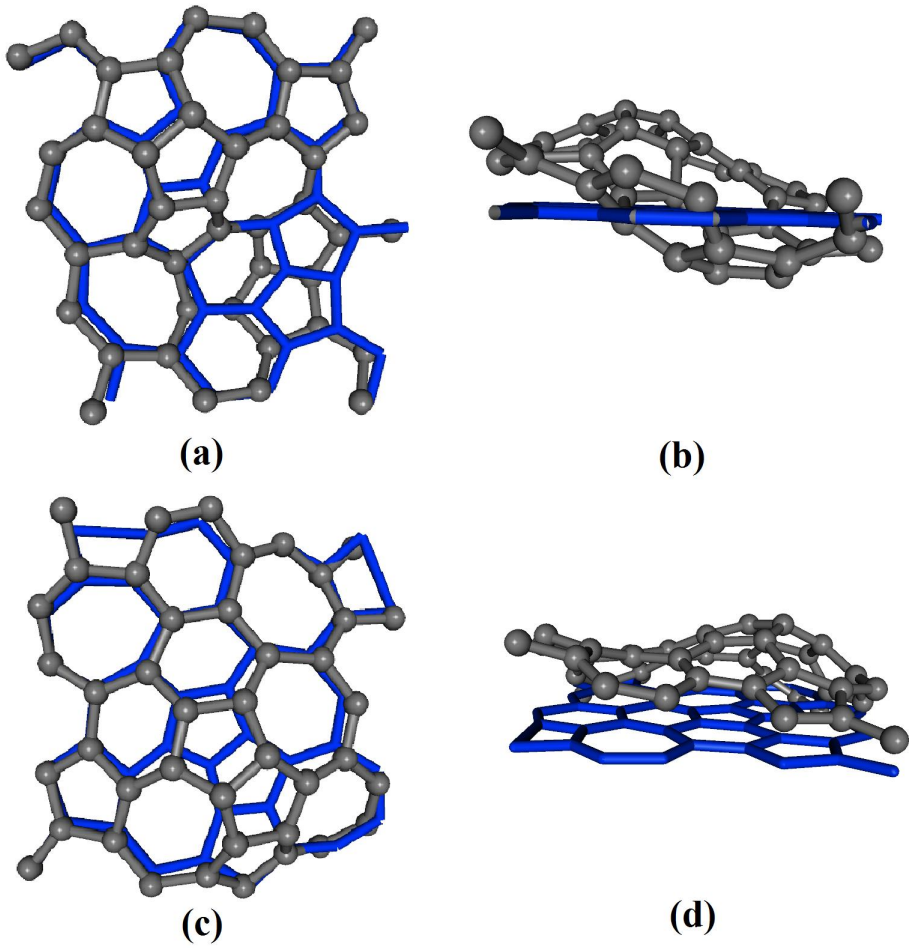

Figure 4.11: The enlarged plot of crinkled and smooth region of 836 a-g2 model. a) The top view of the crinkled region. b) The side view of the crinkled region. c) The top view of the smooth region. d) The side view of the smooth region.

buckyball caps with a pentagon surrounded by larger rings. While we have demonstrated that a well defined puckered state exits, further study is needed to determine whether the puckered state is a single minimum, or rather a series of roughly degenerate local minima with properties akin to the glassy state.

4.4 Potential Energy Landscape of Amorphous Graphene

A key feature of matter in a disordered state is the existence of large numbers of conformations with essentially degenerate energies, which may also be mutually accessible with small energy cost. This is in contrast with crystals, which possess long range order, few polymorphs and typically a deep energy minimum and large energy barrier. The ground state is thus sharply defined, and the only low energy excitations are phonons - transitions to other structures are prohibited. Where realistic models of disordered systems are concerned, few attempts have been made to quantitatively characterize the number, energetics, and proximity (in the sense of barrier) of these states. In his inherent structure formulation of statistical mechanics, Stillinger argued that the number of minima scales like $N!exp(\alpha N)$[77], where N is the number of atoms in the model, and a is a positive system-dependent constant. a was estimated to be around 0.8 in a monatomic liquid[78], and flexible organic molecules exhibit larger α, as in the fragile glass former ortho-terphenyl where a is around 13.14[79]. For temperatures well below the melting point, these local energy minima are denoted inherent structures.

To further motivate this work, consider the following *gedanken* experiment. Consider a sequence of molecules with N atoms. It is well known that asNincreases, the number of minima accessible to the molecule also increase, and such conformations are extensively studied in chemistry[80][81][82][83]. While it is unlikely that a rigorous theory quantifying these minima as a function of N can be formulated, it is clear from computer experiments that the number of minima grow drastically with N. For most molecular systems it is difficult to be certain that the global minimum structure has been found in a simulation as there are so many metastable minima in which the system can be trapped. In this paper, we are concerned with the even more intractable problem of characterizing the minima, or potential energy surface of a disordered condensed matter system in both twodimensional (2D) and three-dimensional (3D) cases. For a 3D crystal, if one

introduces small random distortions and relaxes the disturbed system, it returns to exactly the same structure. This is *not* true for disordered systems. For 3D, we find there exits a continuum of metastable minima for a-Si, in which a number of tiny distortions of bond angles (and to a much lesser extent bond lengths) yield a distinct energydegenerate conformation, which reveals the existence of an extraordinarily flat potential energy landscape (PEL). Fedders and Drabold showed that starting from a well-relaxed α-Si:H model, quenching a set of "snapshots" during a constant-T MD simulation never returns to the exact initial state, instead they fall into minima that are topologically equivalent (*e.g.*, with the same network connectivity), but with small variations in bond angles and bond lengths[84].We find that the behavior in α-Si is consistent with α-Si:H. The case of α-g[76] is different in the following sense. Like α-Si, we find a continuum of essentially energy degenerate states in which minute (but "real") variations in bond angles and bond lengths are displayed. Of course, such states retain identical connectivity since their energies are identical to within a few μeV. However, α-g also exhibits a variety of local energy minima associated with different puckering. These structures usually have similar energies (within $\sim 10meV$), but a significant barrier separating them. Thus, the picture that emerges of the α-g energy landscape is a variety of inherent structures (with varying puckering) with slightly varying energies but substantial barriers between them, and in each of these basins (associated with a particular puckered state) an ambiguously defined minimum with small variations in bond angles and bond lengths accessible as we describe in detail below in Sec. 4.4.3.2. The structure of sp^2 amorphous carbon has been much discussed[85][86][87]. Our networks are quite different because of their strictly 2D nature, though this is not obvious in gross features such as the radial distribution function. Another class of potentially relevant structures are the "schwarzites", 2D negative curvature versions of the graphene materials[65].

Beside the work described above on ultra-low energy excitations, we also discuss other phenomena peculiar to α-g. There has been intensive study in understanding the properties of crystalline graphene, but little is securely understood about amorphous phases. Recent electron bombardment experiments have revealed the existence of amorphous graphene[68] [69]. Clear images of regions of amorphous graphene have been published by Meyer[70]. In previous work, we observed that planar amorphous graphene is extremely sensitive to out-of-plane distortions[57]. Similar behavior has been verified in amorphous graphene by experiment and other calculations[88][89]. We have found that very slightly different initial conditions (*e.g.*, in the transverse coordinates) lead to very different puckering after relaxation[57]. These states exhibit little or no difference in topological properties, *i.e.* ring statistics and coordination number. However, the total energy differences between these metastable states are around 0.02 eV per atom, and the full width of the puckering along the transverse direction (between extrema) is around $6 - 7\mathring{A}$.

A natural complement to these studies is an exploration of low-frequency classical normal modes. These modes turn out to be rather delocalized. As presented for two level systems, the tunneling between two equilibrium states triggers a number of low-energy excitations[90][91]. Details are discussed in Sec. 4.4.3.3. In Sec. 4.4.4, we summarize our findings about the degenerate states and localized imaginary-, low- and high-frequency vibrational modes of amorphous graphene.

4.4.1 Models

To approach this problem computationally, we employ an 800-atom amorphous graphene model (800 α-g) due to He and Thorpe generated by introducing Stone-Wales defects into a perfect honeycomb lattice and a WWW annealing scheme[74]. This model has perfect threefold coordination with varying concentration of 5, 6 and 7 member

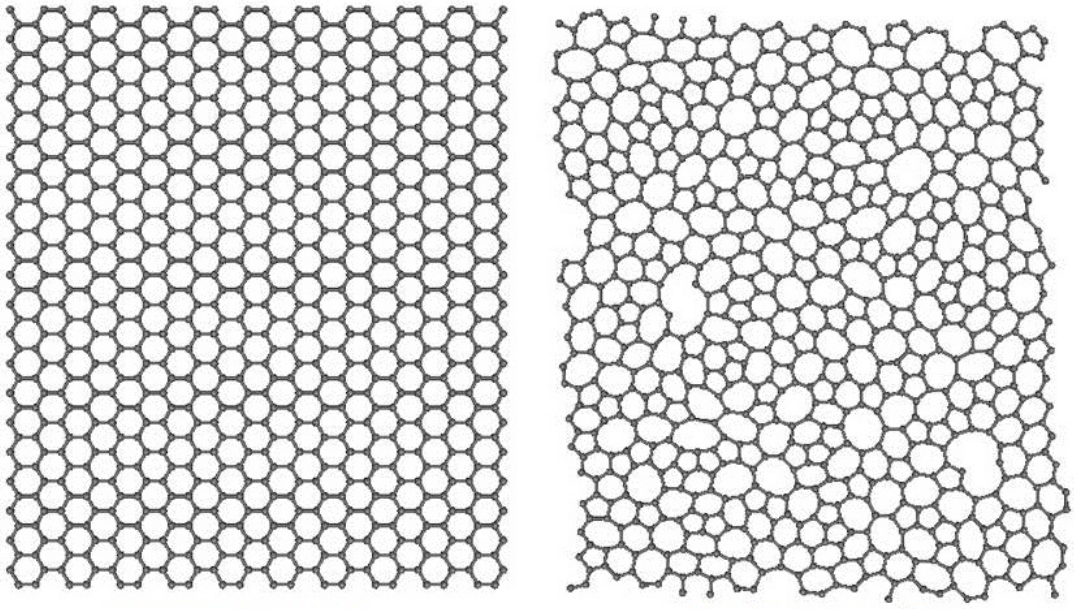

Figure 4.12: Comparison between crystalline and relaxed amorphous phases of graphene. Periodic boundary conditions are employed.

rings[76] and is a practical realization of the continuous random network (CRN) concept proposed by Zachariason[75]. The comparison between crystalline and amorphous graphene is shown in Fig. 4.12. We have relaxed the 800-atom α-g model, and while small rearrangements occurred, planar symmetry was preserved. We found that by very slightly breaking the planar symmetry (by randomly moving each atom by $\sim 0.01\mathring{A}$) and again carrying out the minimization, the resulting structures were always puckered[57].

The amorphous Si model we employ is a realistic 64-atom model (64 α-Si), generated by Barkema and Mousseau using a modified form of WWW algorithm[22]. This model has perfect fourfold coordination and within the limitations of its small size, to our knowledge is not in significant contradiction to any experiment.

4.4.2 Procedure

Our calculations are performed with an *ab-initio* program SIESTA[8], using pseudopotentials and the Perdew-Zunger parameterization of the local-density approximation (LDA) with a single-ζ basis and Harris-Functional at a constant volume. Earlier simulations are described in Refs. [92] and [93]. To investigate the nature of minima on the potential energy surface, we employ a method proposed by Fedders and Drabold[84] similar to the conformational space annealing approach mentioned in [94], which has been used in locating and predicting low-energy conformations of various proteins[95][96][97][98]. First, starting with a perfectly relaxed model (in our case 800 α-g and 64 α-Si), we run a sequence of four parallel simulations. We let the network evolve for $8.0ps$ at four different mean temperatures of 20K, 500K, 600K or 900K. The target temperatures are achieved by velocity rescaling (a "Berendsen thermostat"). From these simulations, we relax these to find the metastable minimum (or inherent structure) associated with the initial snapshots.

To investigate the structural changes between these minima (quenched configurations from snapshots), we use two autocorrelation functions as defined by Fedders and Drabold[84]:

$$\Delta\theta(t_1, t_2) = \sum_i ((\theta_i(t_1) - \theta_i(t_2))^2/N)^{\frac{1}{2}} \tag{4.1}$$

and

$$\Delta r(t_1, t_2) = \sum_i ((r_i(t_1) - r_i(t_2))^2/N)^{\frac{1}{2}} \tag{4.2}$$

In Eq. 4.1 the index i runs through all the bond angles where θ_i is the i^{th} bond angle. In Eq. 4.2 the index i runs over all nearest-neighbor pairs where r_i is the i^{th} distance between a pair. The times t_1 and t_2 refer to the quenched snapshots. These autocorrelation functions provide a close view of how thermal MD simulations induce transitions between different energy basins.

4.4.3 Discussion

We break the discussion into three parts. First, the nature of pentagonal puckering, next, low-energy conformation fluctuations and finally an analysis of the classical vibrational modes.

4.4.3.1 Symmetry Breaking

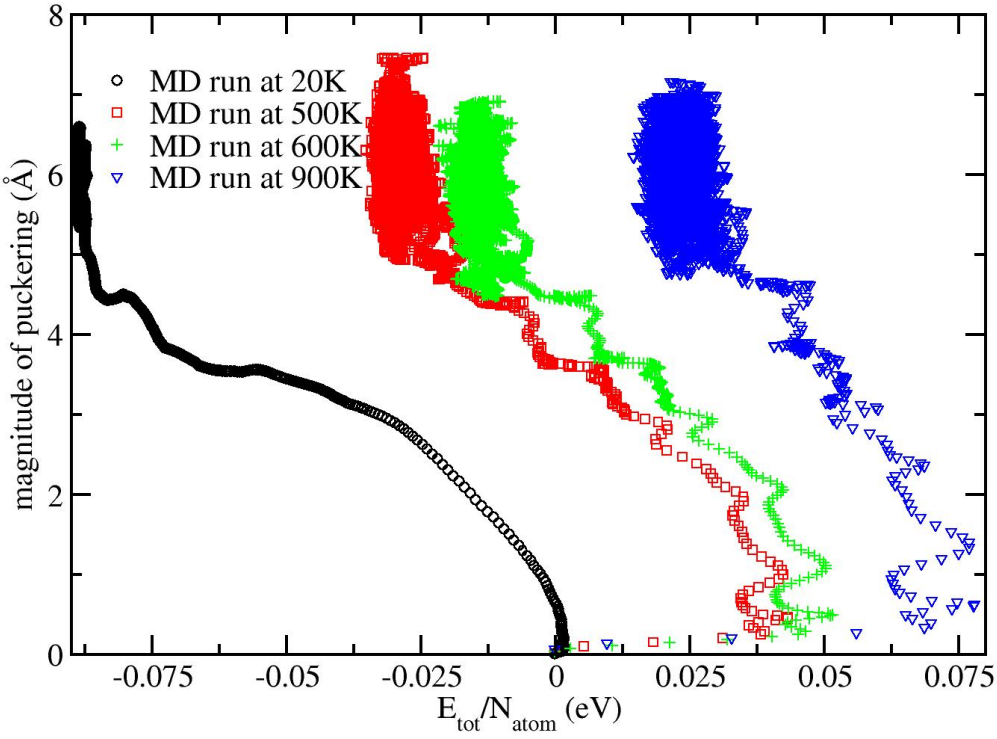

Figure 4.13: Correlation between the total energy per atom and magnitude of puckering for constant temperature MD simulations. The zero total energy refers to the total energy of original flat 800 α-g model.

As conjectured by Cataldo and co-workers using purely topological analysis, fullerene-like structure may be expected in these films[99]. As we have shown in [57], the original flat 800-atom α-g model is exceedingly sensitive to transverse distortion, and then loses planar symmetry lowering the total energy of the supercell. In every case, even at $T = 20K$, the planar symmetry breaks and the system puckers: thermal disorder is sufficient to induce puckering. Fig. 4.13 shows the relation between the total energy of the system and maximum separation of atoms along the normal direction (magnitude of puckering) in constant-T MD simulations at the indicated temperatures. In the language of PEL, starting from the flat 800 α-g, four MD simulations overcome tiny energy barriers and take a down-hill path to regions with lower energy. Thus the flat 800 α-g model can be considered as an exceptionally shallow basin on the PEL. The barrier between flat and puckered is a few μeV for this Hamiltonian.

4.4.3.2 Conformational Fluctuations

The quenching procedures at sequential timesteps yield basins on the PEL. Here we show the calculations at average temperatures of 500K, 600K and 900K. These results of MD runs at different temperatures exhibit consistency with each other. Fig. 4.14 shows how these two autocorrelation functions vary with time. Since temperatures of all the MD simulations achieve equilibrium after 6.0 ps, here the autocorrelation functions are calculated with $t_1 = 6.0ps$. It appears $\Delta\theta(t_1, t_2)$ and $\Delta r(t_1, t_2)$ from three MD runs at different temperatures are qualitatively similar. They increase linearly and eventually fluctuate about a constant. The continuity of the curves in Fig. 4.14 suggests that there is a continuum of states, accessible albeit structurally varying only in very modest ways.

The total energy distributions of all the quenched supercells from MD runs at different temperatures are shown in Fig. 4.15. For temperatures other than 20K, the total energy distributions exhibit several peaks. The minor peaks in Fig. 4.15 correspond with

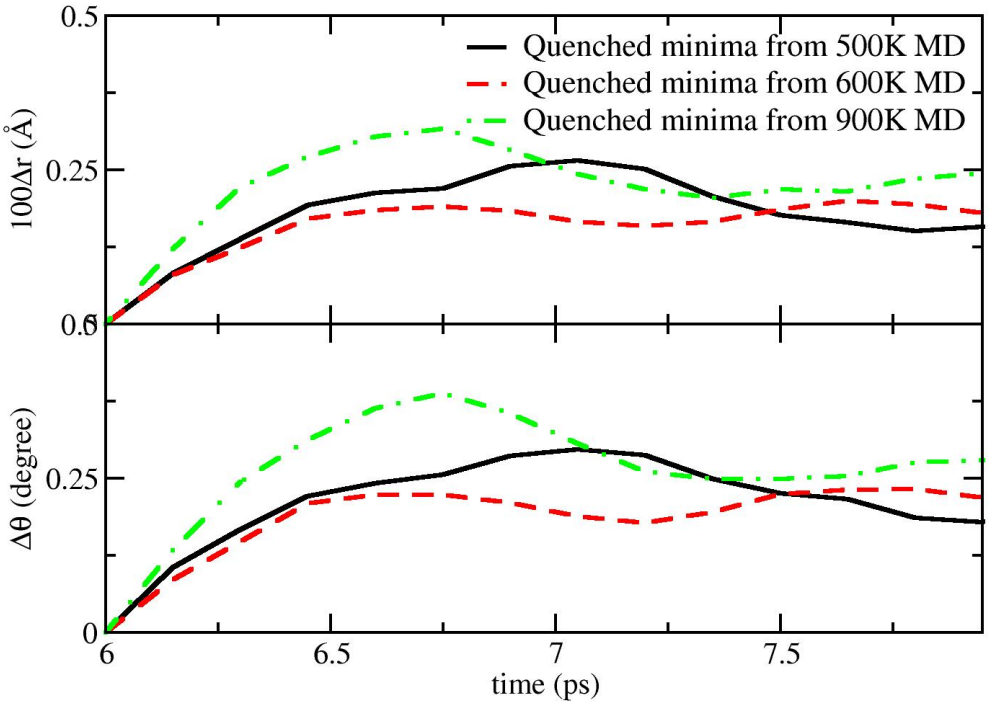

Figure 4.14: Time variation of two autocorrelation functions. This figure shows autocorrelation functions of $\Delta\theta(t_1, t_2)$ and $100\Delta r(t_1, t_2)$ for $t_1 = 6.0ps$ and t_2 varying from 6.0 to $7.95ps$. The temperatures are 500K, 600K and 900K. The functions appear to be continuous.

Table 4.5: Average value and standard deviation of E_{tot}/N_{atom}, $\Delta r(t_1, t_2)$ and $\Delta\theta(t_1, t_2)$ of quenched configurations from MD runs in the time period from 3.6 to 8.0 ps, where $t_1 = 1.05ps$.

T(K)	$\overline{E_{tot}/N_{atom}}$ (eV)	$\sigma_{E_{tot}/N_{atom}}$ (eV)	$\overline{\Delta r(1,t_2)}$ (Å)	$\sigma_{\Delta r}$ (Å)	$\overline{\Delta\theta(1,t_2)}$ (○)	$\sigma_{\Delta\theta}$ (○)
500K	-9.595×10^{-2}	8.855×10^{-5}	$4.907 \times 10{-}2$	2.551×10^{-4}	3.736	1.814×10^{-2}
600K	-9.435×10^{-2}	9.917×10^{-5}	7.503×10^{-2}	1.973×10^{-4}	4.181	6.464×10^{-2}
900K	-9.716×10^{-2}	2.091×10^{-4}	2.516×10^{-2}	8.08×10^{-3}	1.725	0.146

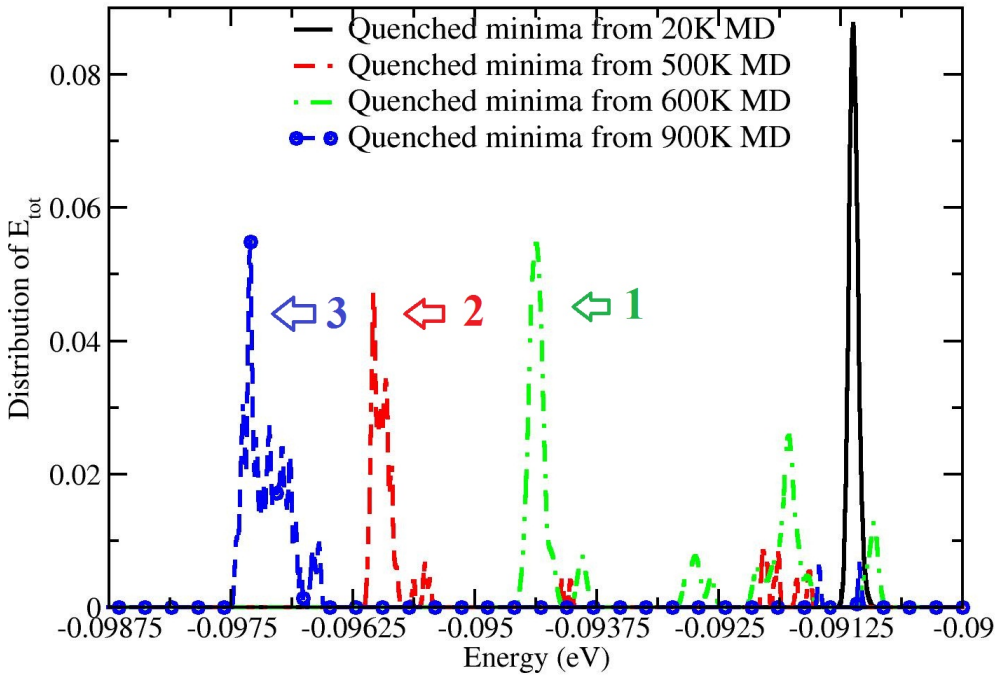

Figure 4.15: Color. Total energy distribution functions of quenched supercells from MD runs under 20K, 500K, 600K and 900K. The total energy of original flat 800 a-g is considered as $0eV$. Distinct structures correspond to different puckered states, broadening within each major peak from conformational variations. Three major peaks from MD runs at 600K, 500K and 900K are labeled as 1, 2 and 3 respectively.

the annealing process of MD runs. The major peaks (labeled 3, 2 and 1 in Fig. 4.15) are derived from different puckering configurations sampled in the process of equilibration to constant T. Correspondingly as shown in Fig. 4.14, the fluctuations of autocorrelation functions (after thermal equilibrium is reached) reach an asymptotic state after of roder $7.0ps$ ($1ps$ from the initial equilibrated state). Each of the three peaks in Fig. 4.15 demonstrates a basin on the PEL of α-G. These nearly degenerate quenched equilibrium states are trapped in distinct basins on the PEL, and quenched minima within one basin form a continuum metastable state around inherent structures. Details of variations in

bond angles, bond lengths and total energies of these metastable states are shown in Table 4.5. The total energy variation between the basins corresponding to the major three peaks are averaged as $1.405 \times 10^{-3} eV$, which is one order of magnitude higher than the energy of fluctuations within a basin. In spite of their different energy scales, these quenched configurations belonged to distinct basins share identical local bonding. The only difference is that they pucker in distinct ways, as shown in Fig. 4.16.

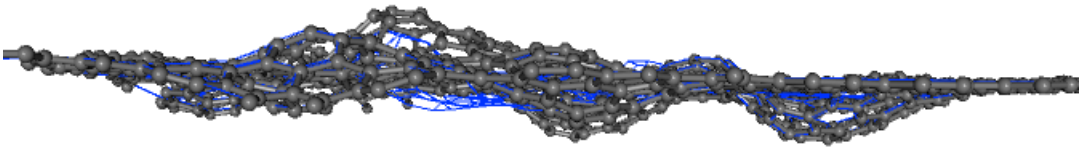

Figure 4.16: Side view of two quenched configurations. Gray balls and sticks show the configuration from 900K MD, and blue lines represent the one from 500K.

For comparison, we repeat parallel calculations using 64 α-Si model quenched from MD runs at 20, 300 and 500K. The autocorrelation functions are shown in Fig. 4.17. The results are in agreement with Fedders and Drabold[84]. We see for α-Si systems, there exists one general basin on the PEL (for a particular network connectivity), and the paths lowering the total energy on the PEL will eventually go into this basin, leading to inherent structures with minor changes in bond angles and lengths, and tiny energy scale.

Comparison between results of α-g and α-Si suggests that PEL of 3D system (α-Si) is smooth and inherent structures are contained in one general basin. α-g is similar within one puckered state.

For α-g, an MD run at higher temperature (annealing) can overcome the energy barrier and hop to a basin associated with a different puckered state. Also by investigating the correlation between topology and energy scale of these quenched supercells, it is

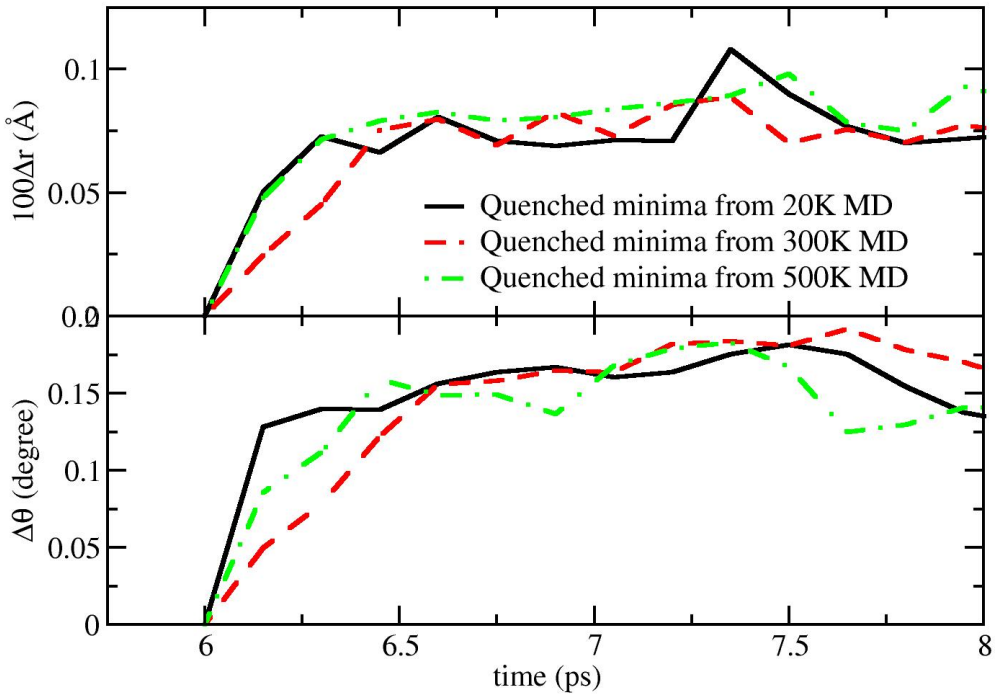

Figure 4.17: Time variation of two autocorrelation functions for α-Si. This figure shows autocorrelation functions of $\Delta\theta(t_1, t_2)$ and $100\Delta r(t_1, t_2)$ for $t_1 = 6.0ps$ and t_2 varying from 6.0 to 8.0 ps. The temperatures are 20K, 300K and 500K. The results are similar to [84].

revealed that lower total energy (stabler state) is associated with small variation in bond lengths and angles from the original flat 800-atom model.

4.4.3.3 Classical Normal Modes

To investigate the vibrational modes in these supercells, we perform calculations of dynamical matrix, its eigenvalues and eigenvectors, for the original flat 800 α-g model, and two quenched configurations with certain region puckering along opposite direction, designated "pucker-up" and "pucker-down" models, as shown in Fig. 4.18. The dynamical matrix was constructed from finite difference calculations (using six orthogonal

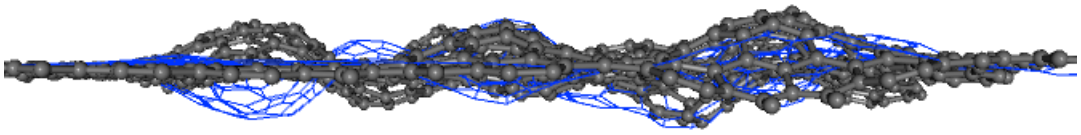

Figure 4.18: Color. Side view of pucker-up and -down 800 a-g models. Gray balls and sticks illustrate pucker-up model, and pucker-down supercell is represented by blue lines.

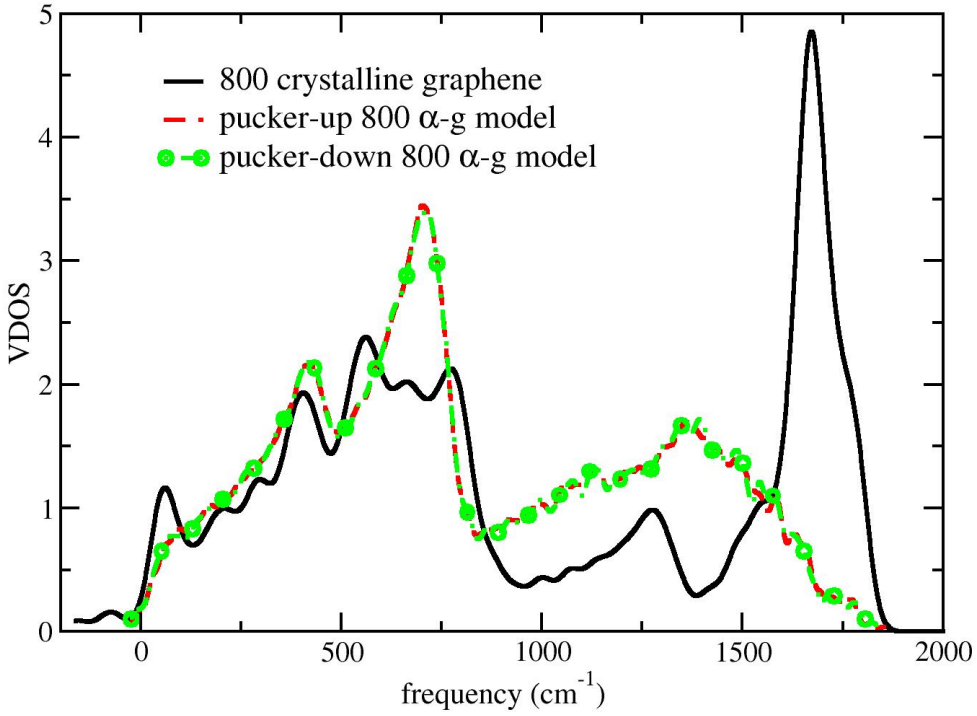

Figure 4.19: Color. Vibrational density of states (VDOS) of 800 crystalline graphene, pucker-up and -down α-g models. Note the distractive feature at $\omega \cong 1375 cm^{-1}$ for α-G.

displacement of 0.04 Bohr for each atom). We also perform the phonon calculation for an 800-atom crystalline graphene model (for related calculations on very large fullerenes, see

Ref. [33]). The vibrational density of states (VDOS) of 800 crystalline model, pucker-up and -down 800 α-g models are shown in Fig. 4.19. The VDOS result of crystalline graphene shows good agreement with a published calculation[100]. In Fig. 4.19 at a frequency near 1375 cm^{-1}, the spectrum of crystalline graphene has a minimum. In contrast the spectrum of two puckered supercells achieve a local maximum. Thus Raman scattering experiments are expected to provide a way to distinguish crystalline and amorphous graphene. There is no difference in the spectrum between pucker-up and -down 800 α-g models. In a mixed sample containing 3D amorphous carbon, this discernible difference from ordered graphene near 1375 cm^{-1} is probably unhelpful because of the many modes seen in various phases of α-C (with varying sp^2/sp^3 ratio) near the relevant energy[101][102][103].

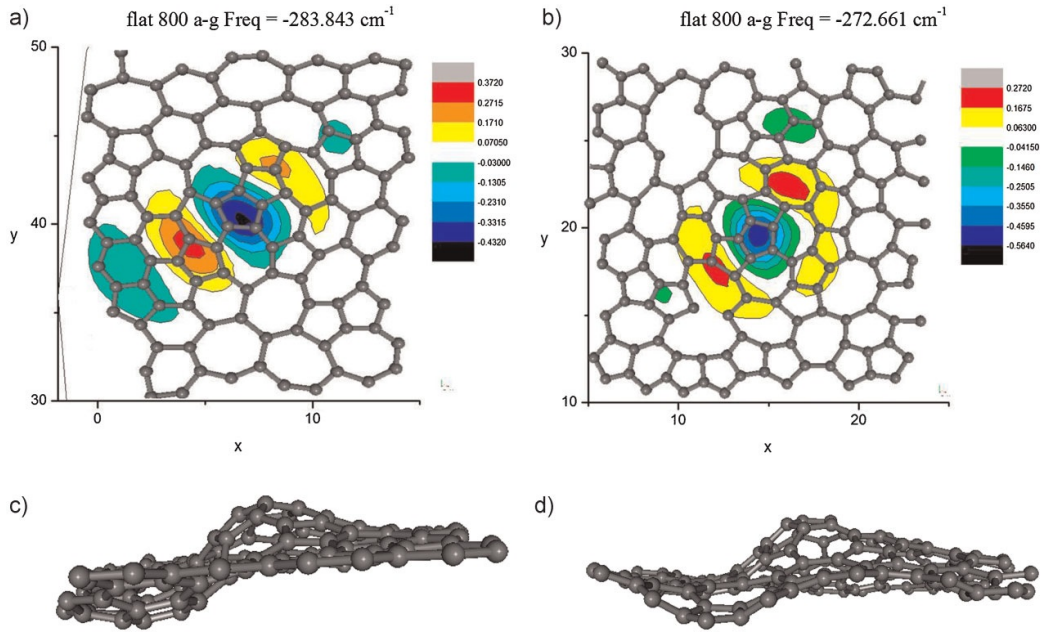

Figure 4.20: Color. Two examples of imaginary-frequency modes in flat 800 α-g model. The contour plot represents the component of eigenvector along the direction transverse to the plane.

In the original flat 800-atom α-g model, the eigenvectors with imaginary eigenvalues have large components along the normal direction of the graphene plane (at least four orders of magnitude higher than the longitudinal components). These imaginary-frequency modes are localized on pentagons in the network: two example are shown in Fig. 4.20. As shown in Fig. 4.20 (c) and (d), these imaginary-frequency modes are localized near structures that lead to puckering. As shown in [57], it is pentagons that lead to puckering and symmetry breaking. Thus these imaginary-frequency modes are an indicator of the instability of the flat 800 α-g model.

In the puckered models, we observe modes with a low frequency, around 14-20 cm^{-1}, reminiscent of "floppy modes" proposed by Phillips and Thorpe[104][105]. The structures of these low-frequency modes are quite complex, as shown in Fig. 4.21. These modes are rather extended, and have significant weight on pentagonal puckered regions and large rings, analogous to what Fedders and Drabold have seen in α-Si:H[84]. The observed energy scale of these low-frequency modes is around a few meV, almost half of the lowest frequency of the acoustic phonon modes in a crystalline graphene with same size. As proposed in the theory of "two-level systems", there exists a distribution of low-energy excitations, caused by tunneling of atoms between nearly degenerate equilibrium states[90][91]. Goldstein pointed out that the dynamics could be separated into two categories: vibrational motion about a minimum on PEL and transitions between minima[106]. Then these low-frequency modes might be triggered by transitions between degenerate minima within one basin on the PEL. As shown in Section 4.4.3.2, the energy variations between minima within one basin is in the order of $10^{-4}eV$, and the energy difference between basins is in the order of $10^{-3}eV$. The energy scales of these low-frequency modes ($\sim meV$) are sufficient to drive conformational fluctuations, but not high enough to overcome the energy barrier between different basins (quenched states) on the PEL.

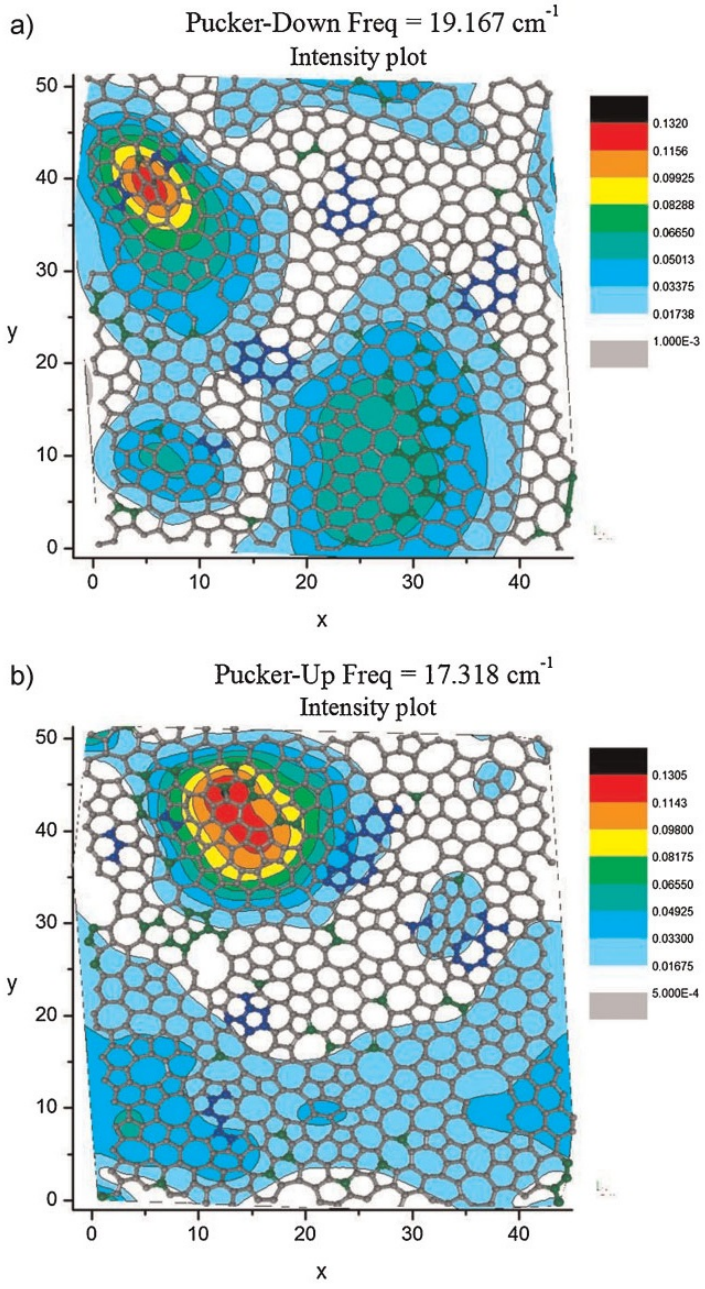

Figure 4.21: Color. Examples of low-frequency modes in pucker-down and -up 800 α-g models. The contour plots represent the intensity of eigenvectors on each atom. The blue atoms illustrate the "puckering-most" atoms, and the green atoms represent "flat" atoms.

In the high-frequency domain, there also exist highly localized high-frequency modes in the puckered configurations. These modes are triggered by the pentagonal defects and

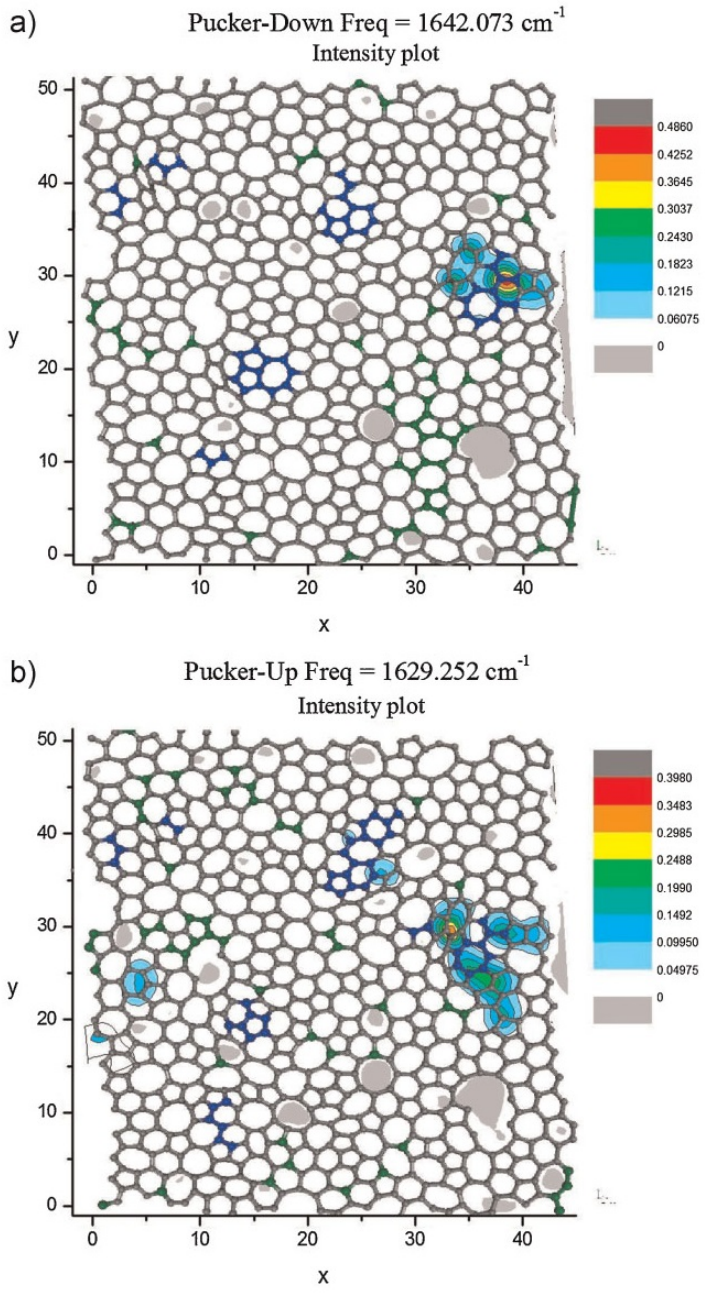

Figure 4.22: Color. Examples of localized high-frequency modes in pucker-down and -up 800 α-g models. The contour plots represent the intensity of eigenvectors on each atom. The blue atoms illustrate the "puckering-most" atoms, and the green atoms represent "flat" atoms.

are highly localized, as shown in Fig. 4.22. This result is consistent with Biswas et al. [107] and Fedders et al. [108], who have shown strain and topological defects are active at highest frequencies.

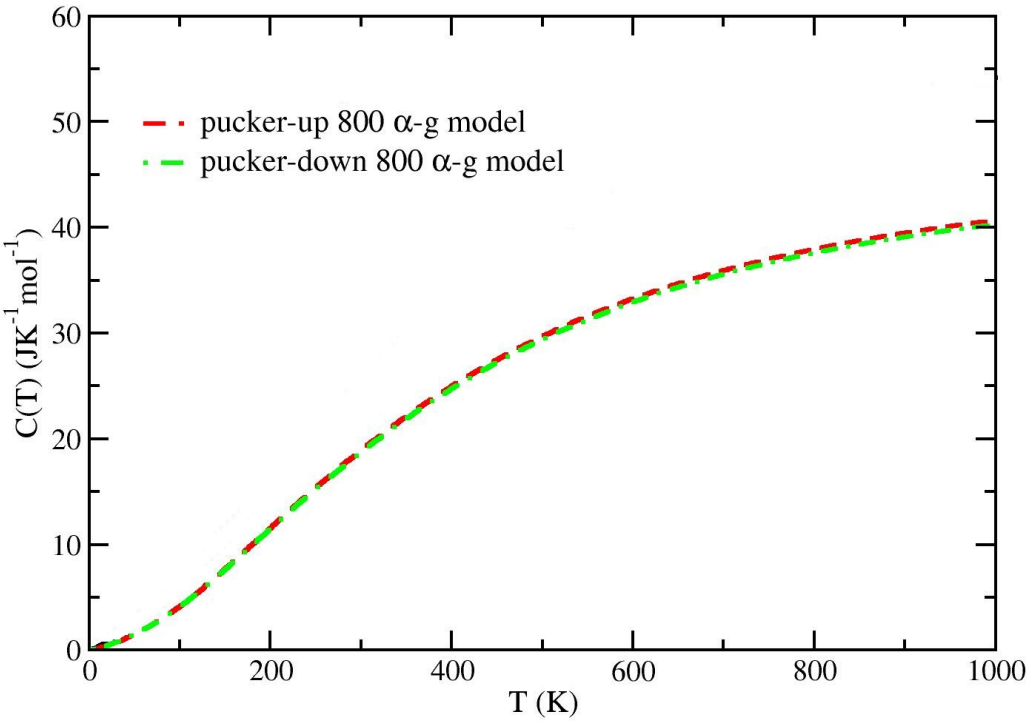

Figure 4.23: Color. Temperature dependence of C(T) of pucker-up and -down 800 α-g models.

We also compute the specific heat $C(T)$ using VDOS information[109]:

$$C(T) = 3R \int_0^{E_{max}} (\frac{E}{k_B T})^2 \frac{e^{E/k_B T}}{(e^{E/k_B T} - 1)^2} g(E) dE \tag{4.3}$$

where g(E) is normalized VDOS. For room temperature (300K), specific heat of flat, pucker-up and -down 800 α-g models are 25.151, 18.879 and 18.702$JK^{-1}mol^{-1}$ respectively. The temperature dependence of C(T) is shown in Fig. 4.23. This is

presumably an academic result as it is currently hard to imagine an experiment for $C(T)$ for this 2D system.

4.4.4 Conclusion

In conclusion, we have found that α-g has a rich and interesting energy landscape. We observe distinct energy scale of basins ($\sim 10meV$) associated with different puckered configurations and then within such a configuration, an ambiguous energy minimum with a continuum of bond angles and bond lengths with energy scale ($\sim$ fewμeV) and a nearly flat PEL. Within a given puckered configuration, this continuum is much like what was seen for α-Si:H in 1996[84].

Vibrational calculations reveal the existence of localized imaginary-frequency modes in flat 800 α-g model. These modes are localized on pentagons and play the key role in losing planar symmetry and forming pentagonal puckering structures. We find delocalized low-frequency phonon modes, similar to floppy modes, which have substantial weight on defects and share the same energy scale as the energy difference between adjacent basins on the PEL. Thus these low-frequency modes are triggered by the transition between adjacent energy minima. Some high-frequency modes are detected and highly localized on puckered regions and large rings.

4.5 Electronic Signatures of Topological Disorder in Amorphous Graphene

4.5.1 Introduction

Spatially localized electronic states occur uniquely in solid state systems with disorder. Since the time of Anderson[19] in the 1950s, it was shown that in the presence of sufficient disorder, certain electron states decay exponentially in space. The study of localization has become one of the most important aspects of condensed matter theory. Localization in three dimensional systems has been well studied[32][110][23][111]. The

celebrated ”Gang of Four” paper discusses localization from scaling theory, and compares one, two and three dimensions[112]. For the two dimensional case, it has been shown theoretically and experimentally that localization can be introduced by defects, as seen in the three dimensional systems[113][114]. In this paper, we'll show that in amorphous graphene, the localized eigenstates emerge from odd-membered ring defects in an otherwise ideal sp^2 system, and we characterize this localization with a realistic Hamiltonian.

Previous calculations reveal that the planar symmetry of amorphous graphene could be easily broken, due to the existence of odd-membered rings[57]. Here we'll show a few electronic states well above the Fermi level could be strongly coupled with several high-frequency phonon modes, which are also highly localized at odd-membered rings. This observation is perhaps reminiscent the polaron study in thin films of liquid He, where Jackson and Platzman showed the motion of a single electron in the plane is highly coupled with the thermally excited ripples in two-dimensional surface[115].

4.5.2 Model

To evaluate the charge density and spatial localization, a 200-atom amorphous graphene model (200 a-g), prepared by a Wooten-Weaire-Winer (WWW) annealing scheme[74], is employed. This model has ideal three-fold coordination, and ring statistics are given in Table 4.6. This 200 a-g model is a realization of CRN concept proposed by Zachariasen[75]. A 288-atom crystalline graphene model (288 c-g) was also used to compare the results with amorphous graphene models.

Table 4.6: Ring statistics of 200 a-g model, shown as %.

Ring Size	5	6	7
Percentage	38.5	53.9	7.7

4.5.3 Charge Density

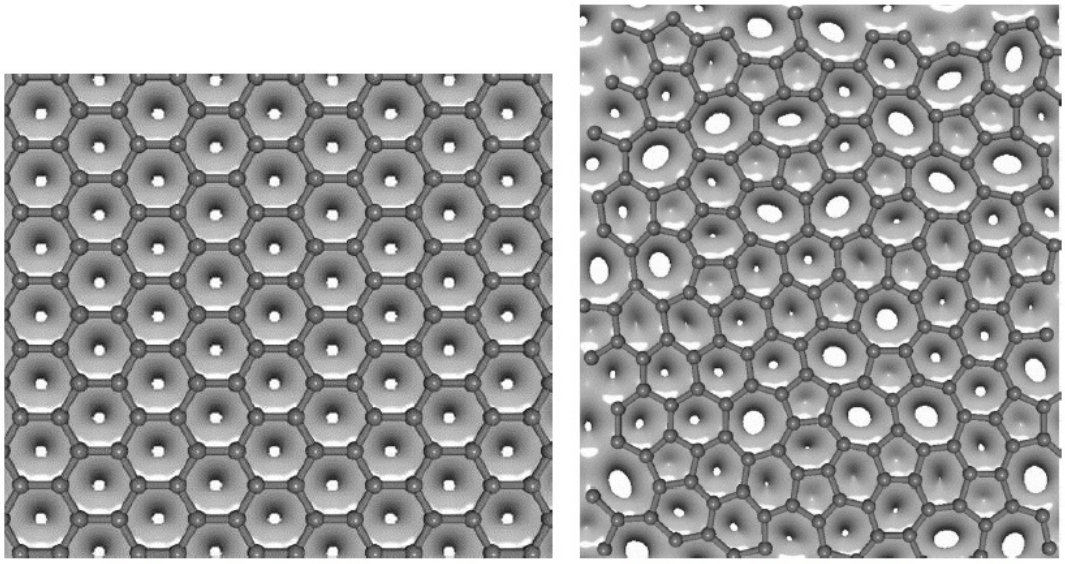

(a) Charge density of 288 c-g model (b) Charge density of 200 a-g model

Figure 4.24: Simulated STM images (total charge density) for both crystalline and amorphous graphene models. The atom configurations are represented by grey balls and sticks.

To study amorphous graphene, we employ an *ab initio* program SIESTA[8], using pseudopotentials and the Perdew-Zunger parameterization of local-density approximation (LDA). In both crystalline and amorphous cases, the minimal basis set (single-ζ basis) and self-consistency were applied. The simulated STM images according to charge density calculation results are shown in Fig. 4.24. For crystalline graphene, the electrons in p orbitals are delocalized on the graphene sheet giving rise to aromaticity. Then the charges are expected to distribute uniformly on the honeycomb lattice of graphene, as shown in Fig. 4.24(a). By contrast, the existence of odd-membered rings disturbs this uniformity, introducing several holes associated with seven-membered rings, and charge is notably localized at five-membered rings. These calculations are in close agreement with

published DFT calculation results of pure crystalline graphene[116] and crystalline graphene with defects[117].

4.5.4 Density of States

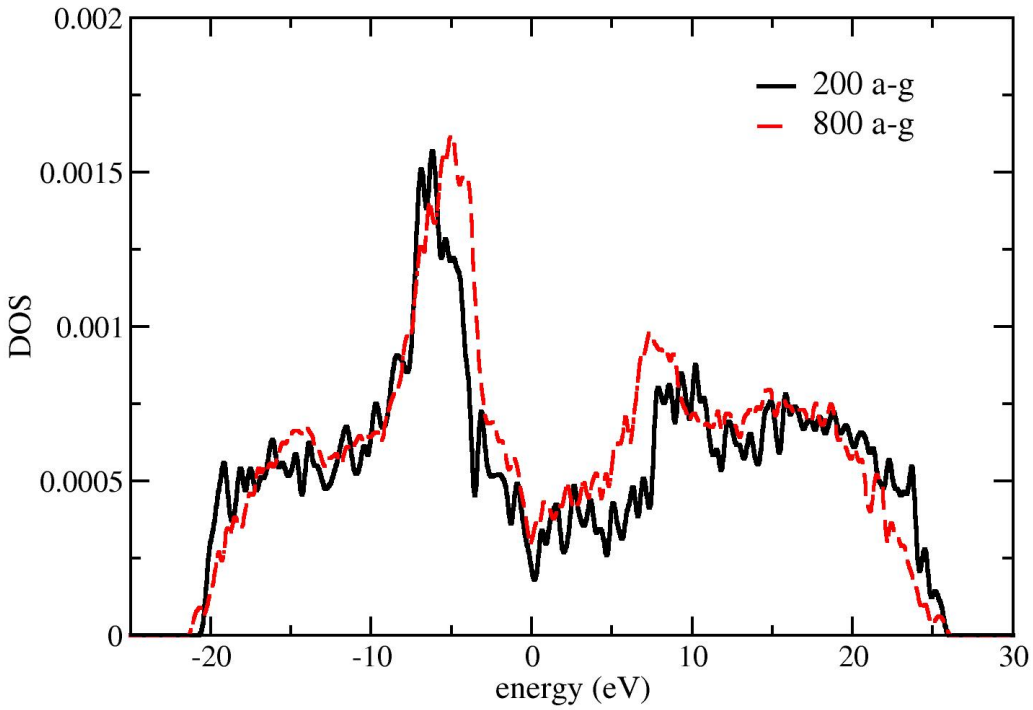

Figure 4.25: DOS of 200-atom a-g and 800-atom a-g models[57]. The solid line represents DOS of 200 a-g, and DOS of 800 a-g is given by dashed line. Fermi level is at 0 eV.

The Γ-point density of states (DOS) of planar 200 a-g model was calculated using the same computational approach as charge density. As we shown in Ref. [57], in an 800-atom amorphous graphene model, the odd-membered rings generate a number of states around the Fermi level. The DOS of 200 a-g model are quantitatively the same as the one of 800 a-g model, as shown in Fig. 4.25.

4.5.5 Localized States

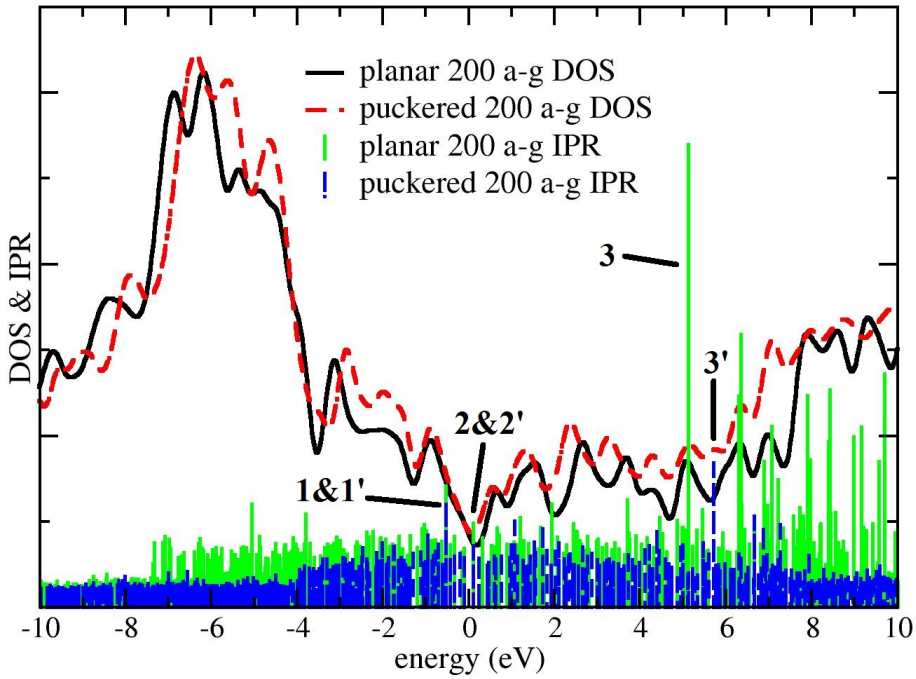

Figure 4.26: Scaled DOS and IPR of planar and puckered 200 a-g models. Fermi level is at 0 eV.

As we previously pointed out, the planar symmetry of amorphous graphene is unstable with respect to tiny external out-of-plane distortions, giving rise to pentagonal puckering and lowering the total energy[57][118]. In the following, localization properties of eigenstates for both planar and puckered models are explored. To characterize the spatial localization of electronic states, inverse participation ratio (IPR) calculations were performed. The IPR is defined as: $I(\psi_j) = N \sum_{i=1}^{N} a_i^{j4} / (\sum_{i=1}^{N} a_i^{j2})^2$, where $\psi_j = \sum_{i=1}^{N} a_i^j \phi_i$ is the j^{th} eigenvector. The results are depicted in Fig. 4.26. Around the Fermi level (0 eV), there are two localized states in planar 200 a-g model, marked as peak 1 and 2 in Fig.

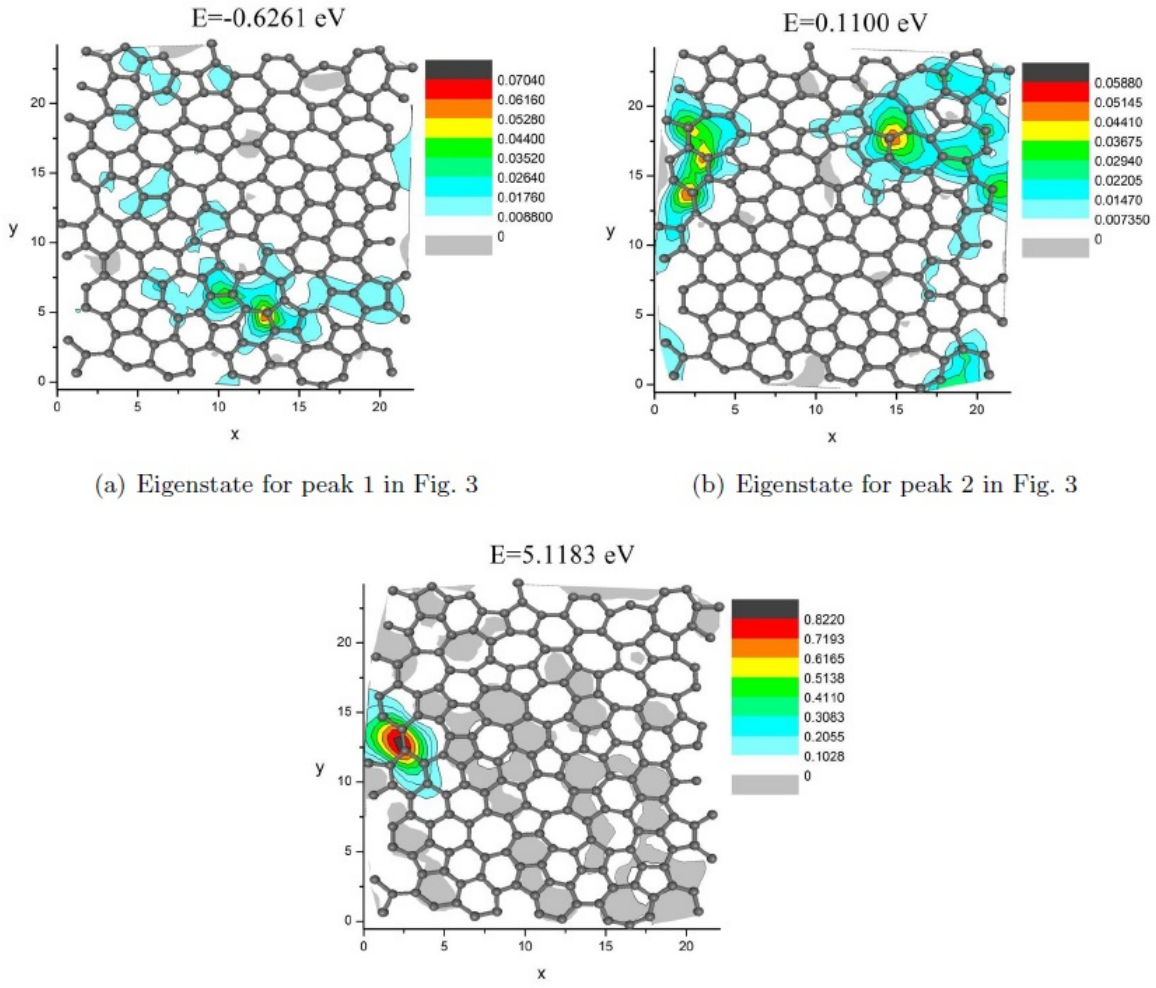

(a) Eigenstate for peak 1 in Fig. 3

(b) Eigenstate for peak 2 in Fig. 3

(c) Eigenstate for peak 3 in Fig. 3

Figure 4.27: Three localized eigenstates of planar 200 a-g model, depicted as peak 1-3 in Fig. 4.26. Here $E_f = 0$ eV.

4.26, and the most localized state is found around 5 eV, marked as peak 3. Correspondingly, the eigenstates are named state 1, state 2, and state 3. Similar calculations have also been performed for a puckered 200 a-g model. Similarly, the IPR calculation shows two localized eigenstates around Fermi level (0 eV), marked as peak 1' and 2' in Fig. 4.26. And the most localized peak is also found around 5 eV, marked as peak 3' in Fig. 4.26. These peaks are named as state 1', state 2' and state 3' respectively.

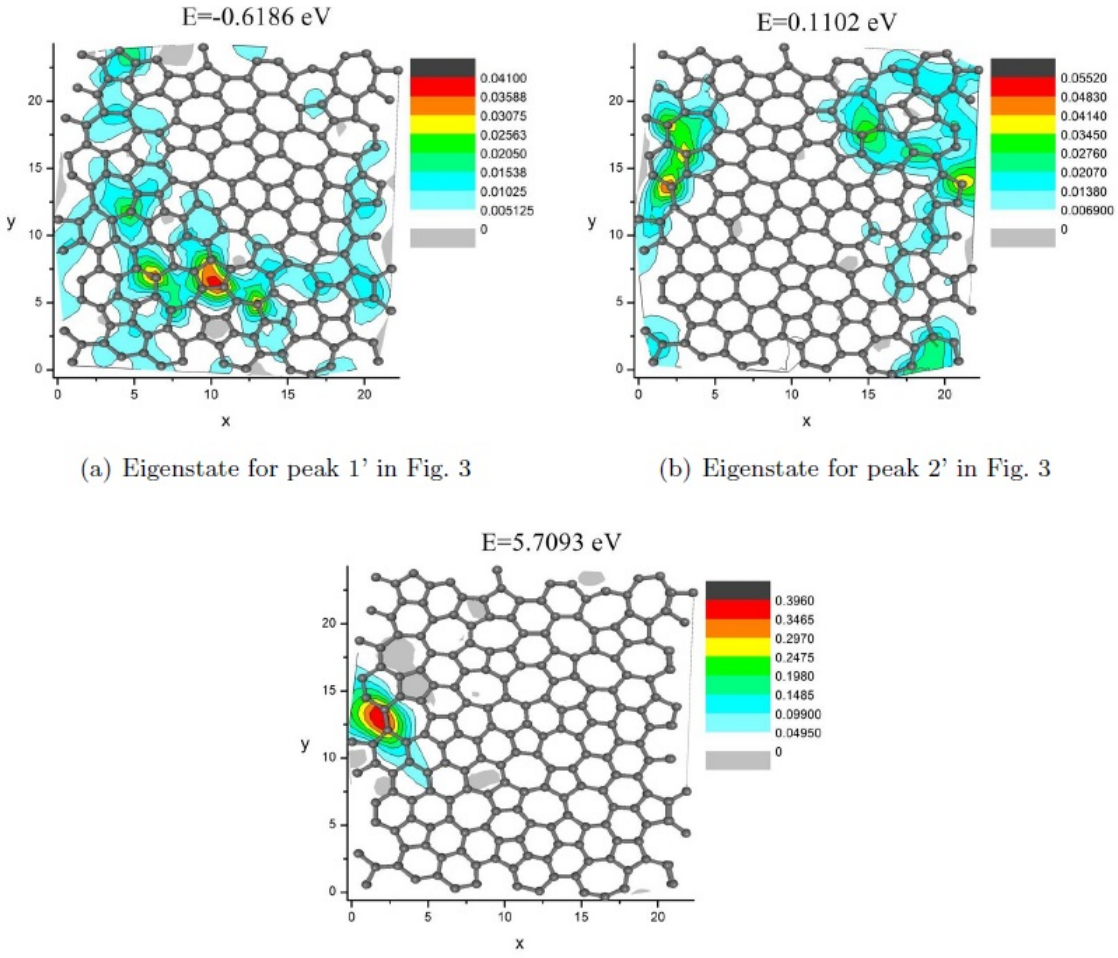

(a) Eigenstate for peak 1' in Fig. 3

(b) Eigenstate for peak 2' in Fig. 3

(c) Eigenstate for peak 3' in Fig. 3

Figure 4.28: Three localized eigenstates of puckered 200 a-g model, depicted as peak 1'-3' in Fig. 4.26. $E_f = 0$ eV.

To visualize the spatial structure of these localized states, the charge density of each conjugate eigenstate is plotted, as shown in Fig. 4.27 and Fig. 4.28. For the planar 200 a-g model, peak 1 is found around the valence tail, and localized around an area with a higher percentage of pentagons, as shown in Fig. 4.27(a). In contrast, for the conduction edge, peak 2 is distributed around an area with higher percentage of heptagons, as shown in Fig. 4.27(b). For the puckered 200 a-g model, the energy levels of peak 1' and 2' are close to

peak 1 and 2. As shown in Fig. 4.28(a), at valence edge, state 1' and state 1 are distributed over an similar high-pentagon-ratio area. And at the conduction edge, state 2' is localized around an area with high heptagon-ratio, as shown in Fig, 4.28(b), analogous to state 2. Thus the presence of odd-membered rings in amorphous graphene gives rise to various eigenstates around the Fermi level, leading to vast difference in DOS between crystalline and amorphous graphene[76][57].

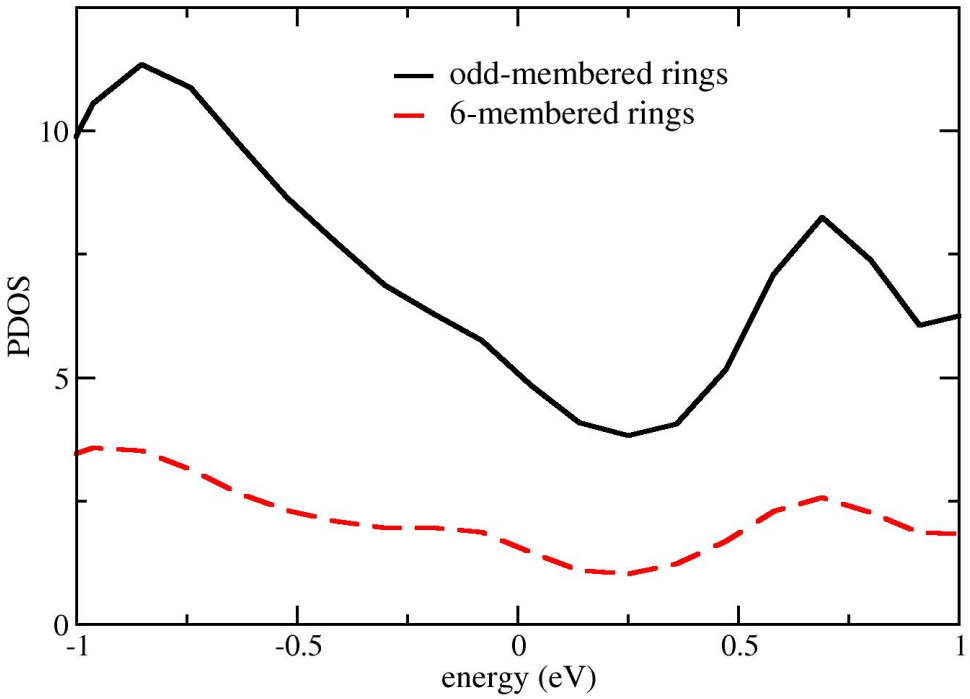

Figure 4.29: PDOS of planar 200 a-g model. Fermi level is at 0 eV.

Next, we explored the electronic consequences of puckering, induced by pentagonal structures. We employ the projected density of states (PDOS) computed for both planar and puckered 200 a-g models, using SIESTA with SZ basis, as shown in Fig. 4.29 and Fig.

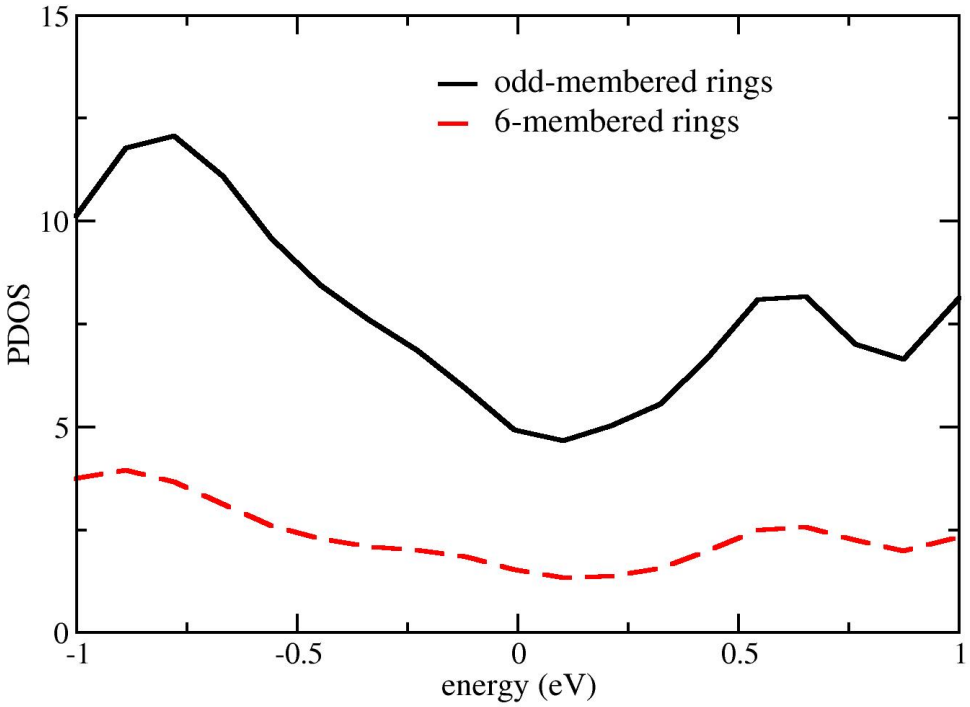

Figure 4.30: PDOS of puckered (relaxed) 200 a-g model. Fermi level is at 0 eV.

4.30. Near the Fermi level, the contributions due to pentagons and heptagons are higher than hexagons, which is consistent with our observation from the localized eigenstates: the localization around Fermi level is associated with odd-membered rings. However, most atoms in odd-membered rings are shared between pentagonal and heptagonal rings. Then at valence edge or conduction edge, on the basis of PDOS calculation, it is hard to distinguish whether the localization around the Fermi level originates from pentagons or heptagons.

The most localized state in planar 200 a-g model is state 3. Its energy level is around 5 eV in the conduction band, and state 3 is highly localized on two atoms shared by two heptagons, as shown in Fig. 4.27(c). In the puckered case, state 3' is found at the exact

same position at state 3, given in Fig. 4.28(c). This is similar to the situation observed in glassy $GeSe_2$ model by Zhang and Drabold[110]. They found that the most defective sites lead to certain localized states far inside the valence and conduction bands.

As illustrated in Fig. 4.26, the global localization degree of puckered 200 a-g model is lower than the planar 200 a-g model. Around the Fermi level, puckered models illustrate localized eigenstates with relatively lower localization degree comparing to planar model. The reduction in strain from puckering helps to delocalize the electronic states. Whereas, in the valence and conduction bands, the localization degree of eigenstates in puckered amorphous graphene model is significantly decreased compared to planar model. Taking state 3 and 3' as example, even though they are localized on the same atoms, state 3' possesses higher energy level and significantly lower localization degree, as shown in Fig. 4.26.

4.5.6 Classical Normal Modes

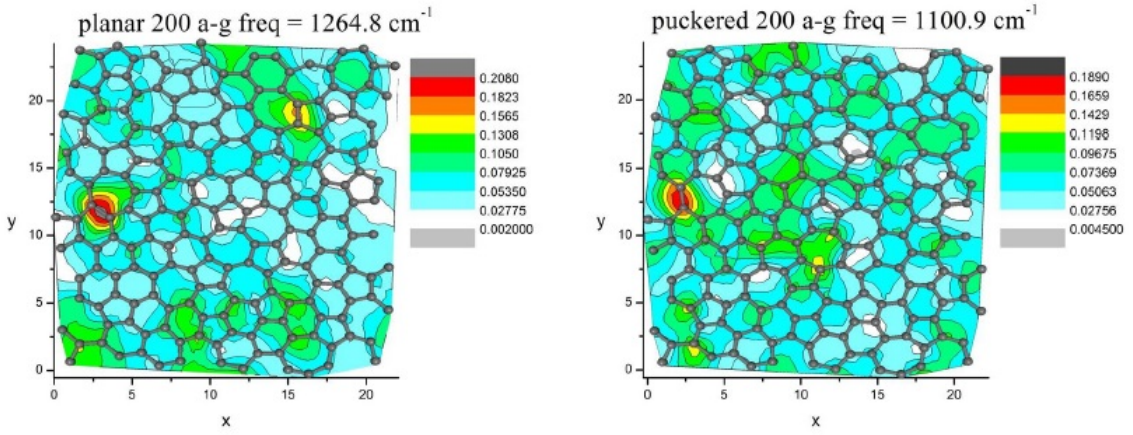

(a) Localized high-frequency phonon mode in planar 200 a-g model.

(b) Localized high-frequency phonon mode in puckered 200 a-g model.

Figure 4.31: Two localized high-frequency phonon modes in planar and puckered 200 a-g modes.

Phonon calculations were performed for both planar and puckered 200 a-g models. Their dynamical matrixes were constructed, by computing forces on all atoms from six orthogonal displacements of 0.04 Bohr. In the high frequency range, we found that several phonon modes are localized at the same range as state 3 and 3' in planar and puckered 200 a-g models respectively, as given in Fig. 4.27(c) and 4.28(c). Two examples of planar and puckered 200 a-g modes are shown in Fig. 4.31. Thus the high localization degree in conduction bands in planar and puckered amorphous graphene models could be originated from the electron-phonon coupling due to these high-frequency modes. Also compared to planar 200 a-g model, the intensity of these phonon modes are lower in puckered a-g model, as illustrated in Fig. 4.31. Therefore, after the strain is released by pentagonal puckering, the coupling effects due to these phonon modes decline, leading probably to reduced electron-phonon coupling.

4.5.7 Conclusion

In conclusion, we found that localized eigenstates in both planar and puckered amorphous graphenes originate from odd-membered rings. Around Fermi level, localized states at valence edge are found in the high-pentagon-ratio area. And the localized states at conduction edge are distributed in the area associated with more heptagons. Far inside the conduction edge, the most localized states in both planar and puckered amorphous graphene models are distributed on the same atoms associated with the junction of heptagons, and are strongly coupled with high-frequency phonon modes. The transport properties of amorphous graphene would be profoundly impacted by these localized states as seen from applying the Kubo-Greenwood formula[119].

Also the IPR calculations reveal that the localization is higher in planar amorphous graphene model compared to the puckered configuration. This could be due to the reduction in strain by pentagonal puckering.

4.6 Conlusion

In this chapeter, we show planar graphene is unstable under external distortion due to pentagonal puckering. The potential energy landscape of amorphous graphene has been explored using Molecular Dynamics approach. Also the electronic properties of planar and puckered amorphous graphene have been discussed.

5 Summary and Future Work

In this dissertation, a few points related to the origin of the Urbach tails in α-Si have been explored. First, the exponential tails clearly exist in large-scale systems (up to 10^5 atoms). These findings are high consistent with smaller models prepared by a similar way. For the strain field induced by short bonds, we shown the most reasonable decay would be a power law. And by phonon calculations, these short bonds behave like phonon traps, causing highly localzied phonon states with frequency higher than $550cm^{-1}$. By performing Molecular Dynamics calculations at constant temperature, we observe the filaments persist at finite temperture, but they are extremely dynamic, even at room temperature. Finally, by exploring the behavior of filaments under different temperatures, it may imply that the external pressure leads to variation of the filaments and then affect the Urbach tails.

For various phases of sp^2 carbon, positive curvature opens up the HOMO-LUMO gap. With the increase of schwarzite sizes, the influence of negative curvature on DOS is reduced. The total energy also declines with the increasing size of closed cage.

For amorphous graphene, we have shown that the presence of pentagons and heptagons induces many states around the Fermi level, and pentagons increase the sensitivity of whole system to external distortions leading to puckered states. A series of MD and quenching simulations suggest these puckered states correspond to distinct local minima on the PEL of amorphous graphene, whose boundaries can be overcomed by heating up the system. Each basin of the PEL is associated with a continuum of bond lengths, bond angles and energy scale. Finally the electronic properties of both crystalline and amorphous graphene have been calculated. The odd-membered rings could lead to strong electron-phonon coupling in these models, and the coupling may be reduced due to the puckered effect.

5.1 Future Work

For the origin of the Urbach tails, there are evidences shown the correlation between filaments and exponential tails. The next interesting thing would be to test the nessasity of filaments to the exponential tials. For fullerenes and schwarzite, the correlation between density of states and curvature of whole system requires further investigation. It would be interesting to show how the electrons are localized in these models, and give rise to their unique electronic properties. For amorphous graphene, since we have observed low-frequency phonon modes akin to floppy modes, it would be a great start to explore the origin of Boson peaks in VDOS of amorphous materials.

REFERENCES

[1] Drabold, D. A. (2009). Topics in the Theory of Amorphous Materials. *The European Physical Journal B, 68*, 1-21.

[2] Cohen, M. L., and Heine, V. (1970). *Solid State Physics* (Vol. 24), New York: Academic Press.

[3] Ashcroft, N. W., Mermin, N. D. (1976). *Solid State Physics*, Cengage Learning.

[4] Ceperley, D. M., and Alder, B. J. (1980). Ground State of the Electron Gas by a Stochastic Method. *Physical Review Letters 45*, 566.

[5] Becke, A. D. (1988). Density-Functional Exchange-Energy Approximation with Correct Asymptotic Behavior. *Physical Review A 38*, 3098.

[6] Perdew, J. P., and Wang, Y. (1992). Accurate and Simple Analytic Representation of the Electron-Gas Correlation Energy. *Physical Revew B 45*, 13244.

[7] Perdew, J. P., Burke, K., and Ernzerhof, M. (1996). Generalized Gradient Approximation Made Simple. *Physical Review Letters 77*, 3865.

[8] Artacho, E., Anglada, E., Dieguez, O., Gale, J. D., Garcia, A., Junquera, J., Martin, R. M., Ordejon, P., Sanchez-Portal, J. M., and Soler, J. M. (2008). The SIESTA Method; Developments and Applicability. *Journal of Physics: Condensed Matter Vol. 20*, 064208.

[9] Kresse, G., and Furthmuller, J. (1996). Efficient Iterative Schemes for *ab initio* Total-Energy Calculations Using a Plane-Wave Basis Set. *Physical Review B 54*, 11169.

[10] Zhang, X. (2001). *Theoretical studies of structural, electronic and optical properties of amorphous chalcogenide materials* (Doctoral dissertation). Available from ProQuest Dissertations & Theses database (UMI No. 3007478).

[11] King, S. V. (1967). Ring Configurations in a Random Network Model of Vitreous Silica. *Nature 213*, 1112-1113.

[12] Guttman, L. (1990). Ring Structure of the Crystalline and Amorphous Forms of Silicon Dioxide. *Journal of Non-Crystalline Solids 116*, 145-147.

[13] Goetzke, K. and Klein, H. J. (1991). Properties and Efficient algorithmic Determination of Different Classes of Rings in Finite and Infinite Polyhedral Networks. *Journal of Non-Crystalline Solids Vol. 127*, 215-220.

[14] Yuan, X., and Cormack, A. N. (2002). Efficient Algorithm for Primitive Ring Statistics in Topological Networks. *Computational Materials Science, Vol. 24*, 343-360.

[15] Wooten, F. (2002). Structure, Odd Lines and Topological Entropy of Disorder of Amorphous Silicon. *Acta Crystallographica Section A 58, Part 4*, 346-351.

[16] Roux, S. Le, and Petkov, V. (2010). *ISAACS* - Interactive Structure Analysis of Amorphous and Crystalline Systems. *Journal of Applied Crystallography 43, Part 1*, 181-185.

[17] Cai, B. (2011). *Model Design and Analysis for Amorphous Materials* (Docteral dissertation). Available from ProQuest Dissertations & Theses database (UMI No. 3478430).

[18] Urbach, F. (1953). The Long-Wavelength Edge of Photographic Sensitivity and of the Electronic Absorption of Solids. *Physical Review 92*, 1324.

[19] Anderson, P. W. (1958). Absence of Diffusion in Certain Random Lattices. *Physical Review 109*, 1492.

[20] Pan, Y., Inam, F., Zhang, M., and Drabold, D. A. (2008). Atomistic Origin of Urbach Tails in Amorphous Silicon. *Physical Review Letters 100*, 206403.

[21] Inam, F., Lewis, J. P., and Drabold, D. A. (2010). Hidden Structure in Amorphous Solids. *Physica Status Solidi A 207*, 599-604.

[22] Barkema, G. T., and Mousseau, N. (2000). High-Quality Continuous Random Networks. *Physical Review B 62*, 4985.

[23] Dong, J., and Drabold, D. A. (1998). Atomistic Structure of Band-Tail States in Amorphous Silicon. *Physical Review Letters 80*, 1928.

[24] Djordjevic, B. R., Thorpe, M. F., and Wooten, F. (1995). Computer Model of Tetrahedral Amorphous Diamond. *Physical Review B 52*, 5685.

[25] Haydock, R. (1980). The Recursive Solution of the Schrodinger Equation. *Solid State Physics Vol. 35*, 215-294.

[26] Ordejon, P., Drabold, D. A., Martin, R. M., and Grumbach, M. P. (1995). Linear System-Size Scaling Methods for Electronic-Structure Calculations. *Physical Review B 51*, 1456.

[27] Kwon, I., Biswas, R., Wang, C. Z., Ho, K. M. and Soukoulis C. M. (1994). Transferable Tight-Binding Models for Silicon. *Physical Review B 49*, 7242.

[28] Jaynes, E. T. (2003). *Probability Theory: The Logic of Science*. Cambridge, UK: Cambridge University Press.

[29] Drabold, D. A., and Sankey, O. F. (1993). Maximum Entropy Approach for Linear Scaling in the Electronic Structure Problem. *Physical Review Letters 70*, 3631.

[30] Mead, L. R., and Papanicolaou, N. (1984). Maximum Entropy in the Problem of Moments. *Journal of Mathematical Physics 25*, 2404.

[31] Bandyopadhyay, K., Bhattacharya, A. K., Biswas, P., and Drabold, D. A. (2005). Maximum Entropy and the Problem of Moments: A Stable Algorithm. *Physical Review E 71*, 057701.

[32] Ludlam, J. J.. Taraskin, S. N., Elliot, S. R., and Drabold, D. A. (2005). Universal Features of Localized Eigenstates in Disordered Systems. *Journal of Physics: Condensed Matter 17*, L321.

[33] Drabold, D. A., Ordejon, P., Dong, J., and Martin, R. M. (1995). Spectral Properties of Large Fullerenes: From Cluster to Crystal. *Solid State Communications Vol 96 Issue 11*, 833.

[34] Martin, R. M. (2004). *Electronic Structure*. Cambridge, UK: Cambridge University Press.

[35] Fedders, P. A., and Carlsson, A. E. (1985). Information-Theoretic Approach to High-Temperature Spin Dynamics. *Physical Review B 32*, 229.

[36] Drabold, D. A., and Fedders, P. A. (1988). Dipolar Broadening in Magnetically Diluted Lattices. *Physical Review B 37*, 3440.

[37] Pan, Y., Zhang, M., and Drabold, D. A. (2008). Topological and Topological-Electronic Correlation in Amorphous Silicon. *Journal of Non-Crystalline Solids Vol 354 Issue 29*, 3480.

[38] Landau, L. D., and Lifshitz, E. M. (1959). *Theory of Elasticity*. London: Pergamon Press.

[39] Aljishi, S., Cohen, J. D., Jin, S., and Ley, L. (1990). Band Tails in Hydrogenated Amorphous Silicon and Silicon-Germanium Alloys. *Physical Review Letters 64*, 2811.

[40] Liang, J., Schiff, E. A., Guha, S., Yan, B., and Yang, J. (2006). Hole-Mobility Limit of Amorphous Silicon Solar Cells. *Applied Physics Letters 88*, 063512.

[41] Cliffe, M. J., Dove, M. T., Drabold, D. A. and Goodwin, A. L. (2010). Structure Determination of Disordered Materials from Diffraction Data. *Physical Review Letters 104*, 125501.

[42] Street, R. (1991). *Hydrogenated Amorphous Silicon*. Cambridge, UK: Cambridge University Press.

[43] Drabold, D. A., Fedders, P. A., Klemm, S., and Sankey, O. F. (1991). Finite-Temperature Properties of Amorphous Silicon. *Physical Review Letters 67*, 2179.

[44] Li, Y., and Drabold, D. A. (unpublished).

[45] The ”filament free” model was obtained by performing extended thermal MD simulations at T = 300 K and waiting for an instantaneous conformation *sans* filaments.

[46] Meyer, R., and Comtesse, D. (2011). Vibrational Density of States of Silicon Nanoparticles. *Physical Review B 83*, 014301.

[47] Ziman, J., M. (1972). *Principles of the Theory of Solids, 2nd edition*. Cambridge, UK: Cambridge University Press.

[48] Drabold, D. A., Li, Y., Cai, B., and Zhang, M. (2011). Urbach Tails of Amorphous Silicon. *Physical Review B 83*, 045201.

[49] Novoselov, K. S., Geim, A. K., Morozov, S. V., Jiang, D., Zhang, Y., Dubonos, S. V., Gregorieva, I. V., and Firsov, A. A. (2004). Electric Field Effect in Atomically Thin Carbon Films. *Science 306*, 666.

[50] Castro Neto, A. H., Guinea, F., Peres, N. M. R., Novoselov, K. S., and Geim, A. K. (2009). The Electronic Properties of Graphene. *Reviews of Modern Physics 81*, 109.

[51] Novoselov, K. S., Jiang, D., Schedin, F., Booth, T. J., Khotkevich, V. V., Morozov, S. V., and Geim, A. K. (2005). Two-Dimensional Atomic Crystals. *Proceedings of the National Academy of Sciences of the United States of America Vol 102 No 30*, 10451-10453.

[52] Zhang, Y., Tan, J. W., Stormer, H. L., and Kim, P. (2005). Experimental Observation of the Quantum Hall Effect and Berry's Phase in Graphene. *Nature 438*, 201-204.

[53] Novoselov, K. S., Geim, A. K., Morozov, S. V., Jiang, D., Katsnelson, M. I., Grigorieva, L. V., Dubonos, S. V., and Firsov, A. A. (2005). Two-dimensional Gas of Massless Dirac Fermions in Graphene. *Nature 438*, 197-200.

[54] Harris, J. (1985). Simplified Method for Calculating the Energy of Weakly Interacting Fragments. *Physical Review B 31*, 1770-1779.

[55] Christ, K. V., and Sadeghpour, H. R. (2007). Energy Dispersion in Graphene and Carbon Nanotubes and Molecular Encapsulation in Nanotubes. *Physical Review B 75*, 195418.

[56] Gui, G., Li, J., and Zhong, J. (2008). Band Structure Engineering of Graphene by Strain: First-principles Calculations. *Physical Review B 78*, 075435.

[57] Li, Y., Inam, F., Kumar, A., Thorpe, M., and Drabold, D. A. (2011). Pentagonal Puckering in a Sheet of Amorphous Graphene. *Physica Status Solidi B Vol 248 Issue 9*, 2082.

[58] Machon, M., Reich, S., Thomsen, C., Sanchez-Portal, D., and Ordejon, P. (2002). ab-initio Calculations of the Optical Properties of 4--diameter Single-walled Nanotubes. *Physical Review B 66*, 155410.

[59] Kroto, H. W., Heath, J. R., Obrien, S. C., Curl, R. F., and Smalley, R. E. (1985). C60: Buckminsterfullerene. *Nature 318*, 162-163.

[60] Kratschmer, W., Lamb, L. D., Fostiropoulos, K., and Huffman, D. R. (1990). Solid C60: a New Form of Carbon. *Nature 347*, 354.

[61] Yu, M., Chaudhuri, I., Leahy, C., Wu, S. Y., and Jayanthi, C. S. (2009). Energetics, Relative Stabilities, and Size-dependent Properties of Nanosized Carbon Clusters of Different Families: Fullerenes, Bucky-diamond, Icosahedral, and Bulk-truncated Structures. *The Journal of Chemical Physics 130*, 184708.

[62] Diniz, G. S. (2012). *Electronic and Transport Properties of Carbon Nanotubes: Spin-orbit Effects and External Fields* (Docteral dissertation). Available from ProQuest Dissertations & Theses database (UMI No. 3540124).

[63] Saito, R., Dresselhaus, G., and Drssehaus, M. S. (1998). *Physical Properties Of Carbon Nanotubes*. London: Imperical College Press.

[64] Diniz, G. S. (2012). *Electronic and Transport Properties of Carbon Nanotubes: Spin-orbit Effects and External*. ProQuest Dissertations & Theses database (UMI No. 3540124).

[65] Phillips, R., Drabold, D. A., Lenosky, T., Adams, G. B., and Sankey, O. F. (1992). Electronic Structure of Schwarzite. *Physical Review B 46*, 1941.

[66] Monkhorst, H. J., and Pack, J. D. (1976). Special Points for Brillouin-zone Integrations. *Physical Review B 13*, 5188.

[67] Terrones, H., and Terrones, M. (2003). Curved Nanostructured Materials. *Journal of Physics 5*, pp. 126.1-126.37.

[68] Kotakoski, J., Meyer, J. C., Kurasch, S., Santos-Cottin, D., Kauser, U., and Krasheninnikov, A. V. (2011). Stone-Wales-type transformations in carbon nanostructures driven by electron irradiation. *Physical Review B 83*, 245420.

[69] Kotakoski, J., Krasheninnikov, A. V., Kaiser, U., and Meyer, J. C. (2011). From Point Defects in Graphene to Two-Dimensional Amorphous Carbon. *Physical Review Letters 106*, 105505.

[70] Meyer, J. C., Kisielowski, C., Erni, R., Rossell, M. D., Crommie, M. F., and Zettl, A. (2008). Direct Imaging of Lattice Atoms and Topological Defects in Graphene Membranes. *Nano Letters 8(11)*, 3582.

[71] Meyer, J. C., Girit, C. O., Crommie, M. F., and Zettl, A. (2008). Hydrocarbon lithography on graphene membranes. *Applied Physics Letters 92*, 123110.

[72] Kawasumi, K., Zhang, Q., Segawa, Y., Scott, L. T., and Itami, K. (2013). A Grossly Warped Nanographene and the Consequences of Multiple Odd-membered-ring Defects. *Nature Chemistry 5*, 739-744.

[73] Stone, A. J., and Wales, D. J. (1986). Theoretical studies of icosahedral C60 and some related species. *Chemical Physics Letters 128*, 501-503.

[74] Wooten, F., Winer, K., and Weaire, D. (1985). Computer Generation of Structural Models of Amorphous Si and Ge. *Physical Review Letters 54*, 1392.

[75] Zachariasen, W. H. (1932). The Atomic Arrangement in Glass. *Journal of the American Chemical Society 54*, 3841-3851.

[76] Kapko, V., Drabold, D. A., and Thorpe, M. F. (2010). Electronic Structure of a Realistic Model of Amorphous Graphene. *Physica Status Solidi B 247*, 1197-1200.

[77] Stillinger, F. H. (1995). A Topographic View of Supercooled Liquids and Glass Formation. *Science 267*, 1935.

[78] Wallace, D. C., Statistical Mechanics of Monatomic Liquids. *Physical Review E 56*, 4179.

[79] Stillinger, F. H. (1998). Enumeration of Isobaric Inherent Structures for the Fragile Glass Former o-Terphenyl. *the Journal of Physical Chemistry B 102*, 2807.

[80] Stillinger, F. H., and Weber, T. A. (1983). Dynamics of Structural Transitions in Liquids. *Physical Review A 28*, 2408.

[81] Stillinger, F. H. (1999). Exponential Multiplicity of Inherent Structures. *Physical Review E 59*, 48.

[82] Shilling, R. (2006). Energy Landscape Properties Studied Using Symbolic Sequences. *Physica D: Nonlinear Phenomena 216*, 157.

[83] Doye, J. P. K., and Wales, D. J. (2002). Saddle Points and Dynamics of Lennard-Jones Clusters, Solids and Supercooled Liquids. *the Journal of Chemical Physics 116*, 3777.

[84] Fedders, P. A., and Drabold, D. A. (1996). Molecular-Dynamics Investigations of Conformational Fluctuations and Low-Energy Vibrational Excitations in α-Si:H. *Physical Review B 53*, 3841.

[85] Robertson, J., and O'Reilly, E. P. (1987). Electronic and Atomic Structure of Amorphous Carbon. *Physical Review B 35*, 2946.

[86] Jornanda, F. H., Gava, V., Martinotto, A. L., Cassol, L. A., and Perottoni, C. A. (2010). Modeling of amorphous carbon structures with arbitrary structural constraints. *Journal of Physics: Condensed Matter 22*, 395402.

[87] Frauenheim, Th., Blaudeck, P., Stephan, U., and Jungnickel, G. (1993). Atomic Structure and Physical Properties of Amorphous Carbon and Its Hydrogenated Analogs. *Physical Review B 48*, 4823.

[88] Lusk, M. T., and Carr, L. D. (2008). Nanoengineering Defect Structures on Graphene. *Physical Review Letters 100*, 175503.

[89] Holmstrom, E., Fransson, J., Eriksson, O., Lizarraga, R., Sanyal, B., Bhandary, S., and Katsnelson, M. (2011). Disorder-Induced Metallicity in Amorphous Graphene. *Physical Review B 84*, 205414.

[90] Anderson, P. W., Halperin, B. I., and Varma, C. M. (1972). Anomalous low-temperature thermal properties of glasses and spin glasses. *Philosophical Magazine 25*, 1.

[91] Phillips, W. A. (1981). *Amorphous Solids: Low Temperature Properties*. Germany, Berline: Springer.

[92] Drabold, D. A., Wang, R., Klemm, S., Sankey, O. F., and Dow, J. D. (1991). Efficient *ab initio* Molecular-Dynamics Simulations of Carbon. *Physical Review B 43*, 5132.

[93] Drabold, D. A., Fedders, P. A., and Grumbach, M. P. (1996). Gap Formation and Defect States in Tetrahedral Amorphous Carbon. *Physical Review B 54*, 5480.

[94] Wales, D. J. (2003). *Energy Landscapes with Applications to clusters, Biomolecules and Glasses*. New York: Cambridge University Press.

[95] Lee, J., Scheraga, H. A., and Rackovsky, S. (1998). New Optimization Method for Conformational Energy Calculations on Polypeptides: Conformational Space Annealing. *Journal of Computational Chemistry 18*, 1222.

[96] Lee, J., Scheraga, H. A., and Rackovsky, S. (1998). Conformational Analysis of the 20-Residue Membrane-Bound Portion of Melittin by Conformational Space Annealing. *Biopolymers 46*, 103.

[97] Lee, J., and Scheraga, H. A. (1999). Conformational Space Annealing by Parallel Computations: Extensive Conformational Search of Met-Enkephalin and of the 20-Residue Membrane-Bound Portion of Melittin. *International Journal of Quantum Chemistry 75*, 255.

[98] Liwo, A., Lee, J., Ropoll, D. R., Pillardy, J., and Scheraga, H. A. (1999). Protein Structure Prediction by Global Optimization of a Potential Energy Function. *Proceedings of the National Academy of Science of the United States of America 96*, 5482.

[99] Cataldo, F., Ori, O., and Iglesias-Groth, S. (2010). Topological Lattice Descriptors of Graphene Sheets with Fullerene-like Nanostructures. *Molecular Simulation 36*, 341.

[100] Liu, F., Ming, P., and Li, J. (2007). *Ab initio* Calculation of Ideal Strength and Phonon Instability of Graphene Under Tension. *Physical Review B 76*, 064120.

[101] Tamor, M. A., and Vessel, W. C. (1994). Raman "Fingerprinting of Amorphous Carbon Films. *Journal of Applied Physics 76*, 3823.

[102] Ferrari, A. C., and Robertson, J. (2000). Interpretation of Raman Spectra of Disordered and Amorphous Carbon. *Physical Review B 61*, 14095.

[103] Drabold, D. A., Fedders, P. A., and Stumm, P. (1994). Theory of Diamondlike Amorphous Carbon. *Physical Review B 49*, 16415.

[104] Phillips, J. C. (1981). Topology of Covalent Non-crystalline Solids II: Medium-Range Order in Chalcogenide Alloys and A-Si(Ge). *Journal of Non-Crystalline Solids 43*, 37.

[105] Thorpe, M. F. (1983). Continuous Deformations in Random Networks. *Journal of Non-Crystalline Solids 57*, 355.

[106] Goldstein, M. (1969). Viscous Liquids and the Glass Transition: A Potential Energy Barrier Picture. *The Journal of Chemical Physics 51*, 3728.

[107] Biswas, R., Bouchard, A. M., Kamitakahara, W. A., Grest, G. S., and Soukoulis, C. M. (1988). Vibrational Localization in Amorphous Silicon. *Physical Review Letters 60*, 2280.

[108] Fedders, P. A., Drabold, D. A., and Klemm, S. (1992). Defects, Tight Binding, and First-Principles Molecular-Dynamics Simulations on α-Si. *Physical Review B 45*, 4048.

[109] Nakhmanson, S. M., and Drabold, D. A. (2000). Low-Temperature Anomalous Specific Heat without Tunneling Modes: A Simulation for α-Si with Voids. *Physical Review B 61*, 5376.

[110] Zhang, X., and Drabold, D. A. (2000). Structural and Electronic Properties of Glassy $GeSe_2$ Surfaces. *Physical Review B 62*, 15695.

[111] Atta-Fynn, R., Biswas, P., and Drabold, D. A. (2004). Electron-Phonon Coupling is Large for Localized States. *Physical Review B 69*, 245204.

[112] Abrahams, E., Anderson, P. W., Licciardello, D. C., and Ramakrishnan, T. V. (1979). Scaling Theory of Localization: Absence of Quantum Diffusion in Two Dimensions. *Physical Review Letters 42*, 673.

[113] Peres, N. M. R., Guinea, F., and Castro Neto, A. H. (2006). Electronic Properties of Disordered Two-Dimensional Carbon. *Physical Review B 73*, 125411.

[114] Painter, O., Lee, R. K., Scherer, A., Yariv, A., O'Brien, J. D., Dapkus, P., D., and Kim, I. (1999). Two-dimensional Photonic Band-Gap Defect Mode Laser. *Science 284*, 1819.

[115] Jackson, S. A., and Platzman, P. M. (1981). Polaronic Aspects of Two-Dimensional Electrons on Films of Liquid He. *Physical Review B 24*, 499.

[116] Xu, P., Yang, Y., Barber, S. D., Ackerman, M. L., Schoelz, J. K., Kornev, I. A., Barraza-Lopez, S., Bellaiche, L., and Thibado, P. M. (2011). Giant Surface Charge Density of Graphene Resolved from Scanning Tunneling Microscopy and First-principles Theory. *Physical Review B 84*, 161409(R).

[117] Warner, J. H., Lee, Gun-Do, He, K., Robertson, A. W., Yoon, E., and Kirkland, A. I. (2013). Bond Length and Charge Density Variations within Extended Arm Chair Defects in Graphene. *ACS Nano, 7 (11)*, pp 9860-9866.

[118] Li, Y., and Drabold, D. A. (2013). Symmetry breaking and low energy conformational fluctuations in amorphous graphene. *Physica Status Solidi B*, DOI: 10.1002/pssb.201341620.

[119] Abtew, T. A., Zhang, M., and Drabold, D. A. (2007). Ab initio Estimate of the Temperature Dependence of Electrical Conductivity in a Model Disordered Material: a-Si:H. *Physical Review B 76*, 045212.

Thesis and Dissertation Services